Hydroelastic wave deformation of Very Flexible Floating Structures

A performance study of a monolithic finite element model

Sjoerd van Hoof

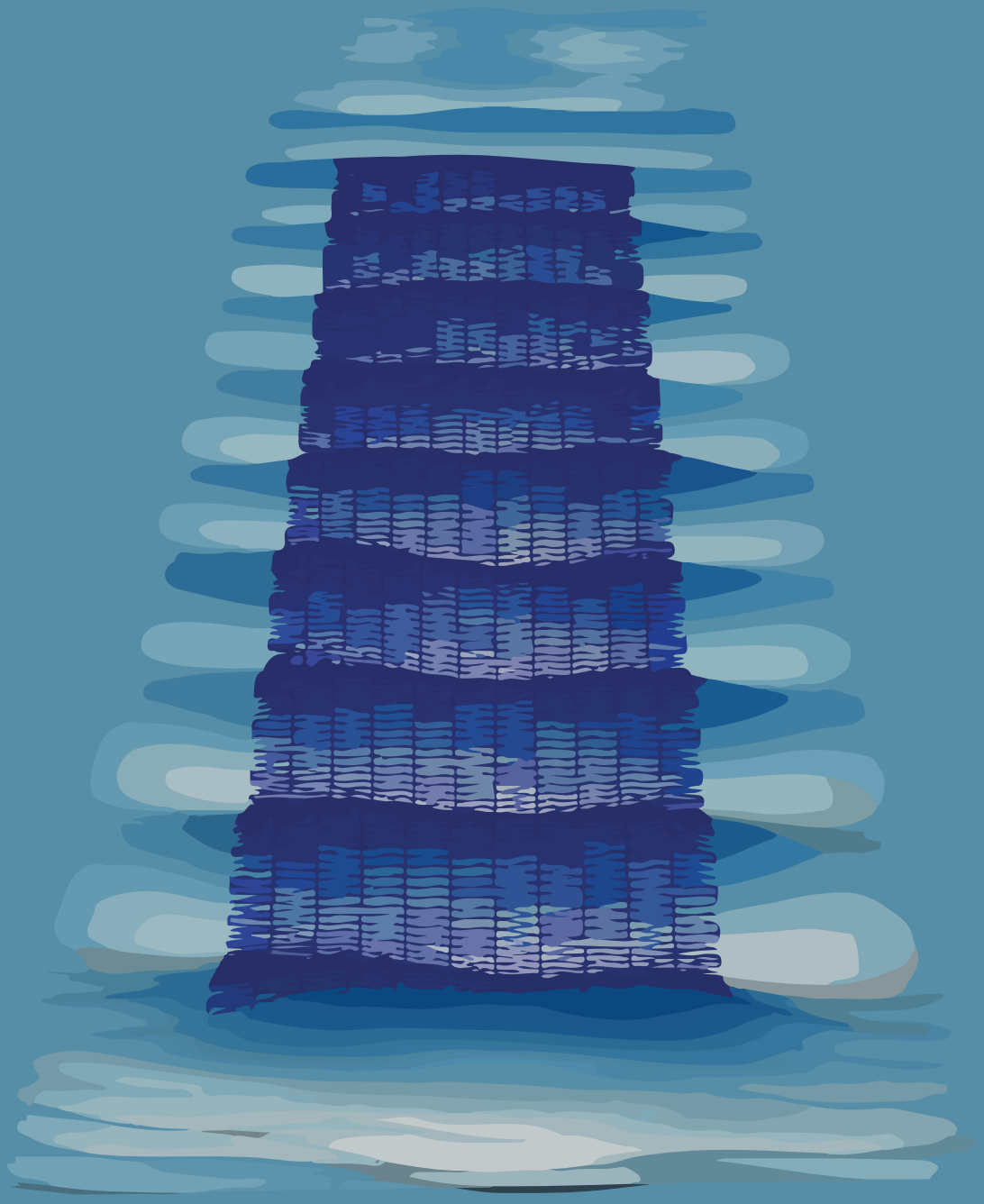

Technische Universiteit Delft - Section Coastal Engineering

mocean
ADVANCED OFFSHORE TECHNOLOGY

TU Delft

Hydroelastic wave deformation of Very Flexible Floating Structures

A performance study of a monolithic finite element model

by

Sjoerd van Hoof

Student number:	4273125	
Project duration:	October 1, 2020 – July 23, 2021	
Thesis committee:	Dr. ir. A. Antonini,	TU Delft, chair
	Dr. ir. S. Schreier,	TU Delft, committee member
	Dr. ir. O. Colomes-Gene,	TU Delft, committee member
	Ir. C.A. Morshuis,	Mocean Offshore, supervisor
	Ir. M. Hoogeveen,	Mocean Offshore, supervisor

An electronic version of this thesis is available at `http://repository.tudelft.nl/`.

TU Delft

Abstract

At the moment, the world is at the verge of an energy transition. One of the most promising green resources is solar energy, which is a rapidly growing market. However, to fully use its potential of economy of scale, the application of offshore floating solar should be explored. A promising option is the use of a flexible type of Very Large Floating Structures (VLFSs), which are called Very Flexible Floating Structures (VFFSs). They are characterised by their large length to height ratio compared to rigid bodies and depending on their material properties have a hydroelastic response to the incident wave.

In the late 1990s, a lot of research has been done on VLFSs by Tsubogo and Okada (1998) who derived an analytical dispersion relation assuming a zero-draught structure. However, only recently, Schreier and Jacobi (2020b) did experimental research on VFFSs in a towing tank at the Delft University of Technology, as little is still known about flexible structures. This report focuses on a numerical alternative that covers both VLFSs as well as VFFSs using a Finite Element Method (FEM) Fluid Structure Interaction (FSI) model which has been built based on potential flow to model the fluid and a dynamic Euler-Bernoulli beam that represents the floating structure using the Julia package Gridap. One of the main advantages is that the zero-draught assumption is not necessary and, therefore, structures with larger draughts can also be modelled. Next to this, the numerical model is able to cope with irregular shapes, for which no analytical method yet exists.

The model is built such that it can handle 2D as well as 3D domains. A 2D analysis has been made to understand the influence of hydroelastic wave deformation of the incident wave, in terms of wavelength dispersion as well as amplitude dispersion on floating structures. To verify the model, the numerical results were compared to the analytical solution and experimental research in a towing tank, which showed accurate results. Test runs were set up that mimicked the towing tank set-up and a full-scale solar park.

Furthermore, a sensitivity study was executed that shows the limits of the flexible domain and to see in which cases significant (>1%) hydroelastic wave deformation would occur using governing mean and extreme ocean waves, as well as a typical lake wave. Finally, the influence of the draught of the structure was examined.

This report provides a good overview of when wave deformation should be accounted for in terms of bending rigidity and density. Confirming existing theory, it was found that the stiffness of the VFFS causes wave stretching and the draught of the structure influences the extent of wave shortening. It was also found that significant wave deformation will not occur for ocean waves as the required stiffness is beyond existing materials. For extreme ocean waves, there is even no dispersion at all. As the wave frequency increases, the hydroelastic interaction gets stronger. The typical lake wave showed to be well within the flexible regime and also showed significant dispersion with realistic material parameters. The numerical model is able to cope with large draught scenarios which lead to wave shortening, which in its turn leads to wave focusing.

Ultimately, the numerical model showed to be a good alternative to existing methods to investigate the behaviour of VLFSs outside the floating solar domain, where one could think of ice floes, floating islands or floating airports.

Preface

“Voor niets gaat de zon op”

is a Dutch saying, which means that nothing comes free of cost. Hard work and investing plenty of time will give you the desired result. For the last nine months, I have been working on my master thesis which is the final part of me as a student of the Delft University of Technology. What started as a request of Mocean Offshore to find a knowledge gap within the floating solar market, at the beginning of October 2020, evolved into a fluid structure interaction model to describe the hydroelastic response of the structure.

This wasn’t a straightforward route, however. The first few weeks of the project, I started to conduct interviews with all actors within the industry, trying to understand the status quo and which difficulties they were facing. Most of them were busy building rigid puzzle-like structures on inland waters and were mostly concerned about optimising electric circuits, whereas the hydrodynamics were less of an issue. However, for offshore purposes the technology was still immature. I found out that Sebastian Schreier was conducting experimental research at the TU Delft about very flexible floating structures in the towing tank at 3ME. This sounded like the perfect solution to large oceanic wave action. Rather than building a physical myself as well, I wanted to build a numerical model that could cope with the same environment, but also be changed easily in terms of material properties and incident waves. In a search to find someone who could help me build a numerical model, I found Oriol Colomés Gené who is involved in the built of a Julia module called Gridap and specialised in fluid structure interactions. Combining the knowledge of both researchers gave me the opportunity to build the model I was aiming for.

However, the real objective only started when I had surrounded myself with these amazing people. A big thanks to Sander and Maas, my company supervisors, who helped me get acquainted with the potential flow theory and guided me through every phase of the master thesis. I would also like to thank Alessandro, the chair of my committee, who kept the deadlines tight and helped me focus on the right things in a labyrinth of complicated mathematics and physics. Furthermore, Sebastian occasionally pulled me out of the numerical domain and put me back in reality, which helped me to zoom out and find the relevance of the study back again, which I am really grateful for. Finally, I would like to thank Oriol, who immediately jumped on the bandwagon and taught me the very principles of the Finite Element Method. During the course of the project, whenever I had questions or struggled with the syntax of his Gridap module, he was there to explain it to me. Sometimes even far beyond office hours.

I would like to conclude by expressing a feeling I had during the entire project. From beginning until the very end, I felt very welcome at the company Mocean Offshore, who gave me the opportunity to work on this project in the office, even though the government limited the available spots due to the COVID-19 pandemic. My colleagues and especially the committee members (university and company) were so well involved in the project that it never felt as if I was working on it alone. This really helped me enjoy the project in its entirety.

Enjoy reading!

Sjoerd van Hoof
Rotterdam, July 2021

Contents

Nomenclature

α_b	Structure stability parameter
α_f	Fluid stability parameter
α_h	General stability parameter
β	Newmark stability parameter
Δt	Timestep
Δx	Spatial resolution
η	Surface elevation
Γ	Boundary of numerical domain
γ	Newmark stability parameter
Γ_b	Beam boundary
γ_h	Order stability parameter
Γ_L	Left boundary
Γ_R	Right boundary
Γ_{btm}	Bottom boundary
Γ_{dz}	Boundary damping zone
Γ_{fs}	Free surface boundary
λ	Wavelength
λ_1	Wavelength short wave
λ_2	Wavelength long wave
Λ_b	Edge of internal nodes of structure
λ_b	Wavelength hydroelastic wave
λ_c	Characteristic length
λ_i	Wavelength incident wave
λ_o	Wavelength outgoing wave
μ	Mass per unit length
μ_0	Damping factor
μ_1	Damping coefficient
μ_2	Dispersion coefficient
ν	Poisson's ratio
Ω	Numerical domain

ω	Angular frequency
ω_0	Natural heave frequency
ϕ	Potential
ρ_b	Structure density
ρ_w	Water density
C	Damping matrix
M	Mass matrix
$\vec{u}$	Velocity field
$\vec{x}$	Spatial vector
ξ	Wave amplitude
ξ_1	Amplitude short wave
ξ_2	Amplitude long wave
ξ_b	Amplitude hydroelastic wave
ξ_i	Amplitude incident wave
ξ_o	Amplitude outgoing wave
B	Width of structure
C	Courant number
c	Phase velocity
D	Flexural rigidity
d	Water depth
E	Young's modulus
E_t	Total energy
$E_{k,b}$	Kinetic energy structure
$E_{k,f}$	Kinetic energy fluid
$E_{kin,b1}$	Kinetic energy hydroelastic wave
$E_{kin,b2}$	Kinetic energy structure
$E_{kin,i}$	Kinetic energy incident wave
$E_{p,b}$	Potential energy structure
$E_{p,f}$	Potential energy fluid
$E_{pot,b1}$	Potential energy hydroelastic wave
$E_{pot,b2}$	Potential energy structure
$E_{pot,i}$	Potential energy incident wave
EI	Bending rigidity
f^{ext}	External forces

f^{int}	Internal forces
F_1	Transfer function
F_2	Transfer function
g	Gravity constant
H	Wave height
h	Thickness structure
H_d	Design wave
$H_{d,e1}$	Extreme design wave 1
$H_{d,e2}$	Extreme design wave 2
$H_{d,m1}$	Mean design wave 1
$H_{d,m2}$	Mean design wave 2
$H_{d,s}$	Lake design wave
I	Moment of inertia
I_{2D}	Moment of inertia per unit width
K	Wavelength dispersion factor
k	Wave number
K_a	Analytical wavelength dispersion factor
k_b	Wave number hydroelastic wave
k_i	Wave number incident wave
K_n	Expected numerical wavelength dispersion factor
k_o	Wave number outgoing wave
k_p	Characteristic wave number
K_{ri}	Measured incident wavelength dispersion factor
K_{ro}	Measured outgoing wavelength dispersion factor
L_d	Length damping zone
m	Mas per unit area
n	Dispersion parameter
$n_{cells,x}$	Grid resolution (x)
$n_{cells,z}$	Grid resolution (z)
n_{cells}	Number of cells
p	Pressure
P_b	Energy flux hydroelastic wave
P_i	Energy flux incident wave
P_o	Energy flux outgoing wave

R	Amplitude dispersion factor
r	Order of system
R_a	Analytical amplitude dispersion factor
R_{ni}	Expected numerical incident amplitude dispersion factor
R_{no}	Expected numerical outgoing amplitude dispersion factor
R_{ri}	Measured incident amplitude dispersion factor
R_{ro}	Measured outgoing amplitude dispersion factor
T	Wave period
t	Time
T_1	Wave period short wave
T_2	Wave period long wave
T_{max}	Maximum wave period
T_{min}	Minimum wave period
T_{ss}	Steady-state
u_i	Velocity X-direction
w	Vertical displacement
w_i	Velocity Z-direction
x	X coordinate
x_d	X-coordinate start damping zone
y_n	Finite Element node
z	Z coordinate
z_i	ith cell node of Z-coordinate

List of Figures

List of Tables

1

Introduction & problem description

At the moment, the world is at the start of an energy transition. People from all over the world are looking into new ways to generate energy that is not exhaustive. One of these renewable energies is solar power which has the potential to change the world. Would it not be beautiful to use the one thing on Earth that has been given free of cost to use to our advantage, indefinitely? Definitely.

1.1. Solar energy

Solar energy is ”energy obtained from the light and heat from the sun, used to produce electricity”.[1] The technology to catch this type of energy can be divided into two different sections. Either active solar or passive solar depending on how the energy is captured. Active solar techniques include ’concentrating solar power’ and ’photovoltaic systems’ to harness the energy. Passive solar systems include the use of transparent surfaces that enter light into a building or designs that naturally circulate air through spaces. The former will be meant when speaking of solar power in this research. Generally speaking, there are two types of locations to build solar panels; they are built on the land, or floating on a water body.

1.2. Land based solar power

The largest amount of solar energy is generated from land based installations. According to the IEA[2], the total installed capacity of photovoltaics (PV) worldwide is set to 750 GW as of 2020 and will be doubled within the next five years. Figure 1.2 is a graph from the IEA that shows the net additions of installed solar PV globally, starting at 2015. As one can see, China is the main contributor worldwide. As Figure 1.1 shows, the total installed capacity of PV in 2015 was only 200 GW. Therefore, the net additions from Figure 1.2 give a good estimate of the leading countries concerning installed capacity.

[1] Oxford Dictionaries (2020), Solar Power, Oxford Dictionaries, Oxford https://www.oxfordlearnersdictionaries.com/definition/english/solar-power?q=solar+power

[2] IEA (2020), Renewables 2020, IEA, Paris https://www.iea.org/reports/renewables-2020

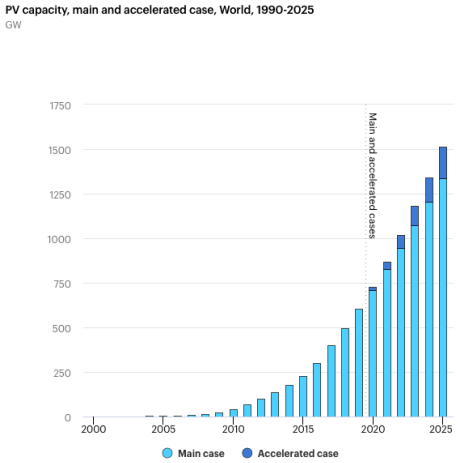

Figure 1.1: Global installed capacity photovoltaics. (IEA, 2020)

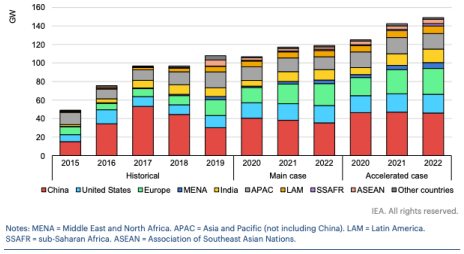

Figure 1.2: Global net additions photovoltaics. (IEA, 2020)

1.3. Floating solar power

As the total installed solar PV is 750 GW in 2020, this consists almost only of land based installations. Figure 1.3 shows the total installed floating solar PV until 2018 and an expectation of 2019. The cumulative installed capacity of FPV is considered to reach 2400 MWp by the end of 2019. According to American credit rating agency Fitch Solutions the floating solar market will grow with 10 GW in the next five years, with China as its main contributor.[3]

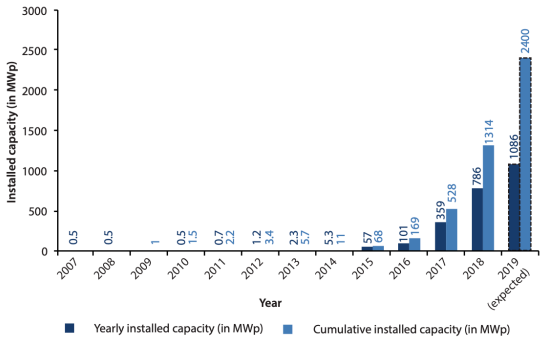

Figure 1.3: Global installed capacity floating photovoltaics. (Acharya and Devraj, 2019)

This clearly states that floating solar PV is still a very small market and is only a fraction of the renewable energy sources. However, as the figures show, the installed capacity is vastly growing at an exponential rate. Floating solar PV can be divided into two distinct segments; inland waterbodies and offshore locations.

1.3.1. Inland

The largest portion of installed capacity is floating on inland waterbodies. The main reason to choose this type is the moderately calm climate. Wind induced waves are the main force acting on the solar panels. As wind waves are a function of the length of the waterbody (fetch), small lakes or old quarries are an ideal location to build FPV. Other types of inland waterbodies which are (potentially) used to accommodate FPV are reservoirs. They are a preferred location as it is man-made, which means the ecological legislation is of less influence, reservoirs already have the proper connections to the grid due to the hydro-power installations and it is often privately owned.[4]

[3] (2020), Fitch Solutions, https://www.rechargenews.com/transition/floating-solar-going-global-with-10gw-more-by-2025-fitch/2-1-894336

[4] (2020), U.S. Army Corps of Engineers, https://www.bloomberg.com/news/articles/2020-05-21/michigan-flood-puts-privately-owned-dams-in-a-critical-spotlight

ProFloating and Groenleven are contractors in floating PV. They exclusively build on inland waterbodies at the moment. The main challenge lies in the interconnections between the modules. According to Van Daalen (2020), working at ProFloating, the modules break due to fatigue. Other concerns were connected to the mooring of the structure as well as the layout of the power circuits. The former is difficult especially when the water depth changes quickly over time or when the waterbody is deep; two typical properties of a reservoir.
Moreover, there is a lot of research going on to optimise the yield of energy. De Jong and Soppe (2020) at TNO are experimenting with the positioning of the solar panels; East-West versus South orientation. Also, experiments are being done to have the floating solar park rotate with respect to the sun. These tests are in collaboration with Marin lead by Otto (2020) who performs the physical experiments in their test labs.

Finally, the maintenance of the panels is a point of attention. Biesheuvel (2020) from Groenleven explained that the challenges they are facing include bird droppings or defective panels which require the operator to have someone fix it.

1.3.2. Offshore

The second and newest type of FPV is based offshore. Although this type is still very immature, it has great potential. The main reason to choose an offshore location is the economy of scale. There is plenty of space in the oceans. Also, less actors are involved during the decision-making process and it is away from everyone's backyard.

As the construction of floating PV is already common practice on inland water bodies, this cannot be said for offshore installations. Where the wind and waves are relatively limited on lakes compared to open sea, this forms the main obstacle for offshore PV. The interconnections of the used modules are not able to withstand the sea loads without an alteration in the design. Next to this, the maintenance is much more difficult compared to inland water body installations, as the location is more remote and the weather conditions are rougher. An offshore design should be less maintenance intensive compared to inland grids.

Also, an offshore solar PV installation needs to be connected to the power grid to bring the electric energy to the mainland. This can be expensive if the offshore location is remote. However, if a location is chosen that already houses wind turbines, an infrastructure is present which lowers the costs. Another option would be to store the electric energy locally. One of the storage options is hydrogen (H_2), which can be used a fuel or as an energy carrier.

Ultimately, as De Werd and Van der Nat (2020) from Bluewater Energy Solutions explained, the installation costs play an important factor for the feasibility of the technology. It is likely that these costs are higher than the alternatives on inland water bodies due to its remoteness. As long as these costs are not reduced, the technology relies on subsidies from the government.

One of the companies that are already operating offshore is Oceans of Energy. They are testing with a rigid structure, that is not much larger than a vessel. Next to this, several joint-ventures are exploring the opportunities of offshore FPV. TNO is working together with Equinor at a test location Lake Oostvoorne near Rotterdam.[5] Shell and Eneco are cooperating under the name CrossWind. This is a new offshore wind park, but also consists of a solar park of 0.5 MW.[6] At the Delft University of Technology, Schreier and Jacobi (2020a) are doing experimental research with flexible floating structures meant as the foundation of FPV.

[5](2020), Solar Magazine, https://solarmagazine.nl/nieuws-zonne-energie/i20999/tno-sabic-equinor-en-westvoorne-testen-drijvende-zonnepanelen-op-het-oostvoornse-meer

[6](2020), Solar Magazine, https://solarmagazine.nl/nieuws-zonne-energie/i22029/nieuwste-nederlandse-windpark-op-zee-krijgt-0-5-megawattpiek-drijvende-zonnepanelen

1.4. Floating structures

To really take advantage of the potential of offshore floating photovoltaics, its main perk (economy of scale) should be further developed. The structure should be at least in the order of magnitude of a football pitch. Such large offshore structures are called Very Large Floating Structures (VLFSs), which also include ice floes, floating islands (as developed in the project Space@Sea (Jiang et al., 2020)) or floating airports. They are characterised by their large length compared to the incident wavelength.

Although VLFSs are not specifically defined, they are characterised by their large length compared to the dominant wavelength of the waves. (Suzuki et al., 2007) Figure 1.4 shows how Suzuki et al. (2007) differentiated Very Large Floating Structures from other floating objects, by dividing the length of the structure (L) over incident wavelength (λ_i) on the x-axis and over the characteristic length (λ_c) on the y-axis. The characteristic length is a measure to quantify the structural stiffness, but a more extensive understanding of this is given in the next chapter.

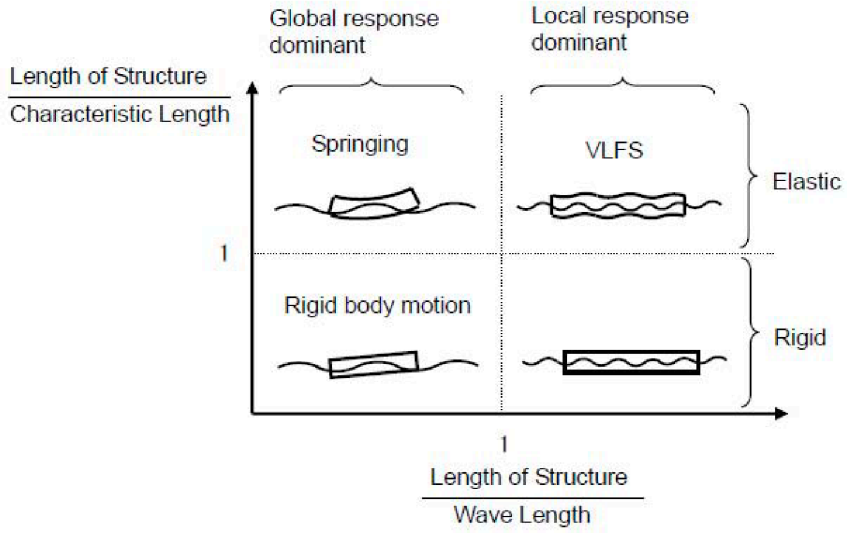

Figure 1.4: Mapping of global response of floating structures. (Suzuki et al., 2007)

Several experiments have been carried out for a range of floating structures. However, most were in the order of $\frac{L}{\lambda_c} \approx 1$; being relatively stiff. (Schreier and Jacobi, 2020b) For structures longer than the incident wavelength, the ratio of wavelength over characteristic length did not exceed $\frac{\lambda_i}{\lambda_c} = 3$. (Schreier and Jacobi, 2020b).

A special type of floating structures is when the characteristic length is much smaller than the dominant wavelength of the sea. In this case it is called a Very Flexible Floating Structure (VFFS). These structures are much more flexible than VLFS, and implies that there is a stronger hydroelastic interaction between the waves and the structure. (Schreier and Jacobi, 2020b) The advantage of this behaviour is that the wave energy is transformed into potential and kinetic energy of the structure instead of slamming against the rigid structure of a VLFS.

When floating structures interact with waves, there is a relation between the incident waves and the deflection of the floating structure. Tsubogo (1999) formulated a dispersion relation between the incident waves and the so called hydroelastic waves, which are defined as ”the propagation of deflection vibrations” and is fully derived in the next chapter.

1.5. Wave diffraction

A possible 3D effect of wave deformation is wave diffraction. Due to a change in wavelength, the celerity of the wave changes accordingly. Wave stretching causes an increase in phase speed, whereas wave

shortening causes a decrease in phase speed. As the sides of the structure should be continuous with the free surface, this effect gradually increases towards the centre-line of the VFFS. Figure 1.5 shows a schematic of the velocity field in the hydroelastic zone. An increased phase speed, results in divergence of wave energy; diffraction. However, a lower wave celerity results in wave focusing. Especially the latter could give unexpected or unwanted loads on the floating structure.

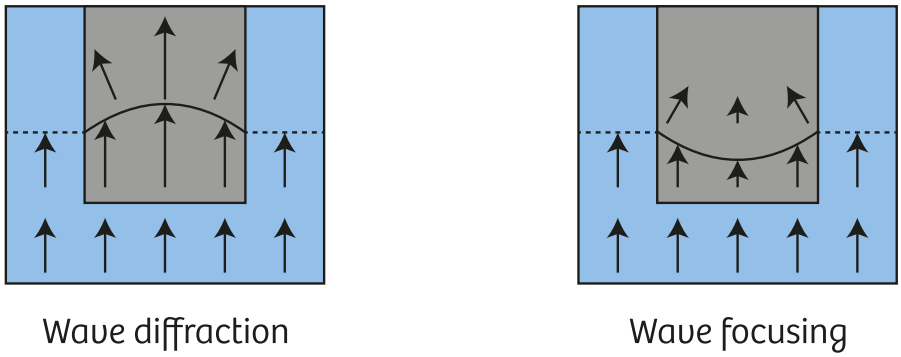

Figure 1.5: Velocity field schematic of wave diffraction (left) or wave focusing (right).

1.6. Mocean Offshore

Mocean Offshore is an offshore consultant that executes workability studies for its clients. As technologies emerge, to remain on the front row, studies are done to find and fill the knowledge gaps within the offshore energy sector. Floating solar parks are such a novelty which still needs further exploration. Therefore, this thesis was initiated to map the involved actors of the industry and identify the issues they are facing.

Mocean Offshore regularly uses OrcaFlex for their calculations. OrcaFlex is a commercial software tool built by Orcina.[7] It is used for dynamic analysis of offshore marine systems. OrcaFlex uses undisturbed waves in their simulations, which means that the structure is only influenced by the wave, but not vice versa. The shape of the wave will thus not deform. This key aspect of the software is relevant, as VLFSs have some degree of wave deformation. Mocean Offshore wants to understand in what regime wave deformation occurs and when an undisturbed wave is applicable for the calculations of VLFSs. This research tries to find an answer with the use of a finite element model where a fluid structure interaction problem is solved.

1.7. Research question

The insights obtained during the interviews showed that the problems faced by the inland water body installations were more of a mechanical challenge. This research mainly focuses on the hydrodynamic aspects of the floating solar technology as part of VLFSs. The offshore challenges, on the other hand, have a stronger relation to this topic. The current techniques of floating PV used for inland waterbodies cannot be used one to one for offshore installations. A VFFS, however, is a type of structure which is a promising alternative for the application of floating solar panels. Several parties, like TNO, TU Delft, Equinor and Moss Maritime are doing research in this field by making different designs. (De Jong and Soppe, 2020)

A unique characteristic of VFFS is its flexibility compared to the incident waves. A lot of research has been done on VLFS, particularly describing the dispersion relation of hydroelastic waves. However, this mainly concerned stiff structures. Therefore, there is still a knowledge gap within the very flexible regime. Schreier and Jacobi (2020b) are executing physical experiments with VFFS in a towing tank. As a comparison to their work this research focuses on a computational alternative. This has several advantages, such as scalability and time efficiency. Furthermore, different floating shapes and material parameters can be tested. Finally, the model will also be suitable for calculations of stiffer VLFSs such as ice floes and floating islands. In a search to find a proper modelling tool, Oriol Colomes, working

[7] Orcina (2021), OrcaFlex, Ulverston https://www.orcina.com/orcaflex/

at the TU Delft recommended a module within the programming language Julia called Gridap. He has been involved in developing this module for several years. Gridap is a Finite Element Method (FEM) toolbox which provides solving partial differential equations and is able to capture this Fluid Structure Interaction (FSI) problem. This leads to the following research question:

> *What is the performance of a Fluid Structure Interaction Finite Element Method model based on linear potential flow theory compared to experimental research and the analytical dispersion relation of hydroelastic waves?*

1.8. Scope

The research focuses on the hydrodynamics of the structure, as the structure is in motion due to the wave forces. In an aim to describe the structural behaviour of the VFFS, the response of the structure imposed by the incident waves is investigated. This interaction is known as the hydroelastic dispersion relation. This will be the main topic of interest.

The FEM model has been built with the assumption of linear potential flow theory. This is often used in ocean engineering due to the assumptions of inviscid and irrotational flow which can be made. The linear system has its drawbacks, as it is only able to describe linear waves, such as regular and irregular waves. This means that non-linear phenomena, such as breaking waves or asymmetrical waves cannot be modelled.

The structure itself is based on the linear Euler-Bernoulli beam. This is only valid for small vertical deflections and cannot capture large deformations. Therefore, the steepness of the incident waves waves should be limited. Schreier and Jacobi (2020b) used a wave steepness of $\xi = \frac{\lambda_i}{50}$ being ξ the wave amplitude. This is also used as a starting point in the report.

For the application of floating PV, it will not be uncommon that the structure exists of a composite material. Although the main material is expected to be a rubber kind material. On top of it, the thin-film solar panels need to be applied. Also, the material might be reinforced by a steel framework to attach the mooring to. This complicates the problem, and as these composite materials are still not specified by any literature, this research assumes a uniform material for the structure.

Apart from the topics that are within the scope, it is also convenient to show the fields of interest that will not be discussed nor answered in this research. As was mentioned earlier, the focus lies within the hydrodynamics. That means that electrical aspects such as circuit layout or the inverter location will not be discussed. Furthermore, mechanical aspects such as connection types are also out of the scope of this thesis. Finally, the location of the floating PV is not discussed extensively. The goal of this research is to see if a computational linear FEM model is a worthy alternative to the existing analytical formulations and experimental research. This study can be done independently of a location in the world. Too many factors, such as the amount of solar radiation around the globe, distance to an existing power cable or local subsidies that make it more affordable to build floating PV, influence the location of choice. However, the wave loads on the VFFS will be based on realistic scenarios existing in potential vacant spots.

1.9. Structure

To give a good overview of the structure of the report a flowchart is presented in Figure 1.6. This first chapter introduces the challenges related to (offshore) floating solar and explains the basics behind fluid structure interactions.

The next chapter covers the full analytical mathematics behind the VFFS. It shows how a VFFS could be simplified to a dynamic Euler-Bernoulli beam and the hydroelastic wave dispersion relation is derived.

The third chapter converts this analytical problem into a numerical problem by rewriting the set of equations to the weak formulation. The Finite Element Method is subsequently used to solve it.

Once the boundary conditions of the model are established, the numerical model is set up and tested. The parameters of the model are tweaked to give reliable results, which includes the definition of the grid resolution, the amount of damping at the end of the model and checking if the system is energy conservative once it reaches its steady-state.

Once this has been done, the model is ready to be used for test runs. Several tests will be executed to better understand the fluid structure interaction. First, Schreier and Jacobi (2020b) experiments in the towing tank will be run. Secondly, a full scale offshore scenario is tested to see how a VFFS would interact with several design ocean waves and a governing lake wave. Next, two material parameters are tested to the same five design waves; the stiffness and the density of the structure are altered to see how they influence the hydroelastic response. Finally, a separate test run is dedicated to the draught of the structure. Little research has been done on flexible structure with large draughts. Also, the analytical theory has not captured this regime and wave shortening is likely to occur, which has several consequences that will be explained later in this report.

Finally, the results from the test runs are evaluated and the observations are discussed. With the new insights using the numerical model, it is tried to get a better understanding of how a floating structure responds to the incident waves.

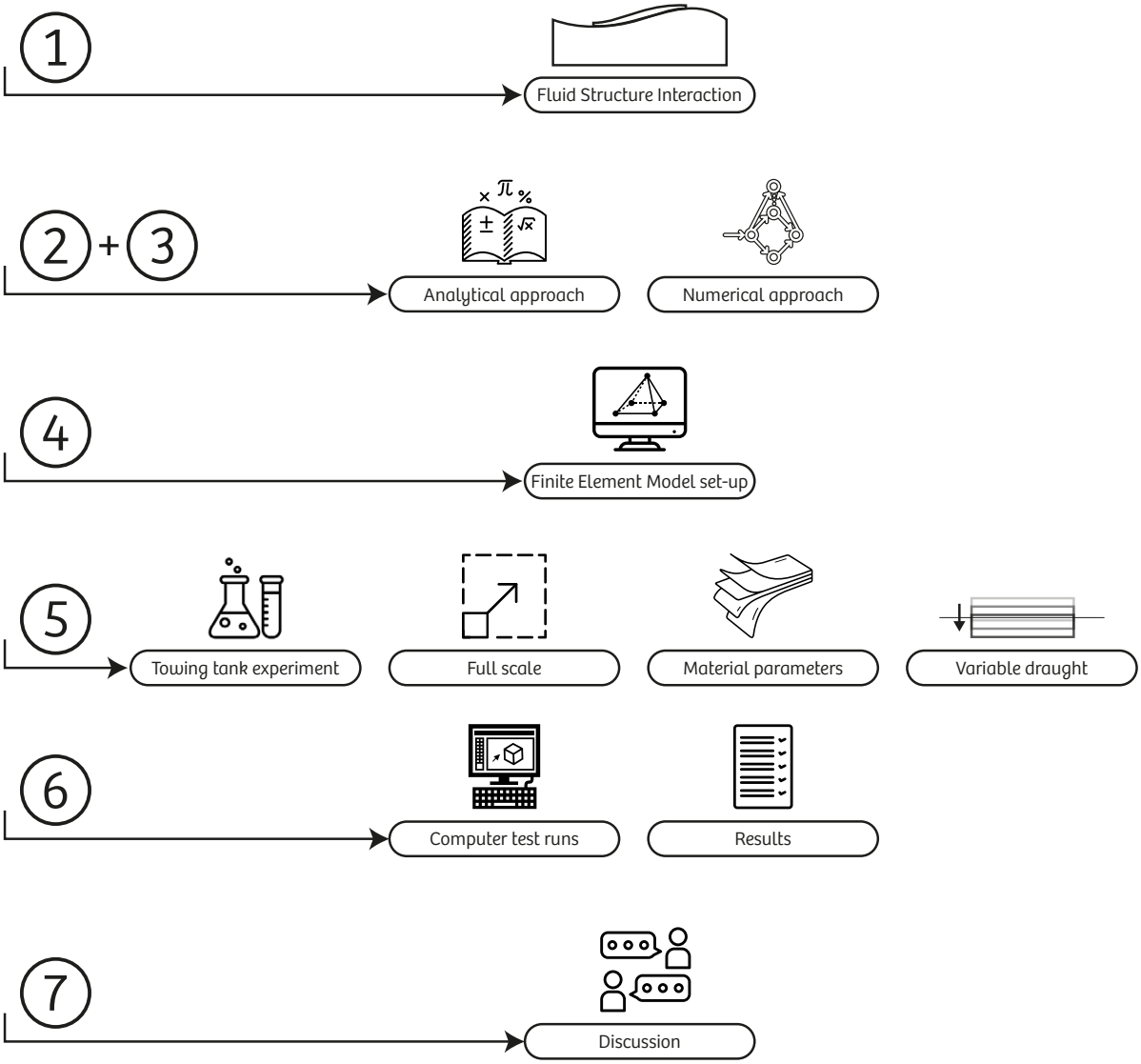

Figure 1.6: Flowchart that shows the structure of the report.

Figure 1.7: Persona tree of people which have been interviewed. Each person is identified by name, title, company and asset for this research.

2

Analytical Method

This chapter will give guidance through the mathematics that will be used to describe the problem; in this case a floating one-dimensional flexible structure in a 2D environment. The more general mathematics behind widely accepted concepts are only briefly discussed (potential flow, linear wave theory). However, the floating structure, which is based on a dynamic Euler-Bernoulli beam, and its dispersion relation is derived, as this was not found online elsewhere.

2.1. Potential flow

In the FEM model, the considered flow is potential flow. The theory of this type of flow has been described extensively by others, such as (Kundu and Cohen, 1987). Therefore, the theory is only briefly explained in this report.

Potential flow is based on the principle that the velocity field can be described by the spatial derivatives of a scalar function, this is called the potential function. Moreover, the fluid is considered to be incompressible. This consideration implies that the divergence of the velocity is equal to zero. The potential function then satisfies the Laplace equation:

$$\begin{cases} \nabla \cdot \vec{u} = 0 \\ \nabla \phi = \vec{u} \end{cases} \Leftrightarrow \nabla \cdot (\nabla \phi) = \Delta \phi = 0 \quad \text{in} \quad \Omega \tag{2.1}$$

Furthermore, the potential flow is characterised by irrotational flow, which implies that the curl of the velocity field is equal to zero. This is only valid if viscous forces are absent. This also implies that viscous terms cannot be described with potential flow theory. However, in this report ocean waves at the free surface are examined; also called wind waves. These waves are characterised by the same principles as potential flow, being inviscid, irrotational and incompressible.

2.2. Fluid boundary conditions

To determine the fluid domain, boundary conditions are imposed on each side of the model. The domain consists of three impermeable sides (Γ_L, Γ_{btm} and Γ_R) and a free surface (Γ_{fs}). The boundary condition for the structure (Γ_b) is discussed in the next section. For an overview, the model is visualised in Figure 2.1.

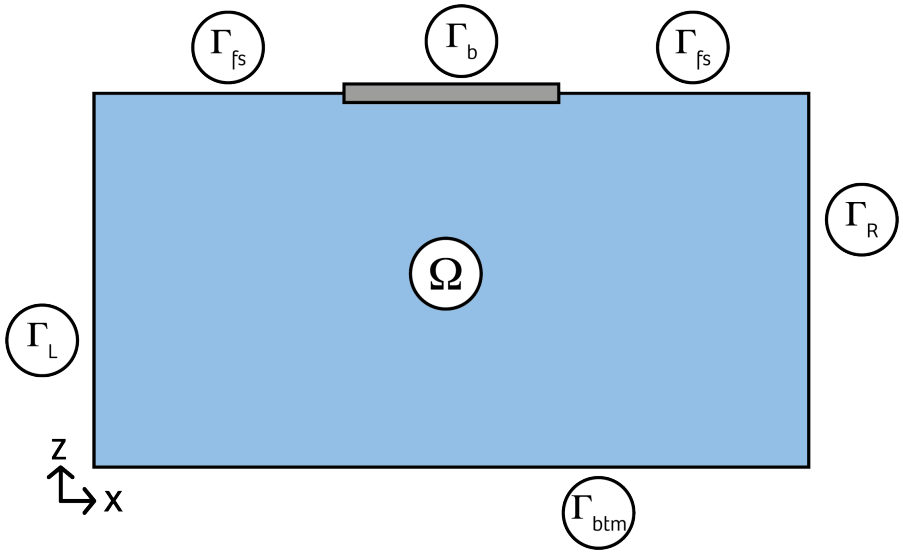

Figure 2.1: Two-dimensional fluid domain (Ω) with a floating 1D Euler-Bernoulli beam at the free surface. Boundaries are indicated with Γ and their respected subscript.

The first boundary condition of the model is located on the sides and on the bottom. Here it is assumed that these boundaries are impermeable. This is called the sea bed boundary condition and given as:

$$\nabla\phi \cdot \vec{n} = 0 \quad \text{on} \quad \Gamma_L \cup \Gamma_{btm} \cup \Gamma_R \quad \text{sea bed b.c.} \tag{2.2}$$

Where $\vec{n}$ is the unit normal vector to the boundary facing outwards.

The second boundary condition is the dynamic free surface boundary condition which states that the pressure above the free surface is constant and equal to zero. Using Bernoulli's equation in the linearised form and assuming that there is no y-direction (since the model is only 2D), the boundary condition is given as:

$$\frac{\delta\phi}{\delta t} + g\eta = 0 \quad \text{on} \quad \Gamma_{fs} \quad \text{dynamic free surface b.c.} \tag{2.3}$$

Where g is the gravity constant and η is the surface elevation. With this boundary condition and assuming that they are imposed at $z = 0$, the formula of the wave potential can be derived and is equal to:

$$\phi = \frac{\xi_i g}{\omega} \cdot \frac{\cosh\left(k_i(d+z)\right)}{\cosh\left(k_i d\right)} \cdot \sin\left(k_i x - \omega t\right) \tag{2.4}$$

Where ξ_i, ω and k_i are the amplitude, the angular frequency and the wave number of the incident wave, respectively and d the water depth.

Finally, the third boundary condition is the kinematic free surface boundary condition which describes that the vertical velocity of the free surface has to be equal to the vertical motion of the flow and is given as follows:

$$\frac{\delta\phi}{\delta z} = \frac{\delta\eta}{\delta t} \quad \text{on} \quad \Gamma_{fs} \quad \text{kinematic free surface b.c.} \tag{2.5}$$

Using this boundary condition the wave number can be related to the wave frequency. By differentiating the dynamic free surface boundary condition and inserting the kinematic free surface boundary condition one obtains the Cauchy-Poisson condition:

$$\frac{\delta\phi}{\delta z} + \frac{1}{g}\frac{\delta^2\phi}{\delta t^2} = 0 \tag{2.6}$$

Substituting Equation 2.4 into Equation 2.6 gives the dispersion relation:

$$\omega^2 = g k_i \tanh\left(k_i d\right) \tag{2.7}$$

Now, the amplitude of the wave (ξ_i) can be chosen freely, considered that the amplitude is small compared to the wavelength (λ) and water depth (d); this is called Airy wave theory.

The remaining boundary which has not been discussed yet, is the VFFS on the free surface (Γ_b). The structure is considered to be a floating Dynamic Euler-Bernoulli beam.

2.3. Dynamic Euler-Bernoulli beam boundary condition

Next to the fluid domain, the VFFS is modelled. Tsubogo and Okada (1998) proposed the hydroelastic wave dispersion as in Equation 2.8.

$$\left[1-\left(\frac{\omega}{\omega_0}\right)^2+\left(\frac{k}{k_p}\right)^4\right]k\tanh kd=\omega^2/g \tag{2.8}$$

With angular frequency (ω), natural heave frequency (ω_0), hydroelastic wave number (k), characteristic wave number (k_p), water depth (d) and gravity constant (g).

$$\omega_0=\sqrt{\frac{\rho_w g}{m}} \tag{2.9}$$

With mass per horizontal unit area (m).

$$k_p=\frac{2\pi}{\lambda_c}=\left(\frac{\rho_w g B}{EI}\right)^{\frac{1}{4}} \tag{2.10}$$

However, a full derivation was not included. Therefore, this equation has been rededucted by using the 1D dynamic Euler-Bernoulli beam. This equation holds if loads are purely lateral and the structure has small deflections. The general dynamic Euler-Bernoulli equation describes the relation of the deflection of the beam (w) and the external force (f) on it as a function of time. Given as:

$$\frac{d^2}{dx^2}\left(EI\frac{\delta^2 w}{\delta x^2}\right)=-\mu\frac{\delta^2 w}{\delta t^2}+f(x) \tag{2.11}$$

With bending stiffness EI and mass per unit length μ.

If the bending stiffness is constant, this equation will simplify to:

$$EI\frac{\delta^4 w}{\delta x^4}=-\mu\frac{\delta^2 w}{\delta t^2}+f(x) \tag{2.12}$$

Where E denotes the Young's modulus and I the moment of inertia. Assuming that the beam is shaped as a rectangle, it is given as:

$$I=\frac{Bh^3}{12} \tag{2.13}$$

However, the 2D model assumes that the incident waves are infinitely wide as there is no width in the model. This also changes the bending stiffness constant and Equation 2.13 divided by the width (B) of the structure and is rewritten to:

$$I_{2D}=\frac{\frac{Bh^3}{12}}{B}=\frac{h^3}{12} \tag{2.14}$$

As the force on the beam is given by the pressure of the fluid, the dynamic free surface boundary condition changes to a non-zero equation, and the water density (ρ_w) is reintroduced:

$$-\rho_w\frac{\delta\phi}{\delta t}-\rho_w g\eta=p \tag{2.15}$$

With pressure p being:

$$p=\rho_b h\frac{\delta^2\eta}{\delta t^2}+\frac{EI}{B}\frac{\delta^4\eta}{\delta x^4} \tag{2.16}$$

Where ρ_b and h are the density and the thickness of the structure, respectively. Resulting in the altered dynamic free surface boundary condition:

$$\rho_b h \frac{\delta^2 \eta}{\delta t^2} + \frac{EI}{B} \frac{\delta^4 \eta}{\delta x^4} + \rho_w \frac{\delta \phi}{\delta t} + \rho_w g \eta = 0 \quad \text{on} \quad \Gamma_b \tag{2.17}$$

Rewriting this equation and inserting the same governing kinematic free surface boundary condition results in an altered Cauchy-Poisson condition with an added factor; three terms in between brackets:

$$\left(\frac{\rho_b h}{\rho_w g} \frac{\delta^2 \eta}{\delta t^2} + \frac{EI}{\rho_w g B} \frac{\delta^4 \eta}{\delta x^4} + 1 \right) g \frac{\delta \phi}{\delta z} = -\frac{\delta^2 \phi}{\delta t^2} \tag{2.18}$$

Assuming that the solution of the free surface elevation is a wave as given in 2.19:

$$\eta = \xi_b \cos(k_b x - \omega t) \tag{2.19}$$

With ξ_b and k_b the amplitude and the wave number of the hydroelastic wave, respectively. Its second derivative in time and fourth derivative in space are given as:

$$\begin{aligned} \eta_{tt} &= -\omega^2 \xi_b \cos(k_b x - \omega t) \\ \eta_{xxxx} &= k_b^4 \xi_b \cos(k_b x - \omega t) \end{aligned} \tag{2.20}$$

Inserting these wave terms in Equation 2.18 and assuming initial conditions ($x = 0, t = 0$) the equation is given as:

$$\left(-\frac{\omega^2 \rho_b h}{\rho_w g} + \frac{k_b^4 EI}{\rho_w g B} + 1 \right) g \frac{\delta \phi}{\delta z} = -\frac{\delta^2 \phi}{\delta t^2} \tag{2.21}$$

Rewriting this equation for a simplified representation results in:

$$Kg \frac{\delta \phi}{\delta z} = -\frac{\delta^2 \phi}{\delta t^2} \tag{2.22}$$

With K being:

$$K = 1 + \frac{k_b^4 EI}{\rho_w g B} - \frac{\omega^2 \rho_b h}{\rho_w g} \tag{2.23}$$

Or in an alternate form:

$$K = 1 + \left(\frac{k_b}{k_p} \right)^4 - \left(\frac{\omega}{\omega_0} \right)^2 \tag{2.24}$$

With:

$$\begin{aligned} k_p &= \left(\frac{\rho_w g B}{EI} \right)^{\frac{1}{4}} \\ \omega_0 &= \sqrt{\frac{\rho_w g}{\rho_b h}} \end{aligned} \tag{2.25}$$

From the altered Cauchy-Poisson equation the hydroelastic wave dispersion is retrieved and given as:

$$\omega^2 = Kg k_b \tanh(k_b d) \tag{2.26}$$

Note the difference between Equation 2.7 and 2.26 where the frequency remains unchanged. Equally, the wave potential (ϕ) is given as:

$$\phi(\vec{x}, t) = \frac{K \xi_b g}{\omega} \cdot \frac{\cosh(k_b(d + z))}{\cosh(k_b d)} \cdot \sin(k_b x - \omega t) \tag{2.27}$$

As the potential wave equation (Equation 2.4) and the hydroelastic potential wave equation (Equation 2.27) are compared, the only difference between them is the factor K. Therefore, K can be used as a transfer function to compute the difference in wave number between the incident waves and the hydroelastic waves.

Not only the wavelength changes when the incident wave deforms into the transmitted hydroelastic wave, but also the amplitude changes. Tsubogo and Okada (1998) showed that this relation can be given by the fact that the energy flux just next to the beam is equal to the energy flux on the edge of the beam. The relation is given as follows:

$$R = \frac{\xi_b}{\xi_i} = \frac{2k_b}{k_i + k_b}\sqrt{\frac{1 + \frac{k_i d}{\cosh(k_i d)\sinh(k_i d)}}{KN}} \tag{2.28}$$

With N being:

$$N = 1 + \frac{k_b d}{\cosh(k_b d)\sinh(k_b d)} + \frac{4}{K}\left(\frac{k_b}{k_p}\right)^4 \tag{2.29}$$

However, Tsubogo and Okada (1998) simplified the solution by making a zero-draught assumption for the structure ($\omega \ll \omega_0$), which implies that the density of the VLFS is very low compared to the water density. Tsubogo also only looked at waves shorter than the natural heave period of the VLFS ($\omega < \omega_0$), which implies that there no resonance will occur.

2.4. Wave energy flux

In order to check if the numerical model is energy conservative, an energy flux balance is set up and the incident wave energy flux (P_i) is compared with the hydroelastic wave energy flux (P_b). The energy flux is the product of the wave energy and the group velocity of the wave. First the energy of the incident wave is calculated. The total energy is split into two terms; potential energy and kinetic energy. The potential component is calculated by integrating the pressure over the wavelength:

$$E_{pot,i} = \int_0^{\lambda_i}\int_0^{\eta} \rho_w g z dz dx = \int_0^{\lambda_i} \frac{1}{2}\rho_w g \xi_i^2 \sin^2(k_i x - \omega t) dx = \frac{1}{4}\rho_w g \xi_i^2 \lambda_i \tag{2.30}$$

Kinetic energy is calculated by integrating the horizontal (u) en vertical (w) velocity components as follows:

$$E_{kin,i} = \frac{1}{2}\rho_w \int_0^{\lambda_i}\int_{-d}^{0} (u_i^2 + w_i^2) dz dx \tag{2.31}$$

Where, for incident waves, u and w are defined as the spatial derivatives of the wave potential in their respected direction:

$$\begin{aligned} u_i &= \omega \xi_i \frac{\cosh(k_i(d+z))}{\sinh(k_i d)} \cos(k_i x - \omega t) \\ w_i &= \omega \xi_i \frac{\sinh(k_i(d+z))}{\sinh(k_i d)} \sin(k_i x - \omega t) \end{aligned} \tag{2.32}$$

Inserting the velocity components of the incident waves into Equation 2.31 results in:

$$E_{kin,i} = \frac{1}{4}\rho_w g \xi_i^2 \lambda_i \tag{2.33}$$

The kinetic and potential energy components together form the total energy of the incident wave:

$$E_i = E_{kin,i} + E_{pot,i} \tag{2.34}$$

For the hydroelastic wave, the potential and kinetic energy terms of the incident wave can be rewritten by using the dispersion factors K and R:

$$E_{pot,b1} = \frac{1}{4}\rho_w g \xi_b^2 \lambda_b = \frac{1}{4}\rho_w g R^2 \xi_i^2 K \lambda_i \tag{2.35}$$

$$E_{kin,b1} = \frac{1}{4}\rho_w g \xi_b^2 \lambda_b = \frac{1}{4}\rho_w g R^2 \xi_i^2 K \lambda_i \tag{2.36}$$

As:

$$K = \frac{k_i}{k_b} \cdot \frac{\tanh(k_i d)}{\tanh(k_b d)}$$
$$R = \frac{\xi_b}{\xi_i} \tag{2.37}$$

As the altered dynamic boundary condition contains two more terms, two extra components of the kinetic and potential energy of the VFFS need to be taken into account for a full energy balance:

$$E_{pot,b2} = \frac{1}{4}\frac{EI}{B}k_b^4\xi_b^2\lambda_b = \frac{1}{4}\frac{EI}{B}\frac{k_i^4}{K^4}R^2\xi_i^2 K\lambda_i = \frac{1}{4}\frac{EI}{B}\frac{k_i^4}{K^3}R^2\xi_i^2\lambda_i \tag{2.38}$$

$$E_{kin,b2} = \frac{1}{4}\rho_b h\omega^2\xi_b^2\lambda_b = \frac{1}{4}\rho_b h\omega^2 R^2\xi_i^2 K\lambda_i \tag{2.39}$$

The total hydroelastic wave energy thus becomes:

$$E_b = E_{kin,b1} + E_{pot,b1} + E_{kin,b2} + E_{pot,b2} \tag{2.40}$$

As the energy components are known, the remaining term to calculate the energy flux is the group velocity (c_g). This is the speed of the energy that is transferred by the waves and is equal to the phase speed (c) times the dispersion parameter (n):

$$c_g = nc = n\frac{\omega}{k} \quad \text{with} \quad n = \frac{1}{2}\left(1 + kd\frac{1-\tanh^2 kd}{\tanh kd}\right) \tag{2.41}$$

With $n = 0.5$ for deep water and $n = 1$ for shallow water.

For the incident wave the group velocity is equal to:

$$c_{g,i} = nc_i = n\frac{\omega}{k_i} \tag{2.42}$$

For the hydroelastic wave, the group velocity can be calculated from the dispersed wave number (k_b) and assuming that the frequency is constant:

$$c_{g,b} = nc_b = n\frac{\omega}{k_b} = n\frac{\omega}{\frac{k_i}{K}} = Kc_{g,i} \tag{2.43}$$

The wave energy flux is obtained by the product of the wave energy and the group velocity and should be equal, resulting in:

$$P_i = P_b = E_i \cdot c_{g,i} = E_b \cdot c_{g,b} \tag{2.44}$$

If Equation 2.44 is satisfied, the numerical model is is coercive, meaning that energy is conserved. The importance of coercivity will be further explained in the next chapter when the shape functions of the Finite Element model are discussed.

2.5. Structural stiffness

To put the numerical test runs into perspective in relation to the towing tank results or other previously researched VLFSs, the characteristic length of a structure will be used as introduced by Suzuki et al. (2007). Equation 2.45 shows a relation of the bending stiffness EI and the hydrostatic stiffness:

$$\lambda_c = 2\pi\left(\frac{EI}{\rho_w g B}\right)^{\frac{1}{4}} \tag{2.45}$$

By dividing the length of the structure over the characteristic length the amount of elasticity is defined as shown in Figure 1.4.

3

Finite Element Method

The Finite Element Method (FEM) is a numerical method to solve partial differential equations. The method subdivides the large complex system into smaller parts; finite elements. This spatial discretisation is done by creating a mesh. This mesh is the numerical domain with a finite number of nodes. In this method an approximation of each element is evaluated to find the unknown function. Finally, the solutions of all elements are assembled to form a full set of equations which represent the full model. To get a full understanding of how the model has been built, Appendix B contains a tutorial which explains every aspect.

3.1. Weak form

The notation for the Finite Element Method is different than the standard partial differential equations. The regular form, also called the 'strong form', as given in the previous section uses fractions to describe the problem. However, for FEM, the so called 'weak formulation' is used. To rewrite an equation into the weak form, it is integrated by parts. An example is shown how to convert the Laplace equation (Equation 2.1) from the strong form into the weak form.

The governing Laplace equation in the two-dimensional domain Ω reads:

$$\nabla^2 \phi = 0 \quad \text{in} \quad \Omega \tag{3.1}$$

And the accompanying boundary condition is given as:

$$\nabla \phi \cdot \vec{n} = f \quad \text{on} \quad \Gamma \tag{3.2}$$

Where $\vec{n}$ is the normal unit vector and f being a constant.

The aim of this problem is to solve the Laplace equation. To do this, a solution space V is specified. It is tried to find a solution for $\phi \in V$ such that $a(\phi, g) = b(g) \forall g \in V$. Here $g(\vec{x})$ is a so called test function. To apply this on the Laplace equation, the equation is multiplied by the test function. Subsequently, this product is integrated over the domain (Ω):

$$\int_\Omega \nabla^2 \phi \cdot g d\Omega = 0 \tag{3.3}$$

Equation 3.3 is integrated by parts:

$$-\int_\Omega \nabla \phi \cdot \nabla g d\Omega + \int_\Gamma g \left(\nabla \phi \cdot \vec{n}\right) d\Gamma = 0 \tag{3.4}$$

By integrating by parts, one ends up with a interior term over the Ω-domain and a boundary term one dimension lower. This is indicated by the Greek letter Γ; the boundary of the domain. If Ω were a three-dimensional domain, the boundary term would be a two-dimensional term representing for example a

plane.

These terms are split over the bilinear function $a(\phi, g)$ and linear function $b(g)$, in which is assumed that $a(\phi, g) = b(g)$. Note that the boundary condition from Equation 3.2 has been inserted in the boundary term, which makes Equation 3.6 only a function of $g(\vec{x})$.

$$a(\phi, g) = \int_{\Omega} \nabla\phi \cdot \nabla g d\Omega \tag{3.5}$$

$$b(g) = \int_{\Gamma} g f d\Gamma \tag{3.6}$$

This process will be used throughout the report when defining the conditions for the FEM model. As this notation is spacious, a more compact format will be used; Equations 3.5 and 3.6 are rewritten as:

$$a(\phi, g) = (\nabla\phi, \nabla g)_{\Omega} \tag{3.7}$$

$$b(g) = (g, f)_{\Gamma} \tag{3.8}$$

3.2. Newmark-beta method

To solve the FEM model, time integration is applied. There are several options available to solve sets of equations, each with their own (dis)advantages, but there are two main categories; explicit and implicit schemes. The explicit scheme uses only the current time to calculate the next time step. Whereas, the implicit scheme uses both the current time as well as the next time step to solve for the next time step. The main difference between the two, is that an explicit scheme could explode if the chosen time step is too large. This is called numerical stability. The implicit scheme does not have this issue, which means that it can use larger time steps. However, it is computational more expensive, as the system needs to be solved for both the current state as well as the state of a later time. Whether one of the two is better depends on the problem to be solved. Equation 3.9 shows an example of the difference between an implicit and an explicit scheme. Where transfer function F_1 only takes the current state as an parameter, F_2 also takes the future state as one of its parameters.

$$\begin{aligned} y_{t+1} &= F_1(y_t) && \text{explicit} \\ y_{t+1} &= F_2(y_t, y_{t+1}) && \text{implicit} \end{aligned} \tag{3.9}$$

Next to numerical stability, there is the order of accuracy. This is defined by the error of the solution of the system. A higher order of accuracy leads to better results, but comes at an expense of computational time. Systems with higher orders of accuracy generally are more computational expensive. One needs to find an optimum between accuracy and time.

As the system of equations in this model contain both potential flow as well as an Euler-Bernoulli beam, it is important to choose a numerical time integration scheme that fits both PDEs. As the dynamic beam equation consists of a second-order time derivative term, it would be convenient to use a numerical time integration scheme that can cope with this. In 1959, Nathan M. Newmark developed a method to solve dynamic systems. (Newmark, 1959) The structural equation is a second order ordinary differential equation system:

$$\mathbf{M}\ddot{y} + \mathbf{C}\dot{y} + f^{int}(y) = f^{ext} \tag{3.10}$$

With mass matrix $\mathbf{M}$, damping matrix $\mathbf{C}$, internal forces f^{int} and external forces f^{ext}. Based on this equation, the full system is derived as Newmark explains (Newmark, 1959):

$$\begin{aligned} \dot{y}_{n+1} &= \dot{y}_n + (1-\gamma)\Delta t\ddot{y}_n + \gamma\Delta t\ddot{y}_{n+1} \\ y_{n+1} &= y_n + \Delta t\dot{y}_n + \frac{\Delta t^2}{2}\left((1-2\beta)\ddot{y}_n + 2\beta\ddot{y}_{n+1}\right) \\ \mathbf{M}\ddot{y}_{n+1} &+ \mathbf{C}\dot{y}_{n+1} + f^{\text{int}}(y_{n+1}) = f^{\text{ext}}_{n+1} \end{aligned} \tag{3.11}$$

This system of equations contains two parameters β and γ, which need to be specified in order to use the method. Newmark states that unless $\gamma = 0.5$, spurious damping occurs in the system. Furthermore, from a stability analysis it follows that if $\beta = 0.25$, the system is unconditionally stable. (Newmark, 1959) The system with these settings is called the Average constant acceleration (Middle point rule) and will be used for the calculations of the FEM model.

3.3. Damping zone

The incident waves in the model start on the left hand side and travel toward the right hand side of the model. Preferably, the computational domain is not much longer than the domain of interest, which is in this case the VFFS. Increasing the domain would only increase the computation time. There are two alternatives to avoid reflecting waves on the boundary. One way is to let the waves radiate through the outlet, which asks for a non-reflective boundary condition. Another option is to cancel the waves in a damping zone. Both methods were investigated and it was found that adding a proper non-reflective boundary condition was hard to find for the potential flow equation. Moreover, adding a non-reflective boundary condition also results in small errors. (Thompson and Huan, 2000) Adding a damping zone, however, was easy to implement and several options were made available by the work of Min Woo Kim. (Kim et al., 2014) In experimental research this could be done by creating a beach. The decreased water depth will cause the waves to break and the energy is dissipated. For a computer model, there is an alternative called artificial damping. This could be compared to adding a viscous term on the end of the domain (damping zone). The wave energy is in that way dissipated.

Kim et al. (2014) released a paper where different alternatives for artificial wave damping are compared. The different alternatives distinguished themselves from each other on where the damping terms were applied on; either on the kinematic or dynamic boundary condition or both. In his paper, the fourth method jumped out as being the second best damping method, very close to the winning method number five. However, method four was much easier to implement. Therefore, method four has been chosen as the preferred damping method. Its accuracy is later discussed in the methodology when the parameters are evaluated.
The damping factor consists of two components; a damping coefficient (μ_1) and a dispersion parameter (μ_2). The damping coefficient determines the rate of damping and needs to be chosen iteratively. The dispersion parameter also is a damping term, but it couples the potential with the elevation. To avoid distortion of the wave frequency, the damping coefficient (μ_1) and the dispersion parameter (μ_2) are linked with the following ratio:

$$\mu_2 = -\frac{\mu_1^2}{4} \tag{3.12}$$

The dynamic boundary condition of the damping zone remains unchanged, but the kinematic free surface boundary conditions in the damping zone is as follows:

$$\frac{\delta\eta}{\delta t} - \frac{\delta\phi}{\delta z} + \mu_1\eta + \frac{\mu_2}{g}\phi = 0 \quad \text{kinematic b.c.} \tag{3.13}$$

The intensity of the damping factor varies in space. As the waves travel further into the damping zone the damping factor increases. To prevent wave reflection, the slope of the ramp should be almost equal to zero at the start of the damping zone. Therefore, there is chosen to use Shape 1 from Kims paper and is given as:

$$\mu_1(x) = \mu_0\left[1 - \cos\left(\frac{\pi}{2}\left(\frac{x - x_d}{L_d}\right)\right)\right] \tag{3.14}$$

With $(x - x_d)$ being the local length of damping zone and L_d the total length of the damping zone.

3.4. Time step resolution

In numerical modelling, the time step is often related to the resolution of the grid. For explicit time integration schemes this is mandatory to get a stable result. For implicit schemes, this is not necessary as implicit schemes are by definition unconditionally stable. A proper way to describe to relate the time step (Δt) to the resolution of the grid (Δx) is by using the Courant-Friedrichs-Lewy (CFL) condition. It states that the time step should be smaller than a certain time, in order to reach convergence and is necessary for time explicit scheme to prevent incorrect results. Equation 3.15 shows this relation. Where C is the dimensionless Courant number and c the celerity of the wave:

$$\Delta t \leq C\frac{\Delta x}{c} \tag{3.15}$$

For explicit schemes the typical maximum Courant number is one. Larger values imply that the phase speed of the wave from the analytical domain travels faster than the numerical domain can cope with. This results in potential loss of information and subsequently in incorrect results. Figure 3.1 visually explains what happens if the Courant number exceeds this value.

Although the CFL-condition should be strictly followed for explicit time integration schemes, it is a convenient tool to guess the initial time step for implicit schemes as well. Furthermore, it clarifies the resolution of the time step compared to the spatial domain and is therefore used in the set-up of the numerical model.

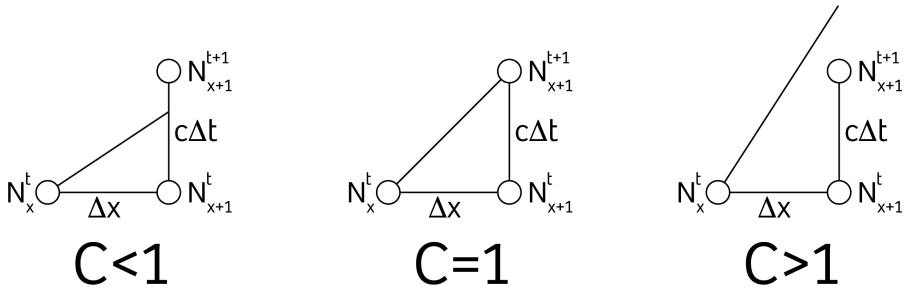

Figure 3.1: Three cases for different Courant number domains. If the Courant number is smaller or equal to one, the system is stable. If the Courant number exceeds one, the system is unstable and will explode.

3.5. Julia

The Julia model is written with the aid of Gridap (Badia and Verdugo, 2020). Gridap is a package that contains a library of functions that provide a set of tools for grid-based approximations of partial differential equations (PDE). It can be used for linear and nonlinear PDE systems. The choice for Gridap was based on numerous reasons. Gridap has a very expressive API allowing to solve PDEs with very few lines of code. The weak formulation can be written nearly one to one. Therefore, the notation is well understood by readers and writers. Moreover, Oriol Colomes, assistant professor at the TU Delft, who is involved in Fluid Structure Interactions, collaborates to improve this package. As there is still little documentation online, he is a good source of information to guide the way. Finally, Julia is one of the fastest programming languages at the moment.[1] As Julia is a compiled language, it runs as fast as Fortran or C, but at the same time, it has the look and feel of scripting languages like Matlab and Python.

The 2D Julia model is purely based on partial differential equations written in the programming language Julia. This model will try to mimic the experimental research of Schreier, upon which the differences will be evaluated. The model is based on the Finite Element Method as explained in the previous chapter. This model written from scratch using the module named Gridap and is visualised in Figure 3.2.

[1] (2019), Nature, Julia: come for the syntax, stay for the speed, https://www.nature.com/articles/d41586-019-02310-3

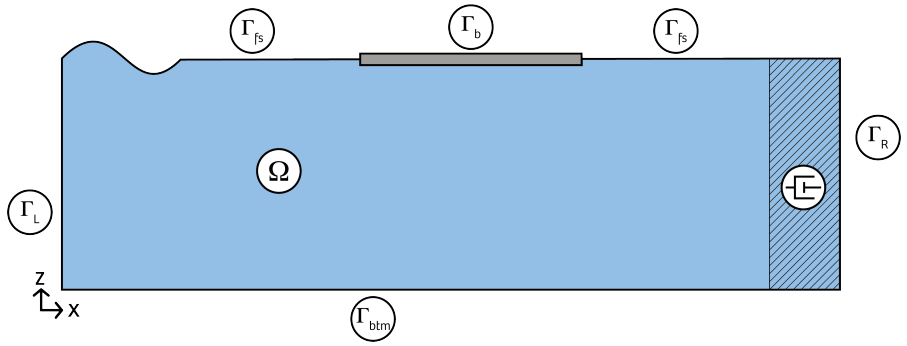

Figure 3.2: Two-dimensional fluid domain (Ω) with a floating 1D Euler-Bernoulli beam at the free surface. Waves are induced by a vertical velocity profile from the left. On the right hand side, an artificial damping zone is implemented to cancel the wave energy. Boundaries are indicated with Γ and their respected subscript. Note that the boundary of the damping zone Γ_{dz} is part of the free surface boundary.

The model consists of four different zones. At boundary Γ_L, a vertical velocity profile is imposed. This profile is given by the horizontal velocity component of Airy wave theory, as written in Equation 3.29. This induces the incident waves on the free surface which travel towards the structure that is positioned in the second zone. Right from the structure there is again a free surface. This continues until the artificial damping zone reached which cancels the wave energy. There is no direct physical comparison with this damping zone, but it could be compared to a beach where the wave energy dissipates.

The partial differential equations which are the building blocks will be briefly repeated and their weak formulation is given. This will be done twice; one time for a fluid domain only. Subsequently, the beam boundary is added. Both formulations will be given as tests will be run, with and without the structure. The equation that describes the potential flow is the Laplace equation and reads:

$$\Delta\phi = 0 \tag{3.16}$$

With the accompanying kinematic boundary condition on the free surface:

$$\nabla\phi \cdot \vec{n} = \eta_t \tag{3.17}$$

For the other boundaries (Γ_L, Γ_{btm} and Γ_R) the kinematic boundary condition states that they are impermeable:

$$\nabla\phi \cdot \vec{n} = 0 \tag{3.18}$$

The dynamic boundary condition of the free surface is equal to the pressure:

$$p = -\rho_w\phi_t - \rho_w g\eta \tag{3.19}$$

The dynamic Euler-Bernoulli beam is given as:

$$p = \rho_b h\eta_{tt} + \frac{EI}{B}\Delta^2\eta \tag{3.20}$$

Where the pressure is the external force. Combining Equation 3.19 and 3.20, and dividing over the water density, results in:

$$\frac{\rho_b}{\rho_w}h\eta_{tt} + \frac{EI}{B\rho_w}\Delta^2\eta + \phi_t + g\eta = 0 \tag{3.21}$$

Finally, the damping terms for the kinematic boundary condition in the damping zone are given as follows:

$$\eta_t - \nabla\phi + \mu_1\eta + \frac{\mu_2}{g}\phi = 0 \tag{3.22}$$

The dynamic boundary condition of the damping zone is the same as on the rest of the free surface.

The test function w needs a stabilisation term α in order to be coercive. Therefore, the weak formulation is constructed as either $\frac{1}{2}(w\alpha_b + v)$ or $\frac{1}{2}(w\alpha_f + v)$, for the beam terms or the fluid terms,

respectively. To fit the equations into the Newmark-beta time integration, they are written in the weak formulation and grouped by their derivatives. This gives the following set of equations. The terms containing second derivatives, representing the mass matrix:

$$m((\phi_{tt},\eta_{tt}),(v,w)) = \frac{1}{2}\left(\frac{\rho_b}{\rho_w}\alpha_b w + v, \eta_{tt}\right)_{\Gamma_b} \tag{3.23}$$

The terms containing the first derivative, representing the damping matrix:

$$\begin{aligned} c((\phi_t,\eta_t),(v,w)) =& \frac{1}{2}\left(\alpha_f w + v, \phi_t\right)_{\Gamma_{fs}} - (w,\eta_t)_{\Gamma_{fs}} \\ &+\frac{1}{2}\left(\alpha_b w + v, \phi_t\right)_{\Gamma_b} - (w,\eta_t)_{\Gamma_b} \end{aligned} \tag{3.24}$$

The terms containing no derivatives:

$$\begin{aligned} a((\phi,\eta),(v,w)) =& (\nabla\phi,\nabla w)_\Omega \\ &+\frac{1}{2}\left(\alpha_f w + v, g\eta\right)_{\Gamma_{fs}} \\ &-(\mu_1\eta, w)_{\Gamma_{dz}} - \left(\frac{\mu_2}{g}\phi, w\right)_{\Gamma_{dz}} \\ &+\frac{1}{2}\left(\frac{EI}{B\rho_w}\alpha_b \Delta w + \Delta v, \Delta\eta\right)_{\Gamma_b} + \frac{1}{2}\left(\alpha_b w + v, g\eta\right)_{\Gamma_b} \\ &+s\left((\phi,\eta),(v,w)\right) \end{aligned} \tag{3.25}$$

Where $s\left((\phi,\eta),(v,w)\right)$ is a function containing several stabilisation terms (α_f, α_b and γ_h) (Colomés et al., 2021):

$$\begin{aligned} s\left((\phi,\eta),(v,w)\right) =& -\frac{1}{2}\frac{EI}{B\rho_w}\left[\left(\{\Delta\eta\}, n_\Lambda\cdot(\alpha_b\nabla w + \nabla v)\right]\right)_{\Lambda_b} + \left([\mathbf{n}_\Lambda\cdot\nabla\eta],\{\Delta v\}\right)_{\Lambda_b}\right] \\ &+\frac{1}{2}\frac{EI}{B\rho_w}\left[\frac{\gamma_h}{h}\left([\mathbf{n}_\Lambda\cdot\nabla\eta],[\mathbf{n}_\Lambda\cdot\nabla v]\right)_{\Lambda_b} + \frac{\gamma_h}{h}\left([\mathbf{n}_\Lambda\cdot\nabla\phi],[\mathbf{n}_\Lambda\cdot\alpha_b\nabla w]\right)_{\Lambda_b}\right] \end{aligned}$$

Where the stabilisation terms are defined as:

$$\begin{aligned} \alpha_f &= \frac{\frac{\delta u_t}{\delta u}}{\alpha_h g + \frac{\delta u_t}{\delta u}} \\ \alpha_b &= \frac{\frac{\delta u_t}{\delta u}}{\alpha_h\left(\frac{\rho_b h}{\rho_w}\frac{\delta u_{tt}}{\delta u} + g\right) + \frac{\delta u_t}{\delta u}} \\ \gamma_h &= 100r(r+1) \end{aligned} \tag{3.26}$$

With $r = 2$ being the order of the system and:

$$\begin{aligned} \alpha_h &= \tfrac{1}{2} \quad \text{(default value)} \\ \frac{\delta u_t}{\delta u} &= \frac{\gamma}{\beta\Delta t} \\ \frac{\delta u_{tt}}{\delta u} &= \frac{1}{\beta\Delta t^2} \end{aligned} \tag{3.27}$$

Where Λ_b denotes the edge of the internal nodes of the structure. They are not part of the standard weak formulation, but are added to ensure a coercive system. For the specific set of PDEs, there does not exist a norm that satisfies $B(u,u) \geq ||u||$. Currently, Colomés et al. (2021) are doing research to find a norm which satisfies this inequality. If it can be proved that this norm exists, the monolithic system is unconditionally stable. However, until then, the stabilisation parameters are required to ensure a stable system, which could lead to numerical errors.

Finally, there is a function that contains the external forces, which is the incident vertical velocity profile, that imposes the Airy waves:

$$b(t,(v,w)) = (v_L(t), w)_{\Gamma_L} \tag{3.28}$$

Note that $b(t,(v,w))$ is a transient function of the linear form (the test functions only), whereas the other functions were of the bilinear form (dependent on both the unknowns as well as the test functions). $v_L(t)$ is the spatial derivative in the horizontal direction of Equation 2.4. The numerator has been rewritten as the coordinate system of the numerical model is such that z = 0 at the bed and z = d at the free surface.

$$v_L(\vec{x},t) = \omega\xi_i \frac{\cosh k_i z}{\sinh k_i d} \cos k_i x - \omega t \tag{3.29}$$

With $\vec{x}$ being the 2D spatial vector:

$$\vec{x} = \begin{bmatrix} x \\ z \end{bmatrix} \tag{3.30}$$

The Julia model contains several parameters that need to be calibrated before the tests can be run. These parameters include: the grid resolution, the damping factor, length of the damping zone and the steady state domain. Each of the parameters will be evaluated independently and are calibrated to find an optimum between computational time and accuracy. In Figure 3.3, a representation of the 2D model is given to scale.

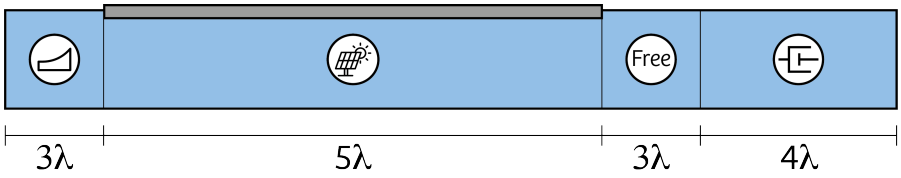

Figure 3.3: Two-dimensional representation of the Julia model. The left-hand side shows the building zone where the waves are generated, followed by the structural zone where the structure is located. Subsequently, there is a free zone without any boundary conditions and finally a damping zone where the wave energy is dissipated.

3.6. Energy calculation

To compare the total amount of energy in the numerical model with the analytical solution, the trial functions are specified as: $w = \phi_t$ and $v = 2\eta_t - \alpha_{f,b}\phi_t$. (Colomés et al., 2021) Where $\alpha_{f,b}$ is the stabilisation parameter for either the fluid or the structure. By inserting them in the weak formulation, the following energy terms are found:

$$E_{k,f} = \frac{1}{2}\rho_w \sum \int \nabla(\phi)^2 d\Omega \tag{3.31}$$

$$E_{p,f} = \frac{1}{2}\rho_w g \sum \int \eta^2 d\Gamma_{fs} \tag{3.32}$$

$$E_{k,b} = \frac{1}{2}\rho_w \sum \int \nabla(\phi)^2 d\Omega + \frac{1}{2}\rho_b h \sum \int \eta_t^2 d\Gamma_b \tag{3.33}$$

$$E_{p,b} = \frac{1}{2}\rho_w g \sum \int \eta^2 d\Gamma_b + \frac{1}{2}\frac{EI}{B} \sum \int \Delta(\eta)^2 d\Gamma_b \tag{3.34}$$

Where $E_{k,f}$ and $E_{p,f}$ are the kinetic and potential energy of the fluid and $E_{k,b}$ and $E_{p,b}$ are the kinetic and potential energy of the structure, respectively.

3.7. Set-up model

Now all the numerical tools are available, it is time to set up the model. An overview of the code is given in Appendix B. The next chapter will discuss the choices which have made during the set-up.

4

Model set-up

As the general mathematics behind the model has been laid out in the previous chapter, this chapter will show how the 2D Julia model is set up. First, a model is tested where the free surface only consists of a fluid. This is done to see if Airy waves can be generated accordingly. Secondly, the energy balance of both the fluid as well as the VFFS are examined independently. The energy balance of the numerical model is compared to the analytical solution. Once the model is set up and the tests have been executed, the fluid structure interaction experiments can be built and run which is further explained in the next chapter.

4.1. Model parameters

The numerical model is set up by using the parameters as given in the experiments by Schreier and Jacobi (2020b). Below Table 4.1 and 4.2 show the parameters of the neoprene rubber material and the incident waves of the experiments, respectively.

Material parameters	**Symbol**	**Value**	**Unit**
Length	L	4.95	m
Width	B	1.02	m
Thickness	h	0.005	m
Density of structure	ρ_b	116	kg/m^3
Flexural rigidity	D	6.9e-3	Nm
Poisson's ratio	ν	0.4	-
Young's modulus	E	560	kPa
Characteristic length	λ_c	0.17	m

Table 4.1: List of material parameters, retrieved from Schreier's experiment (Schreier and Jacobi, 2020b)

Wave parameters	**Symbol**	**Experiment** 1 ($H_{d,1}$)	**Experiment** 2 ($H_{d,2}$)	**Unit**
Wavelength	$\lambda_1 \vee \lambda_2$	0.495	0.990	m
Amplitude	$\xi_1 \vee \xi_2$	0.01	0.02	m
Wave period	$T_1 \vee T_2$	0.563	0.796	s
Water depth	d	1.0	1.0	m
Wave steepness	$\frac{2\xi}{\lambda}$	$\frac{1}{25}$	$\frac{1}{25}$	-
Dispersion parameter	n	0.500	0.500	-

Table 4.2: Wave parameters retrieved from Schreier's experiment (Schreier and Jacobi, 2020b)

4.2. Verification

To verify if the numerical model produces the correct output values based on the input parameters, the results are compared to the analytical solution. This is subdivided into different regions. The free surface waves are compared to the analytical Airy waves. The wavelength, amplitude and frequency of the waves should correspond to expected analytical input value.

Moreover, the amount of wave energy is calculated for both the free surface waves as well as the hydroelastic waves. These are compared to the potential and kinetic energy components which were derived from the (altered) Cauchy-Poisson condition.

Finally, the numerical damping zone is calibrated to ensure that all radiating energy is dissipated before it reaches the end of the domain. This iteratively done and the energy levels should converge to zero. A complete overview of all the chosen model settings is given in Table 4.12 at the end of the this chapter.

4.2.1. Grid resolution

The grid resolution or mesh size is the amount of cells the model consists of. The grid resolution should be chosen accordingly based on the phenomena one wants to examine. If the grid resolution is too large, the results may contain errors, or certain phenomena will not be visible due to the lack of resolution. If the mesh size is too small, the model becomes computationally expensive and will slow it down. Also, if the model is explicit in time, a too small grid resolution could result in errors when trying to solve the system. This will not happen for the Julia model, however, as the Newmark-beta method is used, which is implicit in time and thus unconditionally stable.

As the model needs to be solved in space and time, the time step is inevitably connected to the grid resolution. For these simulations, the CFL-condition is used to determine the time step as described in the previous chapter. By choosing a Courant number equal to one (C = 1) and given the phase velocity ($c = \frac{\lambda}{T}$), Equation 3.15 becomes:

$$\Delta t \leq \Delta x \cdot \frac{T}{\lambda} \tag{4.1}$$

To prevent interpolation errors (see Figure 4.1), Δx is dependent on the wavelength. From here it follows that Δt is subsequently dependent on the wave period:

$$\Delta t \leq \frac{\lambda}{n_{cells}} \cdot \frac{T}{\lambda} = \frac{T}{n_{cells}} \tag{4.2}$$

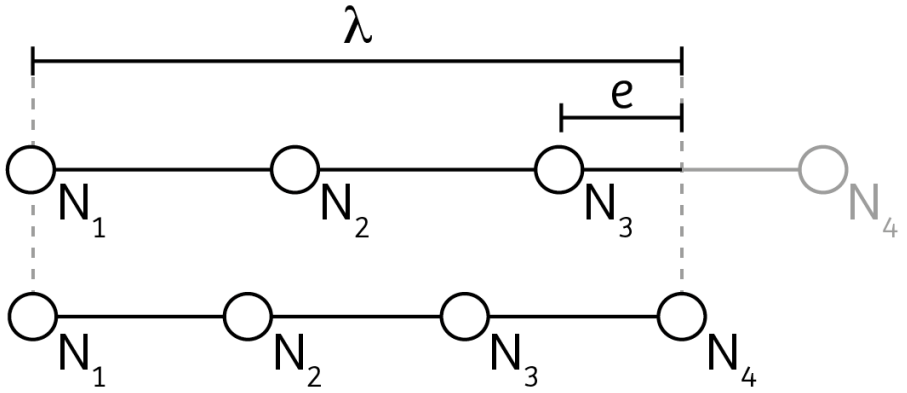

Figure 4.1: If the wavelength (λ) is misaligned with the grid size, an interpolation error is developed. As one is only able to retrieve results from the nodes, it is convenient to choose a spatial resolution that complies with the length of the wave.

The resolution of the Julia model is chosen based on the wavelength of the governing wave conditions. According to The SWASH team (2020), a rule of thumb is to have at least 50 grid cells per wavelength. However, in a similar paper, Akkerman et al. (2020) finds a convergence of energy already at 24 cells

per wavelength. The resolution of the grid can be divided into two parameters; the horizontal component and the vertical component. For the horizontal component the resolution must be high, as the incident waves travel across the domain and each location is equally important. For the vertical component, however, the interest lies mainly at the free surface. Therefore, it is acceptable to have larger cells at bottom of the model than at the free surface.

Horizontal mesh size

To check if the mesh size is accurate, the 2D FEM model is altered by removing the structure, and looking only at the incident waves. A vertical velocity profile is imposed on the left boundary which causes free surface waves to develop. These waves should be equal to the expected wavelength and constant across the domain. By calculating the error, an optimal mesh size is retrieved. Figure 4.2 shows the wavelength of the incident waves over the domain of the model. A zero crossing method has been used to calculate wavelength at each location. Therefore, the starting point in the graph is not at X = 0, but half a wavelength ahead ($X = \frac{\lambda}{2}$). The end of the calculation is at half a wavelength before the damping zone starts. Otherwise, the damping zone is interfering. Three different horizontal mesh sizes have been evaluated; $n_{cells,x} = 20$, $n_{cells,x} = 50$, $n_{cells,x} = 100$ per wavelength. The wavelength is normalised and plotted as the blue line. The black dashed line indicates the supposed incident wavelength. The dashed red and green lines indicate where the VFFS is supposed to be laid in the numerical model. However, during the set-up of the free surface waves of the model, no structure is implemented yet. Figure 4.2 shows that for all three resolutions, the wavelength varies between higher and lower values than the theoretical wavelength. The errors of each resolution are summarised in Table 4.3.

Resolution	Error [%]		
$n_{cells,x}$	Mean	Upper bound	Lower bound
20	-1.59	+0.15	-0.22
50	-0.22	+0.05	-0.03
100	-0.03	+0.04	-0.04

Table 4.3: Overview of wavelength error of long waves for each horizontal mesh size.

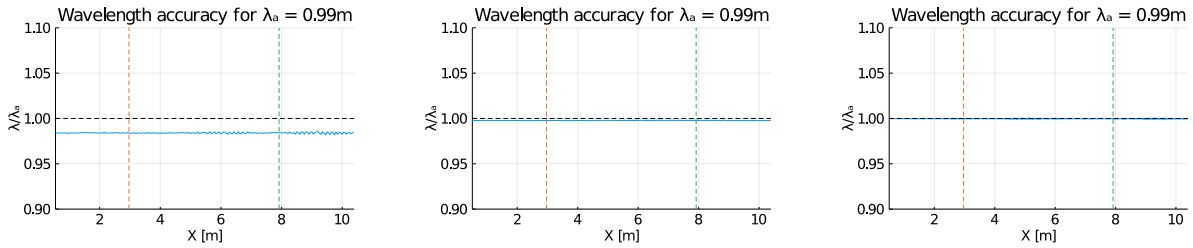

Figure 4.2: Calculation of normalised wavelength of long waves for $n_{cells,x}$ = 20 (left), $n_{cells,x}$ = 50 (middle) and $n_{cells,x}$ = 100 (right) to determine the mean and the error. (– Wavelength; - - BeginVFFS; - - End VFFS; - - Original wavelength)

In Figure 4.3, the wavelength for the short waves has been visualised and its errors are summarised in Table 4.4.

Resolution	Error [%]		
$n_{cells,x}$	Mean	Upper bound	Lower bound
20	-1.27	+0.16	-0.20
50	+0.09	+0.09	-0.11
100	+0.29	+0.06	-0.06

Table 4.4: Overview of wavelength error of short waves for each horizontal mesh size.

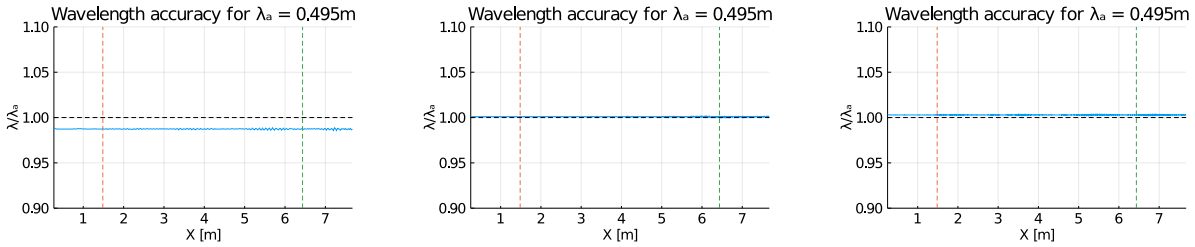

Figure 4.3: Calculation of normalised wavelength of short waves for $n_{cells,x}$ = 20 (left), $n_{cells,x}$ = 50 (middle) and $n_{cells,x}$ = 100 (right) to determine the mean and the error. (– Wavelength; - - BeginVFFS; - - End VFFS; - - Original wavelength)

For the long waves, there is an improved accuracy as the resolution increases. However, for the short waves an optimum is found at 50 cells per wavelength. As for both waves, the mean difference to the theoretical value and the errors are very small (-0.22%), it is chosen to use 50 cells per wavelength in the X-direction.

Vertical mesh size

For the vertical mesh size, an unequally spaced grid is used. As explained above, the potential energy in the top of the model is much more important than at the bottom. Therefore, the following formula has been used to create an exponentially spaced grid, as this could potentially save some significant computational time.

$$\begin{aligned} z_i &= d - \frac{d}{2^i} \quad \text{for} \quad i < n_{cells,z} \\ z_i &= d \quad \text{for} \quad i = n_{cells,z} \end{aligned} \tag{4.3}$$

Where z_i is the i^{th} vertical node. This formula applies to all vertical nodes, except the last one, which is always equal to the water depth. This unequally spaced grid is compared with a uniform spaced grid of $n_{cells,z}$ = 10 is used. Figure 4.4 shows the uniform spaced vertical grid cells for the long waves (left) and the short waves (right). The errors are summarised in Table 4.5

Resolution	Error [%]		
$n_{cells,z}$	Mean	Upper bound	Lower bound
10 (long)	+0.25	+0.04	-0.08
10 (short)	+0.11	+0.05	-0.07

Table 4.5: Overview of wavelength error of long waves and short waves for a uniform spaced vertical grid.

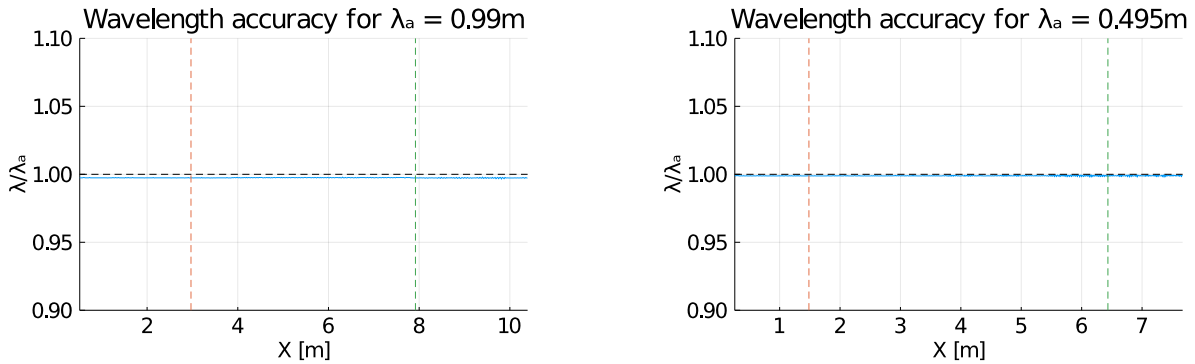

Figure 4.4: Calculation of normalised wavelength of long waves (left) and short waves (right) for uniform spaced grids. (– Wavelength; - - BeginVFFS; - - End VFFS; - - Original wavelength)

The uniform spaced grid is the benchmark to compare the exponentially spaced grid to. In Figure 4.5, the wavelength is given for four different test runs; $n_{cells,z}$ = 3, 4, 5 and 6. It is observed that as the amount of cells increases, the mean value decreases and the errors increase. This could be due to numerical noise. The errors are summarised in Table 4.6.

Resolution	Error [%]		
$n_{cells,z}$	Mean	Upper bound	Lower bound
3	+0.10	+0.06	-0.03
4	-0.22	+0.05	-0.03
5	-0.24	+0.13	-0.13
6	-0.24	+0.27	-0.33

Table 4.6: Overview of wavelength error for long waves for an uneven spaced vertical grid.

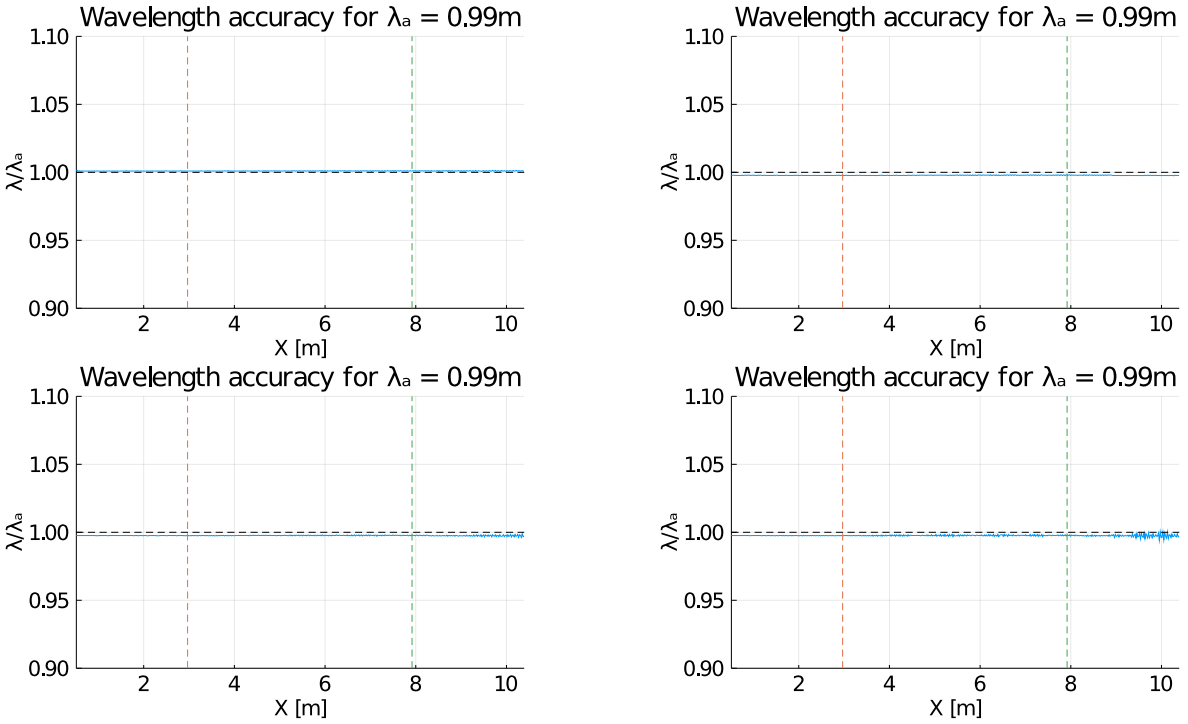

Figure 4.5: Calculation of normalised wavelength of long waves for $n_{cells,z}$ = 3 (top left), $n_{cells,z}$ = 4 (top right), $n_{cells,z}$ = 5 (bottom left) and $n_{cells,z}$ = 6 (bottom right). (– Wavelength; - - BeginVFFS; - - End VFFS; - - Original wavelength)

For the short waves, the unequally spaced grid calculations have also been made and visualised in Figure 4.6. Where for the long waves the fewest amount of vertical grid cells ($n_{cells,z}$ = 3) showed the best solution, for the short waves the mean wavelength differs +2.9%. The errors are summarised in Table 4.7

Resolution	Error [%]		
$n_{cells,z}$	Mean	Upper bound	Lower bound
3	+2.9	+0.15	-0.09
4	+0.09	+0.09	-0.11
5	-0.22	+0.16	-0.12
6	-0.35	+0.30	-0.35

Table 4.7: Overview of wavelength error for short waves for an uneven spaced vertical grid.

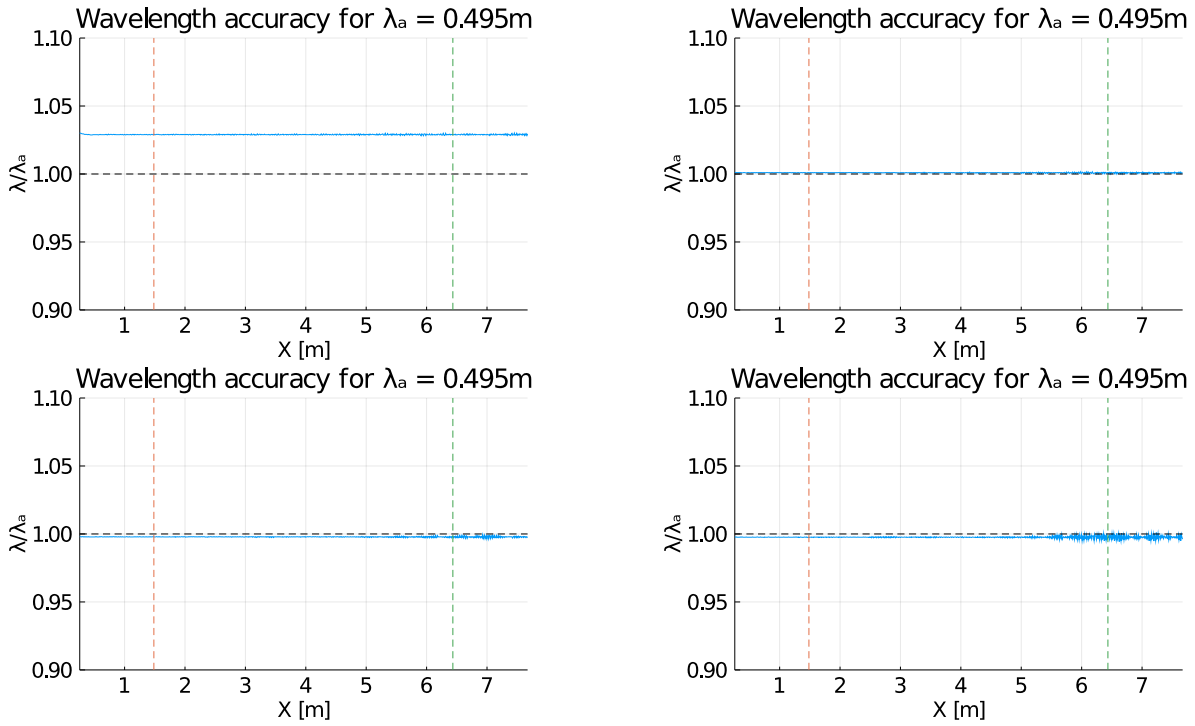

Figure 4.6: Calculation of normalised wavelength of short waves for $n_{cells,z}$ = 3 (top left), $n_{cells,z}$ = 4 (top right), $n_{cells,z}$ = 5 (bottom left) and $n_{cells,z}$ = 6 (bottom right). (– Wavelength; - - BeginVFFS; - - End VFFS; - - Original wavelength)

Comparing the values of the exponentially spaced grid to the benchmark, it becomes clear that for the long waves, test runs perform better if only three or four vertical grid cells are used. For the short waves this only accounts for four grid cells over the vertical domain. It is also observed that for a too fine resolution, the accuracy of the results decrease again. It is likely that this is caused by numerical noise as is observed in the lower right plot of Figure 4.5 and 4.6, where at the end of the domain the wavelength is not constant anymore. Therefore, it is decided to use the exponentially spaced grid with $n_{cells,z}$ = 4.
In Table 4.8 an overview is given of the effect that Equation 4.3 has on the spacing of the vertical cells. In the table, the Z-coordinates are given for unequally spaced vertical nodes for $n_{cells,z}$ = 4, $n_{cells,z}$ = 5 and $n_{cells,z}$ = 6 with a water depth of H = 1m as used in the model. Comparing to a uniform spaced grid of $n_{cells,z}$ = 10 (spacing is 0.1m), one observes that four unequally spaced cells result in a coarser grid (spacing is 0.125m), whereas five cells give a finer grid (spacing is 0.0625m) just below the free surface.

	Z-coordinate [m]				**Spacing [m]**
Nodes / Cells	**3**	**4**	**5**	**6**	
1	0.0	0.0	0.0	0.0	-
2	0.5	0.5	0.5	0.5	0.5
3	0.75	0.75	0.75	0.75	0.25
4	1	0.875	0.875	0.875	0.125
5	-	1	0.9375	0.9375	0.0625
6	-	-	1	0.96875	0.03125
7	-	-	-	1	0.03125

Table 4.8: Z-coordinates of unequally spaced grid for several amount of vertical grid resolutions.

The second criterion states that the amplitude of the wave should remain constant. To check this, Figure 4.7 shows the free surface elevation of the model with the proposed mesh sizes: $n_{cells,x}$ = 50 and $n_{cells,z}$ = 4.

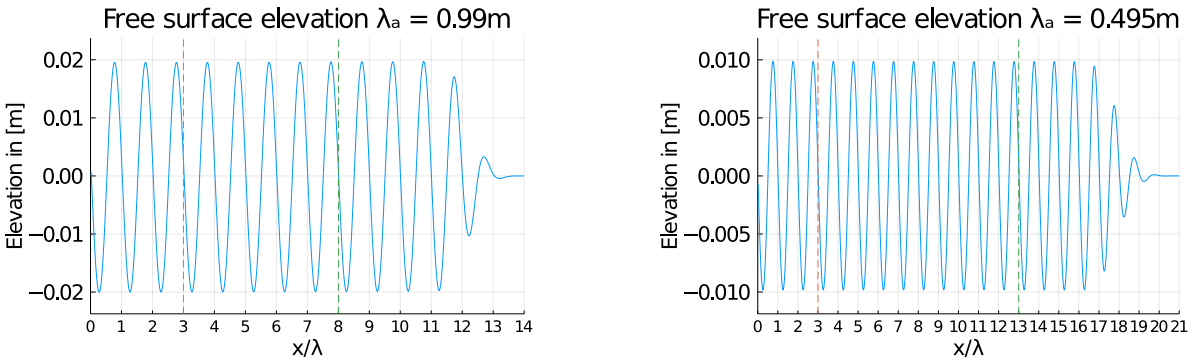

Figure 4.7: (Free surface elevation of long waves (left) and short waves (right). (– Free surface elevation; - - BeginVFFS; - - End VFFS)

For the long waves, the mean amplitude of the waves, before they enter the damping zone, is -0.99% lower than the theoretical amplitude of ξ = 0.02m with errors ranging (-0.28% to +0.53%). For the short waves, the differences are even lower, giving a mean amplitude difference of -0.52% compared to ξ = 0.01m with errors ranging (-0.13% to +0.13%). The errors on the amplitudes confirm the choice of the proposed mesh sizes and therefore, it is decided to proceed with these values.

4.2.2. Damping factor

The damping factor (μ_0) is a value that determines the amount of damping in the damping zone. According to Kim et al. (2014), this factor needs to be chosen iteratively. In their paper, they use a μ_0 equal to 2.5. However, their wave parameters are completely different than the ones used in this report. Therefore, a range of values will be examined to see how this damping factor behaves. Values of μ_0 = 5, 10 and 20 are evaluated to see which fits best to the model. Figure 4.8 shows the free surface elevation of the damping zone in case of the long incident waves. To see if the damping works accordingly, the final value of the free surface is compared to the initial amplitude. The left plot shows the free surface elevation with a damping factor of μ_0 = 5 and the elevation at the end of the domain is still 0.97% of the initial amplitude. If the damping factor is increased to μ_0 = 10, this value decreases to 0.011%. An even larger damping factor of μ_0 = 20 gives an amplitude decrease of the same order as the previous value, resulting in an elevation of only 0.008% of the initial amplitude. Based on these results, the damping factor of μ_0 = 5 is clearly too low, as there is still energy to dissipate. On the other hand, the Figure 4.8 also shows that a damping factor of μ_0 = 20 damps the waves faster than necessary. This could cause wave reflection and is therefore not desirable.

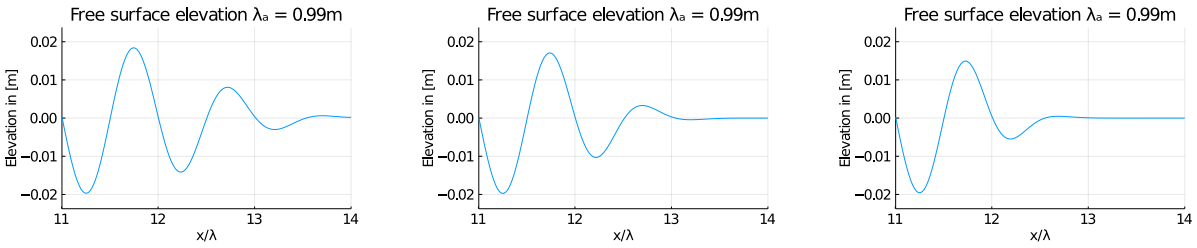

Figure 4.8: Three plots with different damping factors ($\mu_0 = 5$ (left), $\mu_0 = 10$ (middle) and $\mu_0 = 20$ (right)) for short waves. (– Free surface elevation)

The results of different damping zone length for the short waves are visualised in Figure 4.9. The lowest damping factor μ_0 = 5 gives a final elevation of 1.25%, indicating that not all energy is fully dissipated. A damping factor of μ_0 = 10 results in an elevation of 0.083% at the end of the domain. The highest damping factor μ_0 = 20 gives the best results in terms of damping with a final value of 0.016%. However, this is at cost of potential wave reflection, as the numerical viscous zone becomes stronger early in the damping zone.

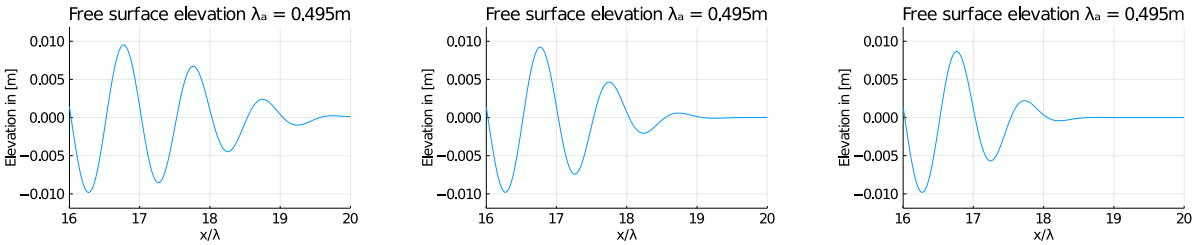

Figure 4.9: Three plots with different damping factors ($\mu_0 = 5$ (left), $\mu_0 = 10$ (middle) and $\mu_0 = 20$ (right)) for short waves. (– Free surface elevation)

Taking into account that as much energy should be dissipated with a minimal risk on wave reflection, it is chosen to use μ_0 = 10 as the damping factor value.

4.2.3. Damping zone

The damping zone needs to be sufficient long in order to damp the wave energy correctly. Min Woo Kim suggests to use a damping zone of at 1.5 times the wavelength. The initial value will be set to the wavelength of the incident waves. In Figure 4.10, three test runs are visualised that have a damping zone length of $Ld = 2\lambda$, 3λ and 4λ. To see which damping zone length fits best, it is examined how much the amplitude is decreased at the final node of the domain. Also, it is taken into account if a larger damping zone has a significant effect on the decrease in amplitude.

For the shortest damping zone length (2λ), the amplitude is decreased to 0.434% of the incident amplitude. If the damping zone is elongated to 3λ, this decreases even further to 0.011%. Once the damping zone is stretched even more to 4λ, there is a slight increase in amplitude compared to the previous length; 0.018%. Taken these values into account, it is decided to use a damping zone length of 3λ for the model concerning the long waves.

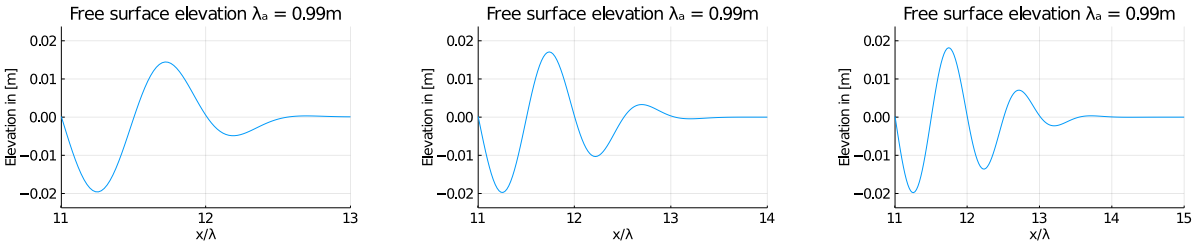

Figure 4.10: Three plots with different damping zone lengths for long waves . A damping length of $Ld = 2\lambda$ does not fully damp the wave (left). A damping zone length of 3λ gives the best results (middle). The damping zone length of 4λ gives worse results and requires unnecessary computational time (right). (– Free surface elevation)

The same procedure has been repeated for the test runs with short waves and visualised in Figure 4.11. A damping zone length of 2λ shows a decrease to 2.09% compared to the incident amplitude. For the 3λ test run, the final value is equal to 0.389% and for the largest damping zone length (4λ), the amplitude decreases to even 0.083%. Therefore, it is decided that the test runs with the short waves are run with a damping zone length of 4λ.

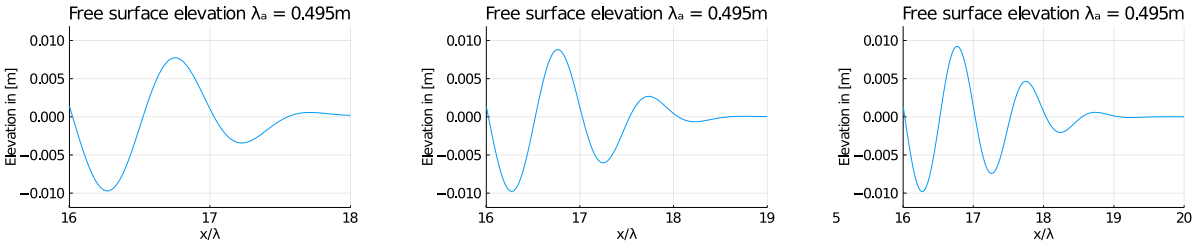

Figure 4.11: Three plots with different damping zone lengths for short waves . A damping length of $Ld = 2\lambda$ does not fully damp the wave (left). A damping zone length of 3λ gives better results (middle). The damping zone length of 4λ gives the best results (right). (– Free surface elevation)

4.2.4. Steady-state domain

In order to get reliable results, the model should be in a steady-state. This means that the behaviour in the model is constant or periodic in both space and time. To determine the steady-state, the wavelength of the waves should be constant across the domain (except the damping zone). In Figure 4.12, the wavelength of the long waves (left) and short waves (right) have been calculated for different moments in time. After 50 wave periods, the normalised mean wavelength is -0.28% lower than than the theoretical wavelength and there are still high fluctuations. The error of the normalised mean wavelength drops as time progresses and the fluctuation errors stagnate after 100 wave periods.

The short waves show an error of the normalised mean wavelength of +0.09% after 50 wave periods. The mean error does not decrease anymore as time progresses. The fluctuations, however, keep decreasing until 90 wave periods. An overview of the errors is given in Table 4.9. Therefore, it is chosen to run both models for at least 100 wave periods.

Wave periods	Error [%]		
T [s]	Mean	Upper bound	Lower bound
50 (long)	-0.28	+0.27	-0.28
50 (short)	+0.09	+0.57	-0.63
100 (long)	-0.22	+0.05	-0.03
90 (short)	+0.09	+0.09	-0.11

Table 4.9: Overview of wavelength errors at given timestamps.

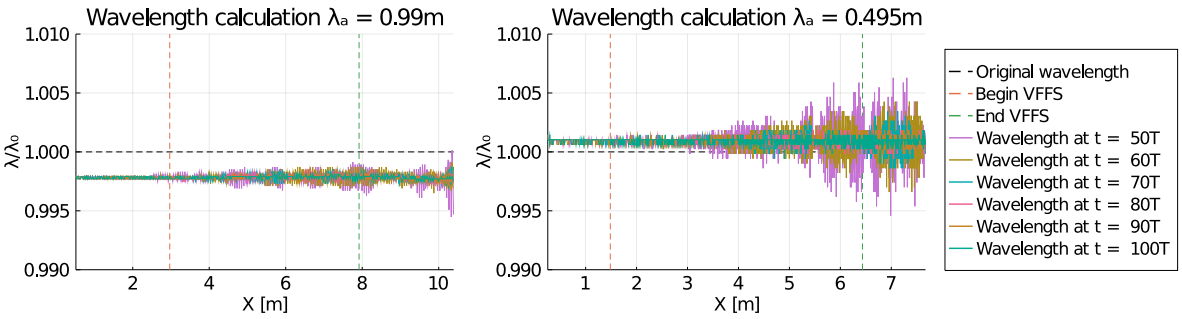

Figure 4.12: Wavelength calculation for different points in time for the long waves (left) and short waves (right). As time progresses the fluctuations significantly drop and stagnate at t = 100T; for the short waves this happens at t = 90T. Note that although the wavelength calculations seem not to align with the original wavelength, the y-axis is highly zoomed.

4.2.5. Energy calculation

Finally, as the model is set up, the total amount of energy is calculated to see if this corresponds to the theory. This is done for both a scenario where there is only water, as well as an infinite VFFS. This time, the setup of the model is only one wavelength long and the boundaries (Γ_L and Γ_R) are periodic. This means that the length of the model becomes infinitely long. An initial displacement of the free surface is imposed and no energy is added to the system during the time span. As there is also no damping, it is expected that the wave keeps traveling without any dissipation of energy. Using Equations 2.30, 2.33, 2.35, 2.36, 2.38 and 2.39 of the previous chapter, the total energy in the incident waves and the VFFS are calculated independently. These values are compared to the numerical energy calculation as given by Equation 3.31, 3.32, 3.33 and 3.34.

Fluid only

In the case of only having a fluid domain, the amount of energy in the system should be equal to the sum of the potential energy and the kinetic energy. Figure 4.13 shows the amount of energy in the system for the short waves and the long waves for one wave period. It is observed that the total amount of energy remains constant over time, whereas the potential energy and kinetic energy component slightly vary in time. Table 4.10 shows the theoretical value as well as the numerical value of the energy components.

It is observed that the differences between the analytical approach are almost identical to the numerical results (+0.08%).

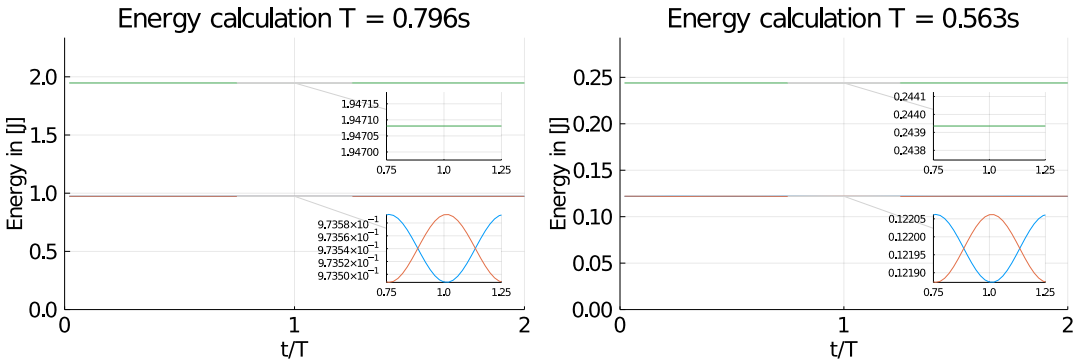

Figure 4.13: Energy components for long waves (left) and short waves (right). (– Potential energy; – Kinetic energy; – Total energy)

Energy [J/m]	Theoretical Short	Numerical Short	Difference	Theoretical Long	Numerical Long	Difference
$E_{k,f}$	0.1219	0.1220	+0.0769%	0.9735	0.9735	+0.0053%
$E_{p,f}$	0.1219	0.1220	+0.0770%	0.9735	0.9735	+0.0054%
E_t	0.2437	0.2439	+0.0770%	1.9470	1.9471	+0.0053%

Table 4.10: Overview of energy components. Numerical values compared to analytical values.

Beam only

The amount of energy in the system for the beam is also calculated and is visualised in Figure 4.14 and the differences between the analytical method and the numerical calculation are given in Table 4.11. Here the differences are slightly larger, reaching a maximum error of 0.8%. Note that the total energy in Figure 4.14 slightly differs compared to Figure 4.13. Due to the density of the beam and wave deformation the amount of energy in the system does not correspond with the free surface wave.

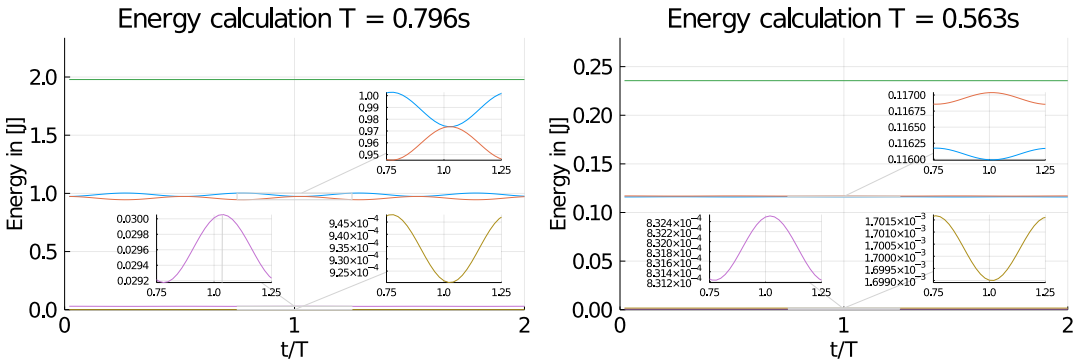

Figure 4.14: Energy components for long waves (left) and short waves (right). (– Potential energy; – Kinetic energy; – Total energy; – Kinetic beam energy; – Potential beam energy)

Energy [J/m]	Theoretical Short	Numerical Short	Difference	Theoretical Long	Numerical Long	Difference
$E_{k,f}$	0.1160	0.1169	+0.8175%	0.9735	0.9722	-0.1274%
$E_{p,f}$	0.1160	0.1161	+0.0718%	0.9735	0.9748	+0.1376%
$E_{k,b}$	0.0008	0.0008	-0.1805%	0.0035	0.0035	-0.5084%
$E_{p,b}$	0.0017	0.0017	+0.2036%	0.0009	0.0009	+0.2695%
E_t	0.2345	0.2356	+0.4407%	1.9514	1.9515	+0.0043%

Table 4.11: Overview of wave energy differences between the numerical output values and the analytical method.

4.2.6. Conservation of energy

To show that the numerical model is energy conservative, the total amount of energy in the system is measured. This is done for two different cases. First, the energy level in the system for the free surface without a structure is shown. Figure 4.15 shows the evolution of energy for 100 wave periods. The green line confirms that the total energy in the system is conserved, as after 30 wave periods it becomes a constant line. It is observed that the potential and kinetic energy component are precisely $\frac{\pi}{2}$ out of phase, as was expected for regular waves. Furthermore, the kinetic energy component varies less than the potential energy component. It is likely that this is caused by the damping zone where the energy is dissipated. Finally, the total amount of energy in the system also varies over time. This is caused by the fact that the incident wave energy is not in phase with the dissipated energy.

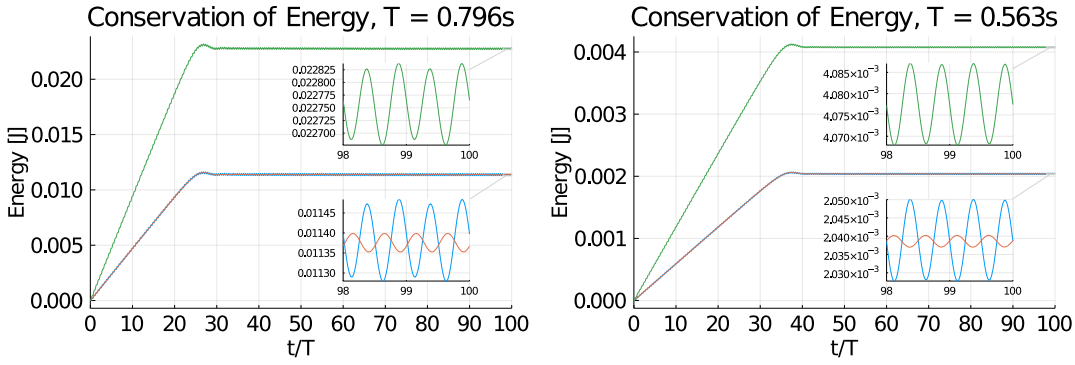

Figure 4.15: Evolution of energy components in time for long waves (left) and short waves (right). (– Potential energy; – Kinetic energy; – Total energy)

Secondly, the total energy of the fluid structure interaction is calculated. Figure 4.16 shows the amount of energy in the entire domain split over four energy components. The total energy in the system, indicated by the green line, is clearly conserved. For the fluid energy components similar behaviour is observed compared to the case without a floating structure. Furthermore, it is observed that for the short waves, the potential energy of the structure is higher than the kinetic part and for the long waves, this is vice versa. The hydroelastic wave deformation is greater than one for the short waves ($K > 1$) and lower than one for the long waves ($K < 1$), which thus have influence on the magnitude of the energy components.

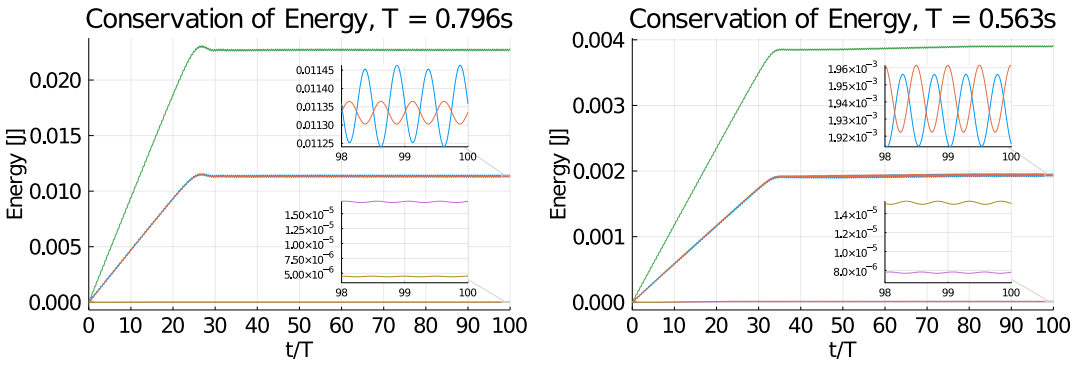

Figure 4.16: Evolution of energy components in time for fluid structure interaction of long waves (left) and short waves (right). (– Potential energy; – Kinetic energy; – Total energy; – Kinetic beam energy; – Potential beam energy)

4.2.7. Wave frequency

The theory states that the incident wave deforms as the wave energy radiates through the structure. However, the frequency of the wave should remain identical. A Fast-Fourier-Transform (FFT) has been executed on the time series at two locations; the incident wave zone and the hydroelastic wave zone. The FFT was used to calculate the spectral density of the system. This is done by taking the square of the real part (a_i) of the FFT solution and dividing it over two times the resolution ($\delta\omega$) of the FFT:

$$E(\omega) = \frac{a_i^2}{2\delta\omega} \tag{4.4}$$

Figure 4.17 shows that the angular frequency across the domain remains constant, which means that only the wavelength disperses. Subsequently, it can be derived that the phase velocity of the wave also changes with the same ratio as the change of wavelength.

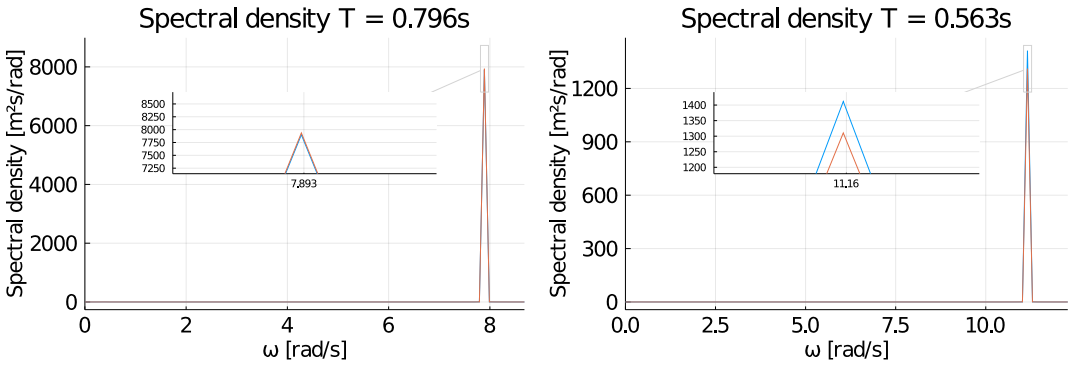

Figure 4.17: Spectral density calculation for incident waves and hydroelastic waves of long waves (left) and short waves (right). (– Incident wave; – Hydroelastic wave)

4.2.8. Energy flux

To compare two locations with each other, an energy flux balance is established. This is the rate of energy that travels through the domain and given by the product of the amount of wave energy and the group velocity of the wave. As was shown in the previous section, the wave frequency was constant across the numerical domain. This implies that the group velocity only changes if the wavelength changes. Figure 4.18 shows the energy flux at two locations in the numerical domain. After 40 wave periods, the red and the blue line clearly converge to the same value, which confirms that the energy flux is equal at both locations. It is observed that the energy flux at $X = \lambda$ rises earlier than the energy flux at $X = 9\lambda$. Also, there is a peak in the total energy flux before it reaches its steady-state. For the short waves, the energy fluxes are nearly identical, whereas, for the long waves, the differences are slightly larger. However, the differences are so small that this could be related to numerical noise. The flux has a sinusoidal shape, which fits with the energy transport of a wave.

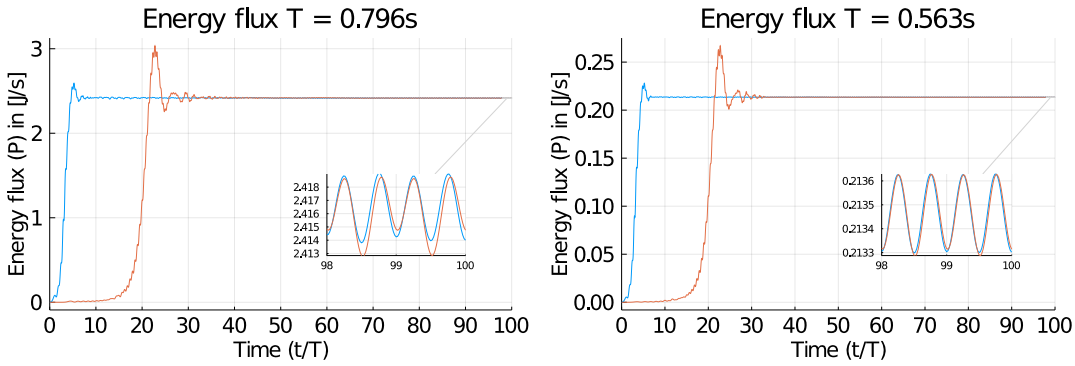

Figure 4.18: Energy flux for incident waves at two locations of long waves (left) and short waves (right). (– Energy flux at $X = \lambda$; – Energy flux at $X = 9\lambda$)

4.2.9. Stabilisation

Currently, as mentioned in the previous chapter, Colomés et al. (2021) are doing research on the stabilisation parameters to find an optimal definition, which will be found in the near future. Until then, the default value for $\alpha_h = 0.5$ will be used to calculate the results.

4.2.10. Summary

The findings of the results from the above mentioned criteria have been summarised in Table 4.12. These parameters will be used in the set-up of the Julia model where the fluid structure interaction is built. In order to obtain accurate results, it was found that the error of the resolution in X-direction converged after 50 cells per wavelength. This is in line with the earlier mentioned rule of thumb proposed by the SWASH team. The resolution in the Z-direction is only four cells per wavelength, but exponentially mapped so that the resolution is high at the free surface and low near the bed. This gave accurate results and speeds up the computation time. The time step has been set to a fraction of the wave period with the highest resolution of the space vector, which is the X-direction. From here the CFL condition equals one, which makes it stable for both explicit models, as well as implicit models. The choice to make it a fraction of the wave period is convenient as the waves can be examined at their zero-crossing. The damping factor of ten and a damping zone of three or four wavelengths, respectively for long or short waves proved to result in dissipating the wave energy most efficiently without having too much wave reflection. Finally, the steady state is well reached at 100 wave periods. An overview of the model set-up is given in Figure 3.3.

Julia parameters	**Symbol**	**Experiment 1 (short waves)**	**Experiment 2 (long waves)**	**Unit**
Grid resolution (x)	$n_{cells,x}$	50	50	-
Grid resolution (z)	$n_{cells,z}$	4	4	-
Cell size	Δx	$\frac{\lambda_1}{n_{cells,x}}$	$\frac{\lambda_2}{n_{cells,x}}$	m
Time step	Δt	$\frac{T_1}{n_{cells,x}}$	$\frac{T_2}{n_{cells,x}}$	t
Damping factor	μ_0	10	10	-
Damping zone	L_d	$4\lambda_1$	$3\lambda_2$	m
Steady-state	T_{ss}	$[100T_1, \infty\rangle$	$[100T_2, \infty\rangle$	s
Stabilisation parameter	α_h	0.5	0.5	-

Table 4.12: Julia model parameters

5

Experiments

This chapter explains the set-up of the test runs for the numerical model. The set-up is divided into three parts. First, a comparison is made with the numerical model and Schreier's experimental research. Secondly, a sensitivity study is executed by comparing the analytical and the numerical model for a range of different scenarios. These scenarios are based on realistic values of the North Sea. This is done using wave climate characteristics of an offshore wind farm in the North Sea. The material parameters are chosen such that they lie within the given boundaries of the theory. Thirdly, the parameters are changed to values where the analytical approach does not hold anymore.

5.1. Schreier's and Jacobi's experiment

Schreier and Jacobi (2020b) made a test set-up in the towing tank of the TU Delft where a 5 mm floating neoprene mat was installed with a $\frac{1}{1000}$ height to length ratio. Regular waves were imposed directed towards the floating structure. As the towing tank is not large enough to accommodate for full-scale testing, the experiment was scaled. Given a significant wave height off the Dutch coast in the North Sea of 1-2 metres (Eecen, 2009), a scaling comparison could be made using Froude Scaling. This would lead to a scale model of $s = 50$. They used a constant wave steepness ratio of $\frac{1}{25}$ throughout the experiments. Translating his values to the real world, corresponding wavelengths of $\lambda = 25$m and $\lambda = 50$m and wave periods of $T = 3.98$s and $T = 5.63$s would occur for the short and long waves, respectively, at a water depth of $d = 50$m. These values seem realistic wave periods of existing sea-states, as DNV gives wave period bounds ranging from $T_{min} = \sqrt{13H_s}$ to $T_{max} = \sqrt{30H_s}$ (DNV-GL, 2016), resulting in values ranging from (3.60s - 5.48s) and (5.09s and 7.75s) for short and long waves, respectively. Using the deep water relation between wavelength and wave period as given in Equation 5.1, DNV's range is rewritten to a wave steepness range of $\frac{1}{20}$ to $\frac{1}{50}$. Their choice of a wave steepness of $\frac{1}{25}$ therefore is moderately steep. In Table 4.1 and Table 4.2 one finds the used material and wave parameters of the experiment. In Table 5.1

$$T = \sqrt{\frac{2\pi\lambda}{g}} \Rightarrow \frac{H_s}{\lambda} = \frac{2\pi H_s}{gT_{min}^2} \approx \frac{1}{20} \vee \frac{2\pi H_s}{gT_{max}^2} \approx \frac{1}{50} \tag{5.1}$$

Test run	$H_{d,1}$ (short waves)		$H_{d,2}$ (long waves)	
	$\frac{EI}{B}$	ρ_b	$\frac{EI}{B}$	ρ_b
1	0.09559	116	0.09559	116

Table 5.1: Overview of Schreier's test runs for numerical model. $\frac{EI}{B}$ in Nm and ρ_b in kg/m^3

They used Digital Image Correlation (DIC) to measure the surface elevation of the entire structure with a spatial planar resolution of 15 mm and a surface height error ranging from 0.7 to 1.8 mm. Wave

buoys were used to measure the wave elevation, which had a error margin of 1.3 mm. They showed that using this technique the test runs were repeatable and that the VFFS followed the local waves elevation for the long waves. In case of the short waves, a hydroelastic interaction was observed that led to wave stretching. Finally, they observed 3D effects across the width of the structure.

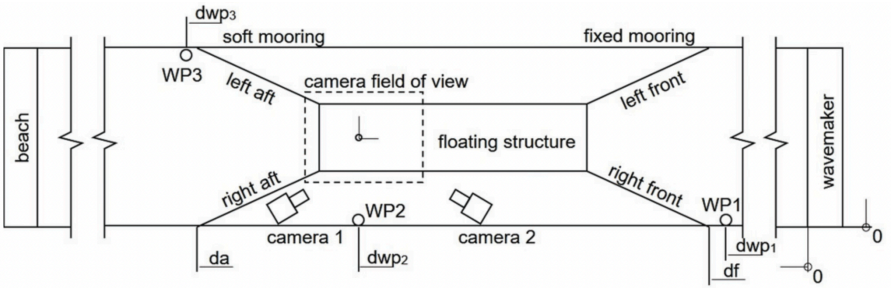

Figure 5.1: Set-up of experimental study. (Schreier and Jacobi, 2020b)

Position (pos)		**1**	**2**	**3**
Wave probe 1	$dwp1[\mathrm{m}]$		25.84	
Wave probe 2	$dwp2[\mathrm{m}]$		29.72	
Wave probe 3	$dwp3[\mathrm{m}]$		38.35	
Front mooring line	$df[\mathrm{m}]$	20.85	22.55	24.25
Aft mooring line	$da[\mathrm{m}]$	35.94	37.64	39.34
Front edge of model	def(pos) [m]	25.77	27.47	29.17
Aft edge of model	dea(pos) [m]	30.72	32.42	34.12

Table 5.2: Longitudinal position (in meters) of wave probes, mooring points, and front and aft model edge with respect to the wave maker flap in its upright position. (Schreier and Jacobi, 2020b)

The results from Schreier and Jacobi (2020b) experiments are displayed in Figure 5.2. For the short waves, the analytical value of wave stretching was calculated to be 40 mm. From the experiment at X = 800mm, a total wavelength stretching of 36 mm was observed at the center line of the VFFS compared to the sides of the VFFS. For the long waves, an expected wave shortening of 15 mm was calculated. The spatial resolution of the camera was about the same size. Therefore, it could not be confirmed whether or not wave shortening actually occured. (Schreier and Jacobi, 2020b)

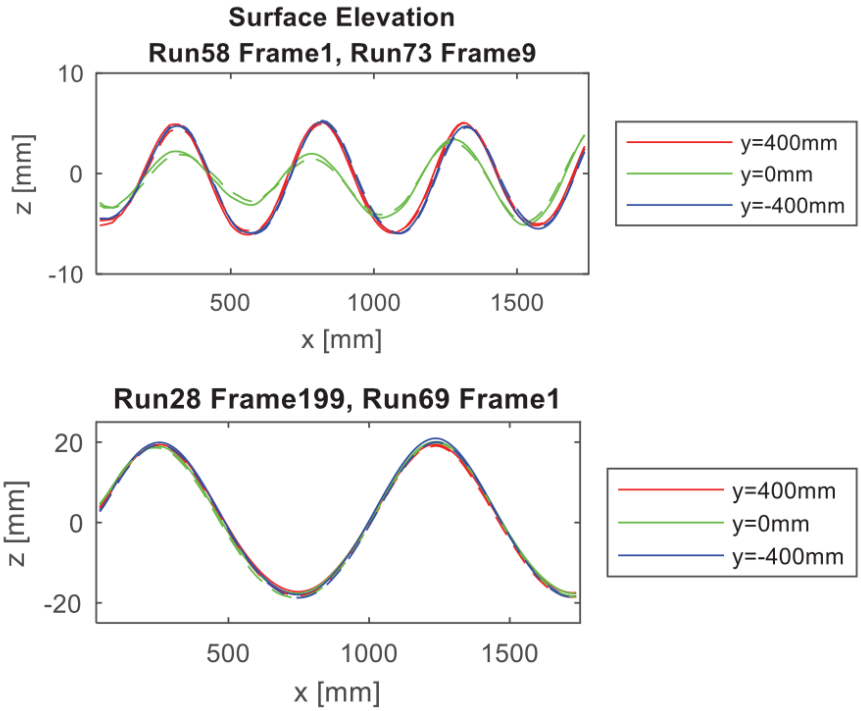

Figure 5.2: Repeatability of surface elevation profiles of phase-matching DIC frames of the aft section of the model for each two test runs with repeated wave condition. Top: runs R58 (continuous lines) and R73 (dashed lines), short waves (Experiment 1); bottom: runs R28 (continuous lines) and R69 (dashed lines), long waves (Experiment 2). Wave propagation right to left. (Schreier and Jacobi, 2020b)

5.2. Sensitivity study

The sensitivity study is executed to examine when the numerical model corresponds with the analytical solution. To do this, wave characteristics are used from an existing offshore wind farm located in the North Sea; the Borssele Wind Farm Zone. The data is obtained from a site study executed by Deltares (Deltares, 2015). In Figure 5.3, monthly wave roses are displayed from a 20 years time period. This location shows a mean wave ($H_{d,m}$) height of 1.3m and a extreme wave height ($H_{d,e}$) of 6.8m. From DNV, it is obtained that a typical wave climate consists of waves with a wave steepness ranging from $\frac{1}{50}$ to $\frac{1}{20}$. Resulting in mean wavelengths of (26 - 65m) and extreme wavelengths of (136 - 340m). Considering a water depth (d) of 50m, the mean waves are well within the deep water regime. The extreme waves do not lie in the deep water regime, but neither are they shallow water waves; they are located in the intermediate water regime. Table 5.3 summarises the characteristics used for the sensitivity study.

As the expectations from the analytical method show that most wave deformation occurs due to high frequency waves, a fifth wave ($H_{d,s}$) has been introduced. The wave height of this wave is only 0.10 metres. Its steepness is based on the maximum steepness as calculated by Deltares (Den Bieman and Kieftenburg, 2015) on inward waterbodies, which is $\frac{1}{12.5}$, resulting in a wavelength of 1.25 m and a corresponding wave period of $T = 0.895$ s. This is a typical wave one would found on a lake. Although this wave does not look like a design wave at first sight, as it contains much less energy than the predefined ocean waves, this wave could potentially be of influence in the fatigue of the material of the VFFS, due to the strong hydroelastic interaction which results in high curvatures.

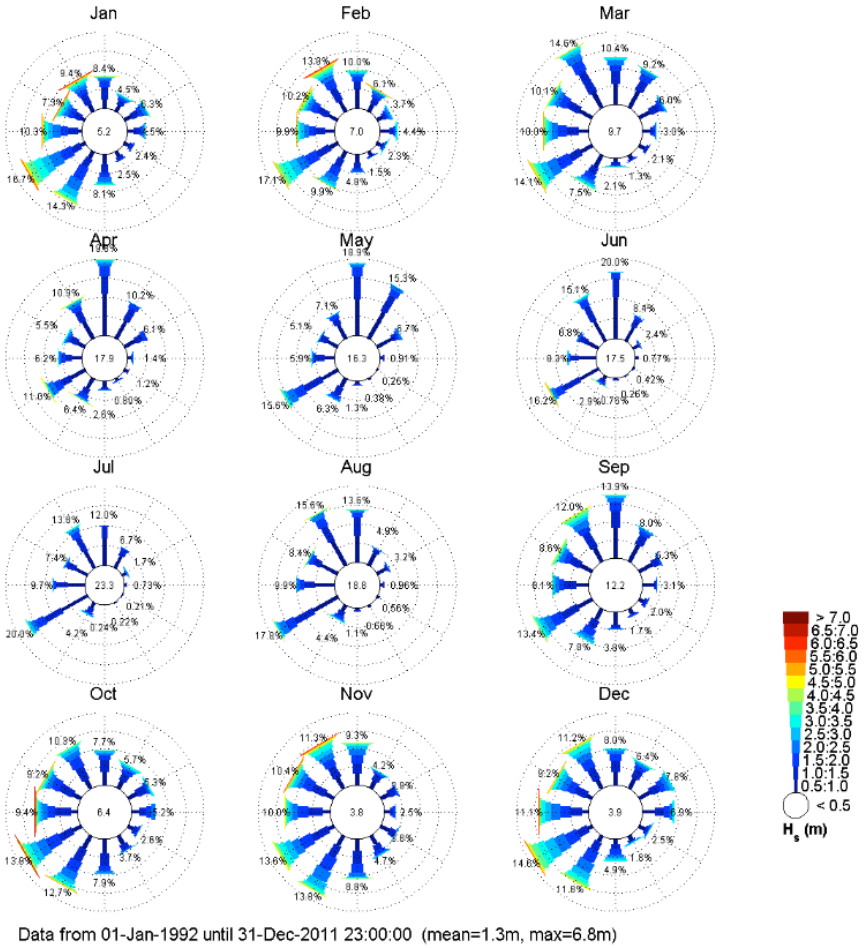

Figure 5.3: Monthly wave roses at the selected location. (Deltares, 2015)

Wave characteristics	**Symbol**	**Mean wave** $H_{d,m1}$	$H_{d,m2}$	**Extreme wave** $H_{d,e1}$	$H_{d,e2}$	**Short wave** $H_{d,s}$	**Unit**
Wave height	H_d	1.3	1.3	6.8	6.8	0.1	m
Wave steepness	$\frac{H_d}{\lambda}$	$\frac{1}{20}$	$\frac{1}{50}$	$\frac{1}{20}$	$\frac{1}{50}$	$\frac{1}{12.5}$	-
Wavelength	λ	26	65	136	340	1.25	m
Wave period	T	4.08	6.45	9.43	17.3	0.895	s
Water depth	d	50	50	50	50	7	m
Dispersion parameter	n	0.500	0.501	0.546	0.799	0.500	-

Table 5.3: Summary of wave characteristics used in the test runs.

5.2.1. Sensitivity study within analytical domain

The analytical method is bound by two assumptions. The first assumption is the zero-draught assumption, which tells us that the draught of the VFFS should be very low. In the numerical model the draught is set by the VFFS density. The theory assumes thus, that the density of the structure is very small compared to the fluid. Secondly, the theory assumes that the VFFS is able to follow the shape of the waves. Therefore, the analytical domain only describes frequencies which are lower than the natural heave period ($\omega < \omega_0$).

These assumptions imply that the theory only holds for long waves and a VFFS of limited density. The stiffness is not bound by the theory, however, in order to remain flexible, the characteristic wave-

length should remain lower than to the incident waves ($\lambda_c < \lambda_i$). However, the theory should be able to cope with stiff structures as well, as it was designed for that sole purpose. Next to this, the hydroelastic dispersion relation is valid for the full wave domain; deep water as well as shallow water. However, as the potential flow used in the numerical model does not go well beyond deep water waves, it is expected that intermediate and shallow water waves will not be captured well in the model.

From these criteria three test runs are set up for the given five characteristic waves from Table 5.3. Test run 2 is based on Schreier's experiment, but scaled to realistic offshore sizes. Although the surroundings of the VFFS are scaled using Froude scaling, the VFFS itself is not scaled using this method. The numerical model assumes no width of the structure, as the model is only two-dimensional. Therefore, only the length and height of the structure need to be scaled. However, a certain height of the structure is only needed to create enough buoyancy to carry the solar panels. It is unfavourable to have a too great thickness, as it will increase the wave loads. A full scale field study was executed by Michigan University where a 1.27 cm (half inch) thickness of neoprene rubber was used. (Mayville et al., 2020). They were able to get enough buoyancy to support the solar panels. This value will also be used in the sensitivity study. Finally, the length of the structure needs to be determined. The analytical solution assumes a semi-infinite VFFS. Therefore, the length of the structure should be long enough to assume no more change in wave deformation. To ensure this, it is decided to use a different length for each incident characteristic wave, and coupled to the incident wavelength. In Schreier's experiments, the minimum $\frac{L}{\lambda}$ ratio was five wavelengths (Schreier and Jacobi, 2020b). This should be sufficient, and at the same time reduce the computational time. The material properties are kept identical to Schreier's set-up.

Next to this test run, two more test runs are set up that follow the analytical boundary conditions. These test runs follow the zero-draught assumption, keeping the density low. The stiffness term is chosen such that wave stretching starts to occur. Test run 3 should theoretically have nearly no wave deformation. Test run 5 is chosen such that it should give significant wave stretching. As the stiffness term is a function of the incident wave number, the bending rigidity is also chosen differently per characteristic wave. The exact values are explained in the next section Expectations.

5.2.2. Sensitivity study outside analytical domain

Although the analytical method is bound by the aforementioned assumptions, the numerical model does not have this limitation. To investigate the wave deformation beyond the theoretical domain, test runs are set up with increased draught. Test run 4 is identical to test run 3, except that the VFFS density is increased such that it approximates the fluid density. The same approach has been repeated for test run 6, which mimics the input values of test run 5, but with the same increased VFFS density as in test run 4. Finally, test run 7 is based on test run 1a. The short wave of Schreier's experiment is reintroduced. This test run consists of five runs, each with an increasing VFFS density (200 - 1000 kg/m^3). This test run will investigate the effect of structure density on the hydroelastic wave deformation.

5.3. Expectations

From the given mathematics in the previous chapters, it is possible to draw expectations of the results of the numerical method. The dispersion parameter K is composed of two terms; the stiffness term and the draught term. As recalled from Equation 2.24, shown below, the stiffness term, $\left(\frac{k}{k_p}\right)^4$, adds wave stretching, whereas the draught term, $\left(\frac{\omega}{\omega_0}\right)^2$, causes wave shortening.

$$K = 1 + \left(\frac{k}{k_p}\right)^4 - \left(\frac{\omega}{\omega_0}\right)^2$$

To determine if their contributions are significant, it is stated that the terms are significant if their contributions are higher than 1%. As the terms have a power in their calculation this relates to the following conversions:

$$\left(\frac{k}{k_p}\right)^4 > 0.01 \rightarrow \frac{k}{k_p} > 0.316 \tag{5.2}$$

$$\left(\frac{\omega}{\omega_0}\right)^2 > 0.01 \rightarrow \frac{\omega}{\omega_0} > 0.1 \tag{5.3}$$

Theoretically, the stiffness term is only bound by a lower limit, the bending rigidity cannot be negative. For a bending rigidity of zero, the VFFS would behave like a fluid. There is no virtual upper limit, as the VFFS theoretically could become infinitely stiff. However, a VFFS is characterised by its flexibility, therefore it should not exceed a certain bending rigidity. According to Schreier, the definition of a VFFS is applicable for ratios of $\frac{\lambda}{\lambda_c} > 5$ or equivalently $\frac{k}{k_p} < \frac{1}{5}$. However, as previously stated, wave stretching is only significant for a stiffness ratio larger than 0.316. Hence, this would result in insignificant wave stretching for all VFFSs. The definition of the VFFS is stated as: ”structures longer than the wavelength and able to follow the local wave elevation”. This is interpreted such that the wave number could not exceed the characteristic wave number ($\frac{k}{k_p} < 1$). However, this upper limit would lead to a wave stretching of factor two. During this study a maximum wave stretching of 10% is taken into account (i.e. $\left(\frac{k}{k_p}\right)^4 < 0.1$ or $\frac{k}{k_p} < 0.562$). This results in a domain where wave stretching is experienced of $0.316 < \frac{k}{k_p} < 0.562$. This upper limit states that the characteristic wavelength ratio is $\frac{\lambda}{\lambda_c} \approx 2$.

The draught term is bound by the air density and the water density in order not to levitate nor sink, respectively. Looking at the draught term, it is expected that wave shortening intensifies as the VFFS density increases, with a minimal value of $\omega_0 = \sqrt{\frac{\rho_w g}{\rho_b h}}$ if the VFFS density equals the water density ($\rho_b = \rho_w$). Using the realistic material properties from test run 2, it follows that significant wave shortening is only experienced for angular frequencies higher than $\omega > 2.78$ rad/s or wave periods lower than $T < 2.26$ s.

$$\omega_0 = \sqrt{\frac{\rho_w g}{\rho_b h}} = \sqrt{\frac{9.81}{0.0127}} = 27.79 \text{ rad/s} \rightarrow \omega = 10\% \cdot 27.79 = 2.78 \text{ rad/s} \tag{5.4}$$

Based on the analytical method, wave deformation can be expected for both Schreier’s experiment and the sensitivity study. The wave deformation is split over two parameters; the change in wavelength and the change in wave amplitude. Using Schreier’s parameters from his two experiments, one would expect wave stretching and a decrease in amplitude for Experiment 1 (short waves), and wave shortening combined with an increase in amplitude for Experiment 2 (long waves). Table 5.4 summarises the expected outcome of the analytical method.

Name	Symbol	Experiment 1	Experiment 2	Unit
Change of wavelength	K	1.007	0.997	**-**
Change of amplitude	R	0.965	1.001	-

Table 5.4: Expected dispersion parameters of Schreier’s experiments. Wave stretching is expected for Experiment 1 (short waves). Wave shortening is expected for Experiment 2 (long waves).

For the sensitivity study, there are still two unknown variables; the bending rigidity of the VFFS and the density of the VFFS. In Figure 5.4, both variables are plotted independently to see how much influence each variable has on wave deformation. The dashed line indicates a significance of 1%. The same has been done in Figure 5.5, to show the influence of each variable on the change in amplitude. It is clear that wave stretching only occurs if the structure is sufficiently stiff; longer waves require stiffer structures in order to deform. Wave shortening, on the other hand, only occurs as the VFFS density increases; shorter waves deform more than longer waves.

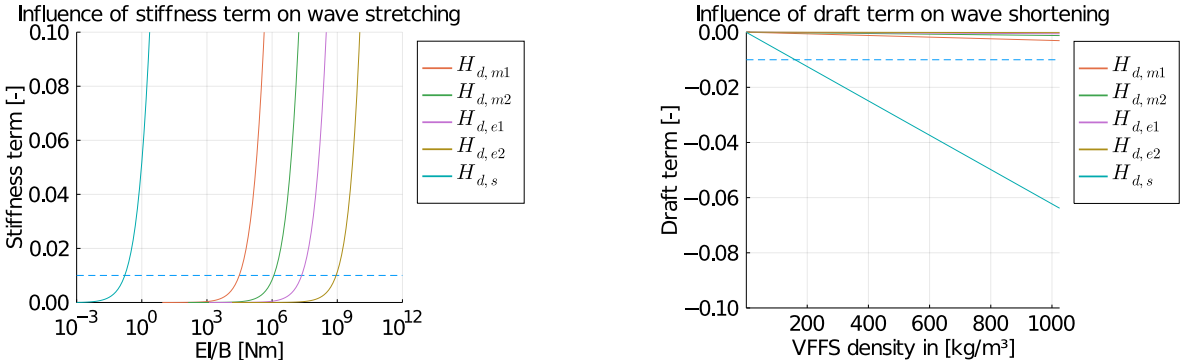

Figure 5.4: Change of wavelength due to stiffness (left) and draught (right).

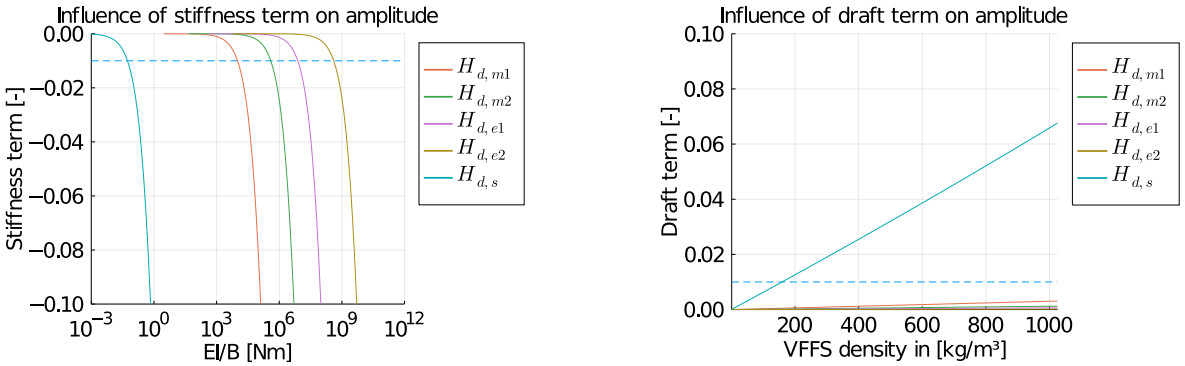

Figure 5.5: Change of amplitude due to stiffness (left) and draught (right).

However, in reality, both variables play a role in wave deformation. Therefore, a contour plot has been made including both dispersion parameters for each of the five waves. The limits of the contour plot have been chosen such, that maximum wave stretching was equal to 10%, the lower limit was obtained using an equilibrium value (below a certain value there was no wave stretching observed anymore) and has been plotted in Figure 5.6. It is expected that significant wave stretching only occurs for structures being rather stiff. Below a certain stiffness the dispersion parameters, K and R, go to one for the characteristic ocean waves. The short characteristic lake wave, $H_{d,s}$, shows values below one, which means that wave shortening is expected.

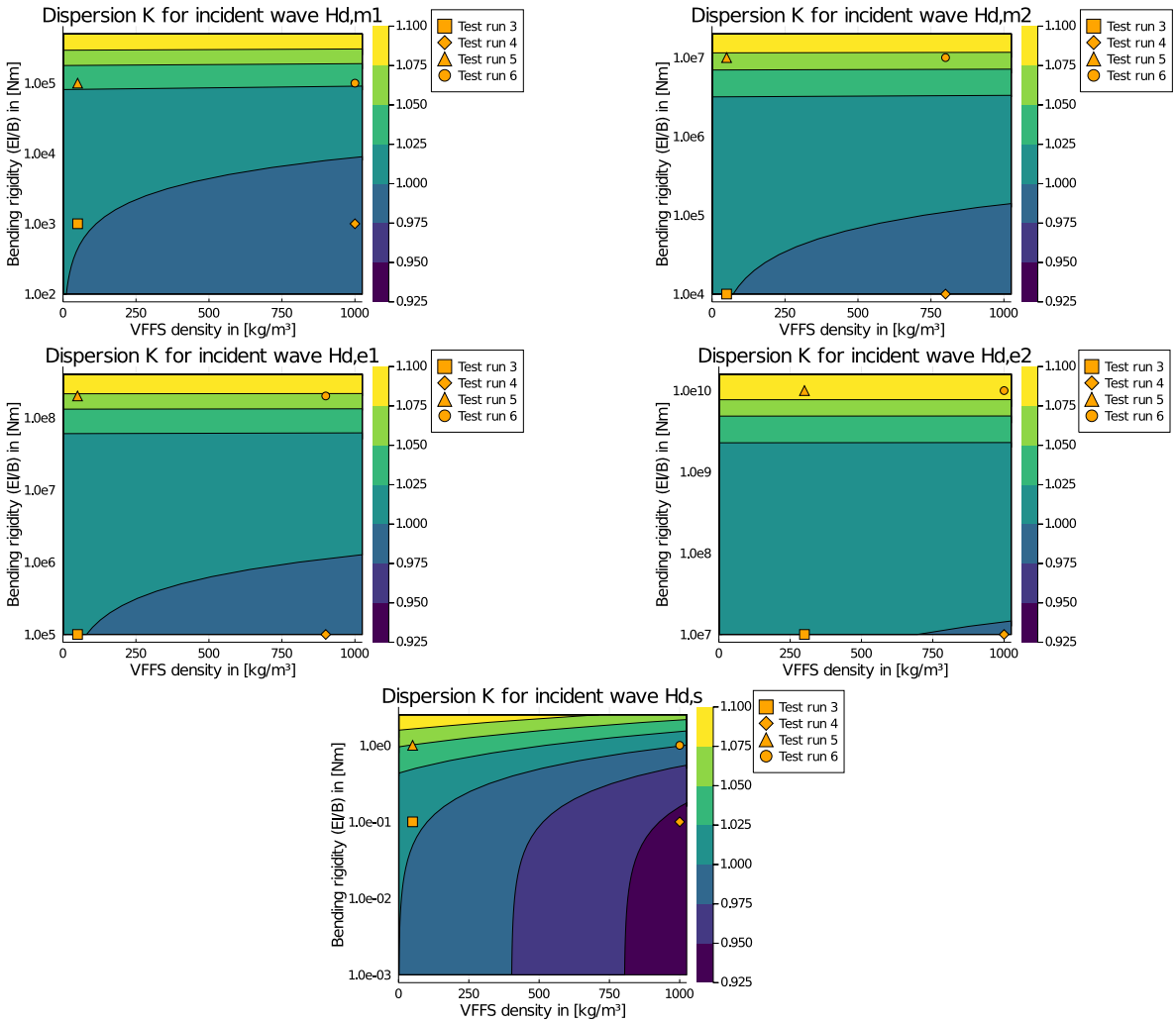

Figure 5.6: Expected change in wavelength for five characteristic waves. Note that the y-axis is different in each plot, the colours match in each plot.

To put the stiffness parameters into perspective, they are compared to existing materials. Table 5.5 shows the equivalent materials that contain a similar Young's modulus as the stiffness terms of the respected test runs. Note that the density of the material has not been accounted for. Some mentioned materials such as aluminium or tungsten carbide (used for high quality drilling equipment) do not float, which makes them unable to use as a VFFS. However, this is purely an indication if the proposed hydroelastic deformation would occur in real life. It is observed that for the extreme waves, to have a hydroelastic interaction the material of the structure should be stiffer than diamond. For significant wave deformation, even the small design waves ($H_{d,m1}$ and $H_{d,m2}$) exceed Young's moduli which are workable materials. During the calculation method, it was assumed that the thickness of the VFFS remained $h = 0.0127m$, which is very thin. Therefore, in cases where the Young's modulus alone does not give a realistic scenario anymore, the bending stiffness has been used to compare it to a concrete structure with a larger thickness. As this report is also useful for VLFS, such as floating islands, this still relates to realistic scenarios.

Test run	Low Stiffness	High stiffness
3a-4a / 5a-6a	Medium-density fiberboard (MDF)	Tungsten carbide
3b-4b / 5b-6b	Aluminium	Concrete (h = 0.16m)
3c-4c / 5c-6c	Tungsten carbide	Concrete (h = 0.43m)
3d-4d / 5d-6d	Concrete (h = 0.16m)	Concrete (h = 1.6m)
3e-4e / 5e-6e	Neoprene	Polystyrene foam

Table 5.5: Comparison of real-world materials to numerical input data.

Using the value ranges of the previous figure. Figure 5.7 shows the expected change in amplitude of the VFFS for a given VFFS density and a bending rigidity for each of the five waves. The change in amplitude shows inverse results of the dispersion parameter K. For stiff structures, the amplitude decreases towards zero for infinite rigid structures. On the other hand, the amplitude shows an increase in wave height for short waves, especially in combination with a high VFFS density.

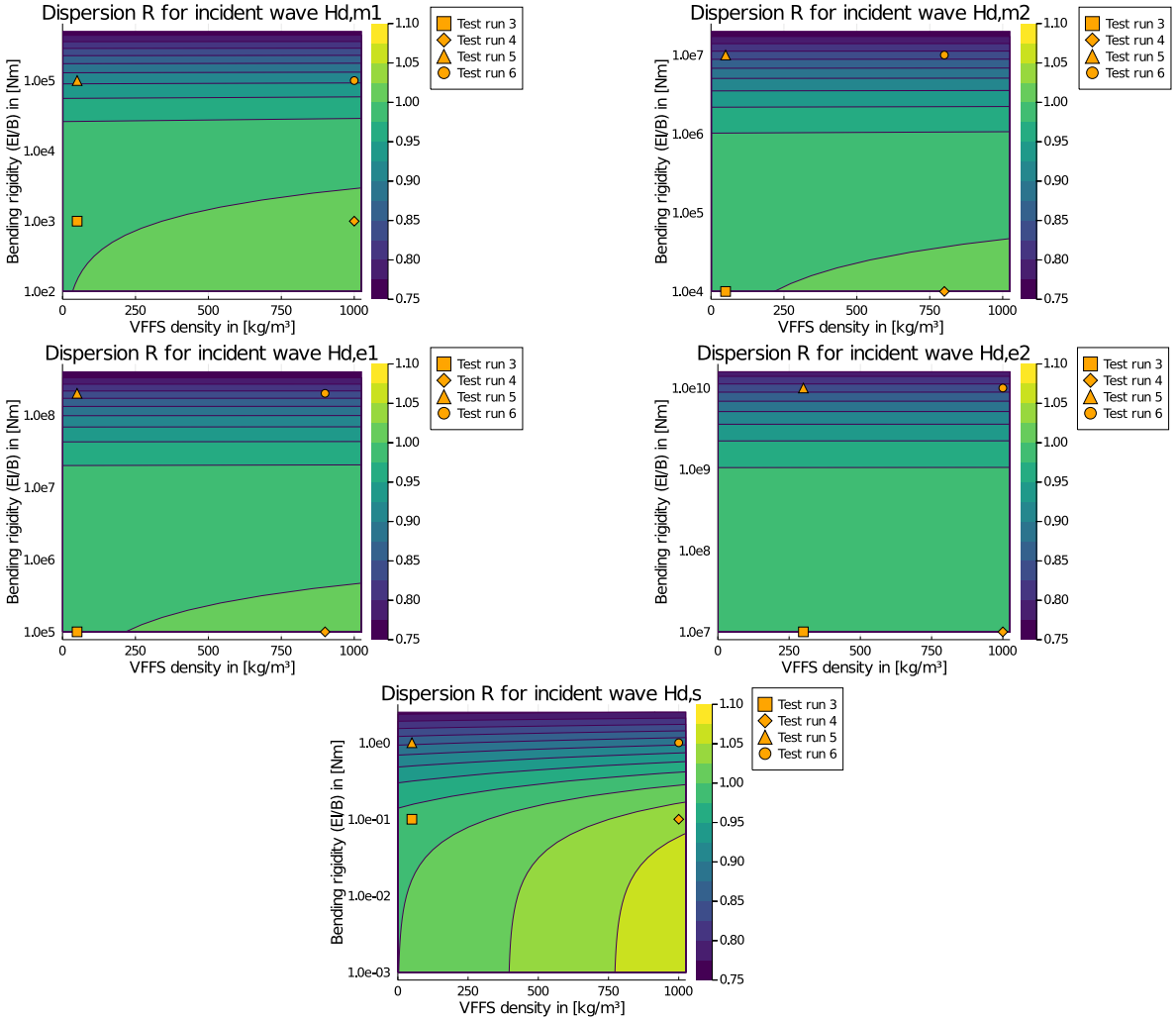

Figure 5.7: Expected change in amplitude for five characteristic waves. Note that the y-axis is different in each plot, the colours, however, do match in each plot.

From these expected results, a set of numerical test runs is compiled. For each characteristic wave, tests are run with realistic parameters of a VFFS. Furthermore, tests are run with stiffness and draught values where significant wave deformation is expected. These values could lie well out of the regime of VFFS, but are examined to see if the numerical model is also able to cope with VLFS. In Table 5.6 an overview is given of the tests which are being run.

Test run	$H_{d,m1}$		$H_{d,m2}$		$H_{d,e1}$		$H_{d,e2}$		$H_{d,s}$	
	$\frac{EI}{B}$	ρ_b	$\frac{EI}{B}$	ρ_b	$\frac{EI}{B}$	ρ_b	$\frac{EI}{B}$	ρ_b	$\frac{EI}{B}$	ρ_b
2	0.09559	116	0.09559	116	0.09559	116	0.09559	116	0.09559	116
3	1×10^3	50	1×10^4	50	1×10^5	50	1×10^7	300	1×10^{-1}	50
4	1×10^3	1000	1×10^4	800	1×10^5	900	1×10^7	1000	1×10^{-1}	1000
5	1×10^5	50	1×10^7	50	2×10^8	50	1×10^{10}	300	1	50
6	1×10^5	1000	1×10^7	800	2×10^8	900	1×10^{10}	1000	1	1000

Table 5.6: Overview of characteristic wave test runs for numerical model. $\frac{EI}{B}$ in Nm and ρ_b in kg/m^3.

Finally, as the wave deformation is expected to occur most significantly at high frequency waves, Schreier's setup is repeated one more time for the short waves. This time, only the density of the VFFS is changed. Five runs, each having an increment of the density of 200 kg/m^3. This would show how the draught of the VFFS plays a factor in the wave deformation and gives a starting point for experimental research.

Test run	$H_{d,1}$		$H_{d,1}$		$H_{d,1}$		$H_{d,1}$		$H_{d,1}$	
	$\frac{EI}{B}$	ρ_b	$\frac{EI}{B}$	ρ_b	$\frac{EI}{B}$	ρ_b	$\frac{EI}{B}$	ρ_b	$\frac{EI}{B}$	ρ_b
7	0.09559	200	0.09559	400	0.09559	600	0.09559	800	0.09559	1000

Table 5.7: Overview of draught test runs for numerical model. $\frac{EI}{B}$ in Nm and ρ_b in kg/m^3.

5.4. Comparison

To verify the numerical results, they are compared to the analytical solution. The dispersion parameters K and R are compared for the analytical solution and the numerical solution. Furthermore, the energy fluxes on both ends of the VFFS are calculated and compared to the energy fluxes of the free surface on both sides, respectively.

To compare the numerical results to the analytical solution, several factors are introduced to indicate what is calculated. These factors are the dispersion parameters K and R, each with different subscripts. The dispersion parameters are calculated on each end of the VFFS. The analytical solution is calculated using the input parameters and indicated by K_a and R_a, respectively. Subsequently, the same factors are calculated, but this time, based on the numerical results. These factors are indicated by K_n and R_n. The subscripts i and o indicate at which boundary the value is calculated. The subscript b indicates the VFFS. Finally, the 'real' solution is calculated. These are the measured numerical values of the wave number and the amplitude and indicated by K_r and R_r. The difference between the analytical solution and the numerical solution shows the error of the numerical model. The difference between the real solution and the numerical solution shows if the mathematical theory is in line with the numerical model. An overview of the used dispersion parameters is given in Table 5.8.

Name	Symbol	Calculation
Wavelength dispersion		
Analytical Solution	K_a	Equation 2.24
Numerical solution (b/i)	K_n	Equation 2.24
Real solution (b/i)	$K_{r,i}$	$\frac{k_i}{k_b} \cdot \frac{\tanh(k_i d)}{\tanh(k_b d)}$
Real solution (b/o)	$K_{r,o}$	$\frac{k_o}{k_b} \cdot \frac{\tanh(k_o d)}{\tanh(k_b d)}$
Amplitude dispersion		
Analytical Solution	R_a	Equation 2.28
Numerical solution (b/i)	$R_{n,i}$	Equation 2.28
Numerical solution (b/o)	$R_{n,o}$	Equation 2.28
Real solution (b/i)	$R_{r,i}$	$\frac{\xi_b}{\xi_i}$
Real solution (b/o)	$R_{r,o}$	$\frac{\xi_b}{\xi_o}$

Table 5.8: Overview of different dispersion parameters, used to compare the analytical and numerical results.

Next to the dispersion parameters, the energy fluxes on each side are calculated. These are indicated by P_i, P_b and P_o for the incident, VFFS and outgoing wave energy flux, respectively. These are calculated using Equation 2.44. The expected result versus the numerical values are discussed at each test run in the next chapter. The accuracy between the theoretical and measured values is given in the summary and discussed in the next chapter as well.

5.5. Overview test runs

To summarise the different test runs that have described in the previous sections, a clear overview is given here. Figure 5.8 shows the relative stiffness of each structure of the different test runs. The black dashed line denotes $\frac{L}{\lambda_c} = 5$, which indicates the lower limit for VFFS. Values lower than this line should be evaluated as VFLS. The lower limit of the plot is equal to one and as all structures are longer than their incident wavelength ($L = 5\lambda$), all test runs conform Suzuki et al.'s (2007) definition of a VFLS as shown in Figure 1.4. A detailed overview is also given in Table 5.9.

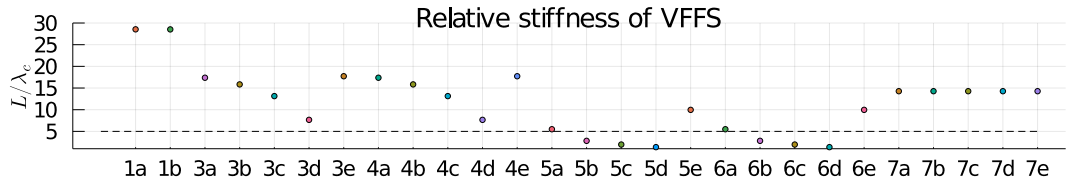

Figure 5.8: Relative stiffness of the VFFS per test run. Note that test run 2 has been omitted, as their values were beyond the scale ranging from 176 to 775 (2a-2d). Test run 2e: $\frac{L}{\lambda_c} = 7.09$.

1. Schreier's experiment (long and short waves)
2. Full scale (five design waves)
3. Low stiffness, low VFFS density (five design waves)
4. Low stiffness, high VFFS density (five design waves)
5. High stiffness, low VFFS density (five design waves)
6. High stiffness, high VFFS density (five design waves)
7. Variable draught (short waves)

Test run	**Wave**	**Stiffness** ($\frac{EI}{B}$ [Nm])	**VFFS density** (ρ_b [kg/m^3])	**Relative stiffness** ($\frac{L}{\lambda_c}$ [-])
1a	$H_{d,1}$	5.833×10^{-3}	116	28.5
1b	$H_{d,2}$	5.833×10^{-3}	116	28.5
2a	$H_{d,m1}$	9.559×10^{-2}	116	176
2b	$H_{d,m2}$	9.559×10^{-2}	116	285
2c	$H_{d,e1}$	9.559×10^{-2}	116	420
2d	$H_{d,e2}$	9.559×10^{-2}	116	775
2e	$H_{d,s}$	9.559×10^{-2}	116	7.09
3a	$H_{d,m1}$	1×10^{3}	50	17.4
3b	$H_{d,m2}$	1×10^{4}	50	15.8
3c	$H_{d,e1}$	1×10^{5}	50	13.1
3d	$H_{d,e2}$	1×10^{7}	300	7.66
3e	$H_{d,s}$	1×10^{-1}	50	17.7
4a	$H_{d,m1}$	1×10^{3}	1000	17.4
4b	$H_{d,m2}$	1×10^{4}	800	15.8
4c	$H_{d,e1}$	1×10^{5}	900	13.1
4d	$H_{d,e2}$	1×10^{7}	1000	7.66
4e	$H_{d,s}$	1×10^{-1}	1000	17.7
5a	$H_{d,m1}$	1×10^{5}	50	5.49
5b	$H_{d,m2}$	1×10^{7}	50	2.82
5c	$H_{d,e1}$	2×10^{8}	50	1.96
5d	$H_{d,e2}$	1×10^{10}	300	1.36
5e	$H_{d,s}$	1	50	9.97
6a	$H_{d,m1}$	1×10^{5}	1000	5.49
6b	$H_{d,m2}$	1×10^{7}	800	2.82
6c	$H_{d,e1}$	2×10^{8}	900	1.96
6d	$H_{d,e2}$	1×10^{10}	1000	1.36
6e	$H_{d,s}$	1	1000	9.97
7a	$H_{d,1}$	5.833×10^{-3}	200	14.3
7b	$H_{d,1}$	5.833×10^{-3}	400	14.3
7c	$H_{d,1}$	5.833×10^{-3}	600	14.3
7d	$H_{d,1}$	5.833×10^{-3}	800	14.3
7e	$H_{d,1}$	5.833×10^{-3}	1000	14.3

Table 5.9: Overview of test runs for numerical model

6

Numerical test runs

This chapter contains the results of the proposed test runs from the previous chapter. Each test run is introduced and observations of the results are given. The figures show the wavelength deformation and the amplitude deformation of each test run. Also, a table is given with the calculated dispersion parameters and the energy fluxes. The accuracy of the analytical expected solution, the numerical expected solution and the numerical measured solution is given at the end of the chapter.

6.1. Test run 1

Test run 1 is a copy of the experiments executed by Schreier and is schematised in Figure 6.1. The material parameters are identical to the test set-up and the incident waves have the same shape as in the towing tank. The first column of Table A.1 shows the expected results test run 1a. Wave stretching was expected for the short waves as K_a was larger than one. Figure A.1 also shows that this expectation is true. Likewise, the amplitude was expected to decrease as R_a was lower than one. Looking at Figure A.1 once again, this is also observed in the numerical model. Finally, something interesting is observed in the wavelength calculation plot. At both interfaces between the free surface and the VFFS, the wavelength is changing significantly. According to Ohmatsu (2005) this can be explained by the fact that this is a transition zone between the two wavelengths and this zone is governed by an infinite complex wave number.

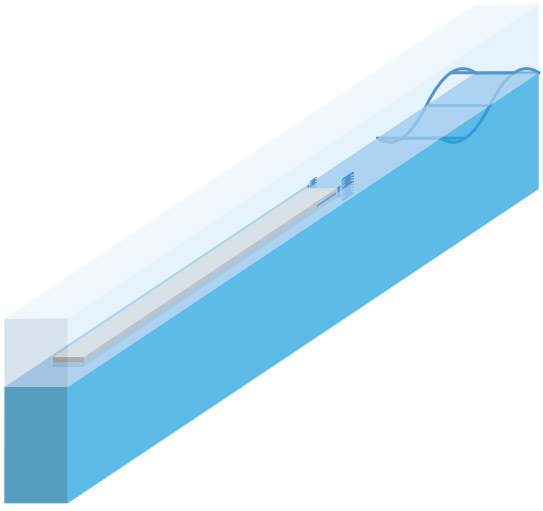

Figure 6.1: Illustration of towing tank test run 1.

The same process has been repeated for the other test set-up, where long waves were imposed on the VFFS. This time, wave shortening was expected, together with an amplitude increase. Although, the wavelength decreased, an increase in amplitude was not noticed, as both R_{ri} and R_{ro} were not higher

than one. The amount of wave shortening is also lower than possible errors, which could have been the cause. This is in line with the results presented by Schreier and Jacobi (2020b).

As a comparison to Schreier and Jacobi (2020b) results, the numerical results have been plotted on top of their presented results in Figure 6.2. In both cases it is observed that the wavelength is shorter for the numerical results than the experimental results. For the long waves this could be due to the fact that the numerical test runs experienced wave shortening whereas this could not be confirmed in the experimental set-up. For the short waves, it is clearly visible that the amplitude of the numerical result is significantly higher than the experimental set-up. The proposed amplitude of 10mm was not perfectly achieved during the experiments. Therefore the wave parameters might not align well with the numerical results. In the experiment of the short waves, 3D effects were observed as the centre line shows lower amplitudes with larger wave stretching than the sides.

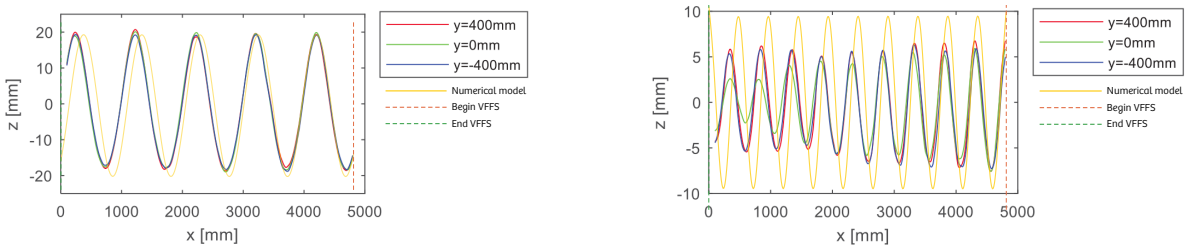

Figure 6.2: Overlay of numerical results on top of experimental research from the towing tank for long waves (left) and short waves (right).

6.2. Test run 2

The second test run describes a realistic sized (see Figure 6.3) VFFS with material parameters identical to Schreier's test set-up. The thickness of the VFFS is larger than in test run 1; 0.0127 m versus 0.005 m. The length of each VFFS is chosen such that the incident wave fits five times in the structure. Due to wave deformation, this might change slightly. The incident waves in this test run are five characteristic waves that occur at sea (1-4) or at a lake (5). The first two waves are mean ocean waves (a and b), the other two are extreme ocean waves (c and d) and finally a typical wave that is found on a lake (e) is imposed. This is repeated for test runs 3, 4, 5 and 6 as well.

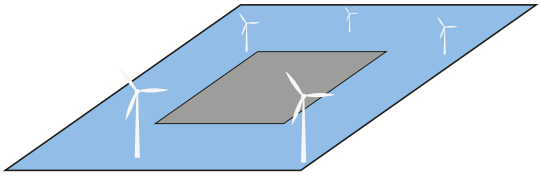

Figure 6.3: Illustration of full scale test run 2.

The VFFS is very flexible compared to the incident waves. Therefore, no wave deformation was expected for any of the four characteristic ocean waves (a-d). This also turned out to be true for the wavelength deformation. For each of the four waves, there is some noise visible on the incident wave side. This indicates on small wave reflections being trapped in the system. Also, in contrast to the previous test run, no transition zone at the interface of the free surface and the VFFS is observed. Furthermore, it is observed that the measured amplitude on the outgoing wave side is lower than the incident wave side. Finally, it is noticed that for test run 2d, the measured amplitude dispersion factor R_{ri} differs significantly from the theoretical value. The right plot of Figure A.6 shows that the shape of the top amplitude is concave and of the bottom amplitude is convex in the hydroelastic zone. This explains why the dispersion factor does not match the result. A reason for this behaviour could be that the design wave is not in deep water, but in the intermediate water regime ($n = 0.799$).

Looking at the fifth characteristic wave in Figure A.7, the behaviour of the infinite complex wave number is back on the interfaces of the free surface and the VFFS. Also, the expected wavelength dispersion

is only 1‰, but the expected amplitude deformation is more than 1% and measured as well. This is interesting, as in test run 1, the increase in wavelength went hand in hand with a decrease in amplitude, and vice versa. However, test run 2e shows that both parameters could decrease at the same time as well.

6.3. Test run 3

The third test run uses the same five characteristic waves as input, but the material properties of the VFFS have changed. In the next four test runs (3-6), the stiffness of the VFFS and the density of the VFFS are changed, independently, such that the influence of both terms can be investigated. First, in test run 3, a low density value is chosen together with a low stiffness term (see Figure 6.4). Therefore, it is expected that the VFFS should react similarly to the incident waves as in test run 2.

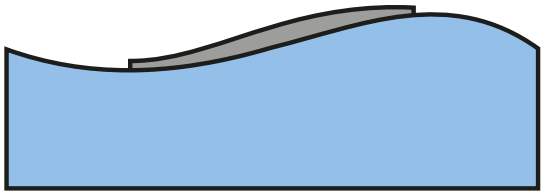

Figure 6.4: Illustration of flexible light structure of test run 3.

For the first four characteristic waves, almost no wave deformation was expected. The measured values in the tables also confirm this expectation. Test run 3d is an exception to this. Like in test run 2d, the measured amplitude factors do not match with the theory. This is again possibly related to the fact that $H_{d,e2}$ is not a deep water wave. Although, the wave deformation is very small among the other runs, the infinite complex wave number is observed in each of the test runs. It is also noticed, that the measured values of the incident wave side are much more in line with the expected result than the measured results on the outgoing side.

Finally, in test run 3e, some wavelength stretching is observed, together with a significant amplitude decrease. The numerical model shows nearly identical results with errors ranging only 1‰.

6.4. Test run 4

The fourth test run uses identical values for both the incident waves as well as the material properties as the third test run, except for the density of the VFFS. In this test run, the density of the structure is increased such that it nearly has the density of the fluid. This results in a much higher draught of the VFFS (see Figure 6.5). As previously explained in the theory, the draught term is responsible for wave shortening. Therefore, this is also expected behaviour for the shorter waves, as higher angular frequencies intensify this effect.

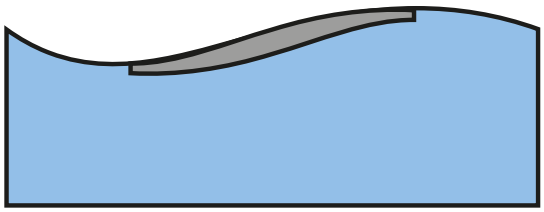

Figure 6.5: Illustration of flexible heavy structure of test run 4.

The expectations of wave shortening are met when looking at test run 4a, 4b and 4c. Wave shortening also seems to lead to an increase in wave amplitude, as this is observed for these test runs as well. Again, the theoretical values align much better on the incident wave interface than on the outgoing wave interface.

Test run 4d does not show any wave shortening, which was not expected either. There was also

no amplitude deformation expected. However, the measured values indicate that an amplitude drop of 3% was observed.

Finally, test run 4e contains a much shorter incident wave than the previous four characteristic waves. Therefore, much more wave shortening was expected and by looking at Figure A.17, significant wave shortening of more than 5% is observed. Together with the wave shortening, an amplitude increase was expected. And although this was not observed at the incident wave interface, the outgoing wave interface shows a significant amplitude difference; even more than expected. Also, relatively much noise is observed on the incident wave side, which is an indication of possible wave reflection.

6.5. Test run 5

In the fifth test run, the VFFS density returns to the same low value as used in test run 3. However, in this test run, the stiffness is increased to a point that significant wave stretching is expected. This increased stiffness changes the material properties of the structure by this much, that the term VFFS might not be applicable anymore (see Figure 6.6). Instead there should be referred to the structure as VLFS (Very Large Floating Structure). However, as the theory is based on the latter type, the analytical solution is expected to be valid. The application of flexible floating solar panels is perhaps not possible anymore.

Figure 6.6: Illustration of stiff light structure of test run 5.

For all five characteristic waves, significant wave stretching and a corresponding amplitude reduction is observed. Four of the five incident waves show numerical values as expected by the theory. Only the measured value of the very large wave from 5d does not align with the theory. This could be due to the fact that it is not a deep water wave. It is also observed that although the noise on the incident wave side is relatively large compared to previous test runs, the measured wavelength in the structure is very stable. Finally, the infinite complex wave numbers on both interfaces of the VFFS are visible. What is interesting and different than previous test runs, is that the peaks of the graphs as seen in Figure A.20 are much larger and exceed the 10% limit of the graph.

6.6. Test run 6

Finally, the sixth test run is the final test run that looks into the combination of stiffness and density. This test run contains a structure with both a large stiffness as well as a large density (see Figure 6.7). Therefore, both wave stretching as well as wave shortening is expected. The five characteristic waves each have different wavelengths and periods, which results in different behaviour of the wave deformation. For the first four characteristic waves, wave stretching is expected to be dominant. For the last wave, due to its short period, it is expected that the contribution of the stiffness cancels the large draught of the VFFS.

Figure 6.7: Illustration of stiff heavy structure of test run 6.

The expectations for the first four waves are met. The larger draught almost has no influence on the

wave deformation, as the angular frequency of the characteristic waves is simply too low. On the other hand, looking at the fifth characteristic wave in Figure A.27, there is a significant difference compared to A.22. The draught term completely canceled the wave stretching. Interestingly, the change in amplitude was not canceled, nor was expected. Although, the expected decrease in amplitude did not align perfectly with the measured results; being off 3%.

Figure 6.8 shows an overview of the dispersion accuracy of the test runs three to six. The colour of each symbol represents the imposed design wave and the symbol itself corresponds with the material parameters as given in the previous chapter.

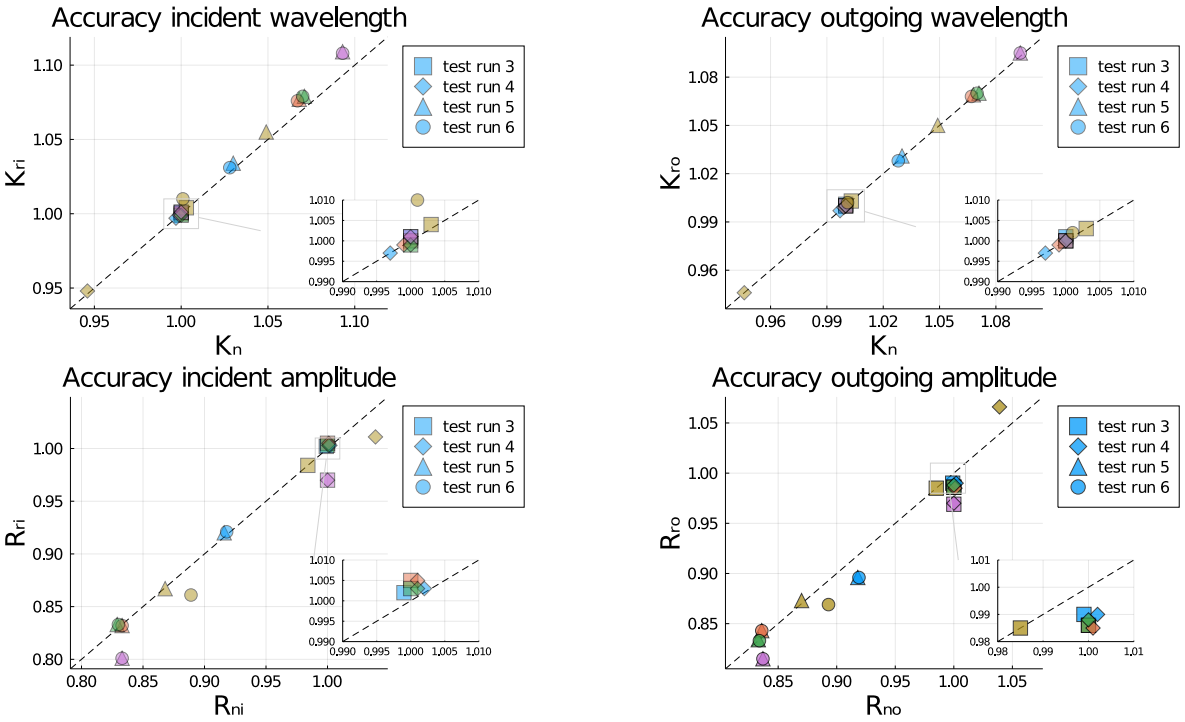

Figure 6.8: Wavelength dispersion of the incident (top left) and outgoing (top right) wave interface and amplitude dispersion of the incident (lower left) and outgoing (lower right) wave interface. (– $H_{d,m1}$; –$H_{d,m2}$; – $H_{d,e1}$; – $H_{d,e2}$; – $H_{d,s}$)

6.7. Test run 7

The seventh and final test run shows the influence of the draught of the VFFS on wave deformation. As the theory describes, a higher draught implies more wave shortening. Therefore, test run 7 consists of five test runs, with an increasing VFFS density, starting at 200 kg/m^3 all the way to 1000 kg/m^3 (see Figure 6.9). The size and the material parameters of the structure is again the same as Schreier's test set-up and the incident wave is the same as the short wave he used in his experiment. The expectations of the first test run (7a) should, therefore, be very similar to test run 1a.

Figure 6.9: Illustration of variable draught of the structure of test run 7.

As expected, test run 7a shows almost no wave deformation (see Figure A.28), although the infinite complex wave number is clearly visible on both interfaces of the VFFS. As the structure gets more

dense, the incident wave gets shortened more as well. Interestingly, the expected amplitude deformation is lower than one for 7a, 7b, 7c and 7d. Only the last test run (7e) expects an increased amplitude in the VFFS. It is also observed in the tables that as the density increases, the error between the theory and the measured values increase. This confirms that the theory is only able to describe the fluid structure interaction given its assumption of zero-draught.

6.8. Accuracy

The results are split into three parts. First the accuracy of test run 1 is evaluated. This is the copy of Schreier's experiments. Secondly, the accuracy of test runs 2, 3 and 5 are evaluated. They all contain input parameters for which the analytical solution is expected to hold. Finally, test runs 4, 6 and 7 are evaluated. These test runs are not covered by the analytical method and therefore may differ from the expected analytical outcome.

6.8.1. Accuracy Schreier's based numerical set-up

To define the accuracy of the dispersion parameters the root mean square error has been calculated for all individual test runs, as well as for each ratio. The results are summarised in Figure 6.10. The first, fourth and fifth column show the difference between the analytical expected value and the numerical expected value. In both test runs, five out of six ratios are equal to 1.000, one is $1‰$ off. This means that the numerical incident wave is identical to the input values of the model.

The second and third column show measured wavelength dispersion versus the numerical expected value. Both measured values are identical to the expected value; on the incident wave side as well as on the outgoing wave side.

The sixth and seventh column show the ratios between the measured amplitude deformation and the expected amplitude deformation. The incident wave side corresponds perfectly with the expected value, the outgoing wave side shows a small difference.

Finally, the measured energy fluxes on either side are compared to the expected values. On the incident wave side, they are highly accurate. On the outgoing wave side the difference is very small for the short waves, but for the long waves, the difference is reasonably large. Especially, as for the long waves, no significant hydroelastic wave dispersion was expected.

The overall accuracy of the short waves was higher than for the long waves. The accuracy of the wavelength dispersion is nearly one. On the other hand, the amplitude dispersion shows small differences, especially on the outgoing wave side. These small errors also reflect to the energy fluxes, as that is a function of both parameters.

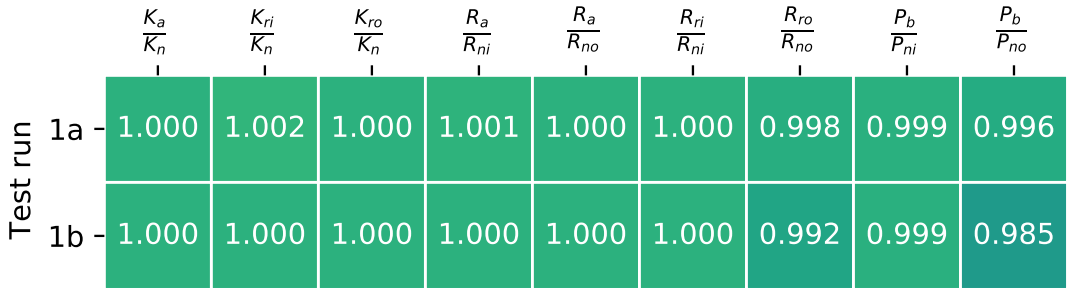

Figure 6.10: Summary of accuracy of dispersion parameters of test run 1.

6.8.2. Accuracy sensitivity study within analytical domain

The accuracy of the this part of the sensitivity study is expected to be higher than the next part. In Figure 6.11 an overview of all dispersion parameter ratios is given. The test runs are discussed independently and observations are done to deviating results.

Test run 2
Test run 2 consists of five test runs, each with different wave characteristics. The overall wavelength dispersion ratios are highly accurate, except for the measured wavelength dispersion on the incident wave side of test run 2e. This characteristic wave is much shorter than the other four. It could be, that more wave deformation occurs on the incident wave side, as the VFFS is relatively stiffer compared to the other waves. However, the outgoing wave side shows nearly identical measured results as the expected wave deformation.

It is also observed that test run 2d shows large differences between the expected amplitude deformation and the measured amplitude deformation. A possible reason to this, could be the fact that the characteristic wave at this test run is so large that the wave no longer behaves as a deep water wave.

Test run 3
Test run 3 has an increased stiffness compared to test run 2, however, it is still considered flexible. Wavelength dispersion is highly accurate compared to the expected values. Amplitude dispersion on the incident wave side is also in line with the expected values, except for test run 3d. The amplitude dispersion on the outgoing wave side is less aligned with the expected values, for the ocean waves. The shorter characteristic lake wave is nearly identical as the expected amplitude deformation.

Test run 5
Test run 5 is similar to test run 3, except the stiffness of the VFFS has increased significantly. For each test run, wavelength stretching of several percent is expected. Figure 6.11 shows that the numerical model copes well with the hydroelastic wave deformation. Except for test run 5d, all other four characteristic waves show good approximations to the analytical method for wavelength dispersion and amplitude dispersion on the incident wave side. The outgoing wave side is less accurate.

Figure 6.11: Summary of accuracy of dispersion parameters of test runs 2, 3 and 5.

6.8.3. Accuracy sensitivity study outside analytical domain

Finally, the third part of the test runs includes numerical tests which may not be well described by the analytical method, as they are outside of the boundary conditions, imposed by the zero-draught assumption. An overview of the dispersion parameter ratios is given in Figure 6.12.

Test run 4

Test run 4 is identical to test run 3, with the exception of the VFFS density, which has been increased to nearly the fluid density. The wavelength dispersion is well in line with the expected values. Although the ocean waves do not change much in wavelength, the lake wave has significant wave shortening, which is well captured. The measured amplitude deformation, however, does not fit with the expected results. Especially, test run 4d and 4e do not correspond. The numerical results of test run 4d are possibly inaccurate due to the fact that $H_{d,e2}$ is not in the deep water regime. In the case of test run 4e, the effect of hydroelastic wave deformation is stronger when waves get shorter. Therefore, the results may also differ more compared to the other test runs.

Test run 6

Test run 6 is identical to test run 5, except for the VFFS density, which has been increased significantly. The density of the structure are identical to test run 4. This test run shows a scenario where a relatively stiff structure is combined with a high draught. The measured wavelength deformation generally corresponds well with the expected results, except for test run 6d. Again, this is possibly due to the large wave. An interesting observation is made in test run 6e, where almost no wavelength dispersion is measured. The large stiffness of the VFFS in combination with the large draught predict significant wave deformation. However, the two terms seem to cancel each other. Contrary to the dispersion factor K, the amplitude deformation is significant in test run 6e (see Figure A.27. However, the analytical method was not able to capture this change in amplitude well. Neither was the theory able to cope well with the amplitude deformation for the other test runs, as significant change of amplitude was observed in the numerical results.

Test run 7

Finally, test run 7 was initiated to see what the influence of the draught term has on the hydroelastic wave deformation of the VFFS. All input values are identical to test run 1a, except for the density of the structure, which has been increased with 200 kg/m^3 in each test run. This test run focuses on a very flexible structure, as the stiffness term is very low, combined with different draughts. It is observed that the expected wavelength dispersion corresponds well with the measured results, especially on the outgoing wave side. The improved accuracy on the outgoing wave side versus the incident wave side is possibly due to wave reflection on the incident wave side. Looking at Figure A.28 and Figure A.32, there is more noise observed at test run 7e than in in test run 7a on the incident wave side, which could indicate wave reflection, but the total amount of energy in the system does not increase over time. Therefore, it is expected to be numerical instability. The outgoing wave side does not have this noise, and wave reflection is also not expected in this region as the damping zone will dissipate all energy. Looking at the amplitude deformation ratios, it is observed that as the VFFS density increases, the accuracy of the expected amplitude deformation decreases. All five test runs show significant amplitude deformation. It was expected that the first test runs were well described by the theory, as test run 7a is still within the analytical domain. As the VFFS density increases, the difference between the measured amplitude deformation and the expected results starts to deviate. Also interesting to notice, is that test run 7a shows a lower amplitude of the structure compared to the incident and outgoing wave side. However, test run 7d and 7e show that the outgoing waves are lower than the hydroelastic waves in the VFFS.

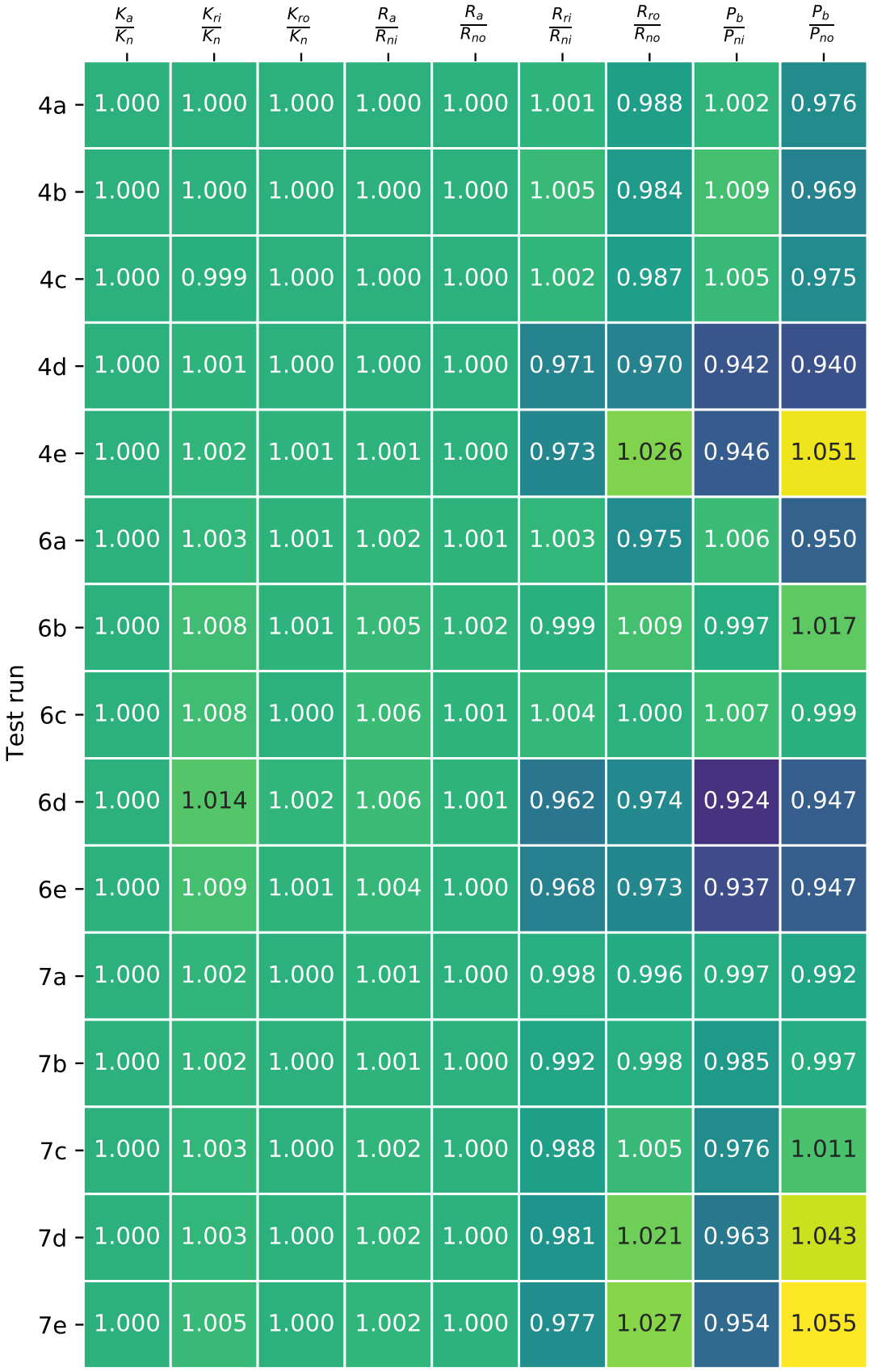

Figure 6.12: Summary of accuracy of dispersion parameters of test runs 4, 6 and 7.

6.9. Stability analysis

As the numerical model is stabilised with several stabilisation parameters, an analysis is done on the accuracy of the results versus the amount of energy in the system. Throughout the test runs, the default value of $\alpha_h = 0.5$ had been used, as this gave very accurate results. However, Colomés et al. (2021) are currently researching the optimal stability of the system. Figure 6.13 shows the energy flux balance in combination with the measured wave deformation for several values of α_h.

Test run 1a has been used to see if the energy flux matches the expected wave deformation results. For a value of $\alpha_h = 0.5$ the wavelength dispersion is very accurate matching the expected result within 1‰. However, the energy flux in the structure (red line) is lower than the energy flux on either side of the interface. High values of α_h result to better stabilisation, but drain energy from the system. Therefore, it is investigated if lower values for α_h could resolve the issue. Choosing $\alpha_h = 0.01$ gives very accurate results for the energy flux in the system. However, looking at the dispersion of the incident wave, the hydroelastic zone shows wave shortening where wave stretching was expected. The wave deformation result clearly does not match.

Going even lower by choosing $\alpha_h = 0.001$, the wave deformation result even worsens and the energy flux balance is also incorrect with a higher energy flux in the structure compared to the free surface zones.

However, for all three scenarios, the energy flux at the incident wave side is nearly identical to the energy flux of the outgoing wave side. This means that the energy is conserved, only the calculation in the structure is slightly off. As Colomés et al. (2021) are currently working on this mismatch, a solution to this issue is expected to be found in the near future.

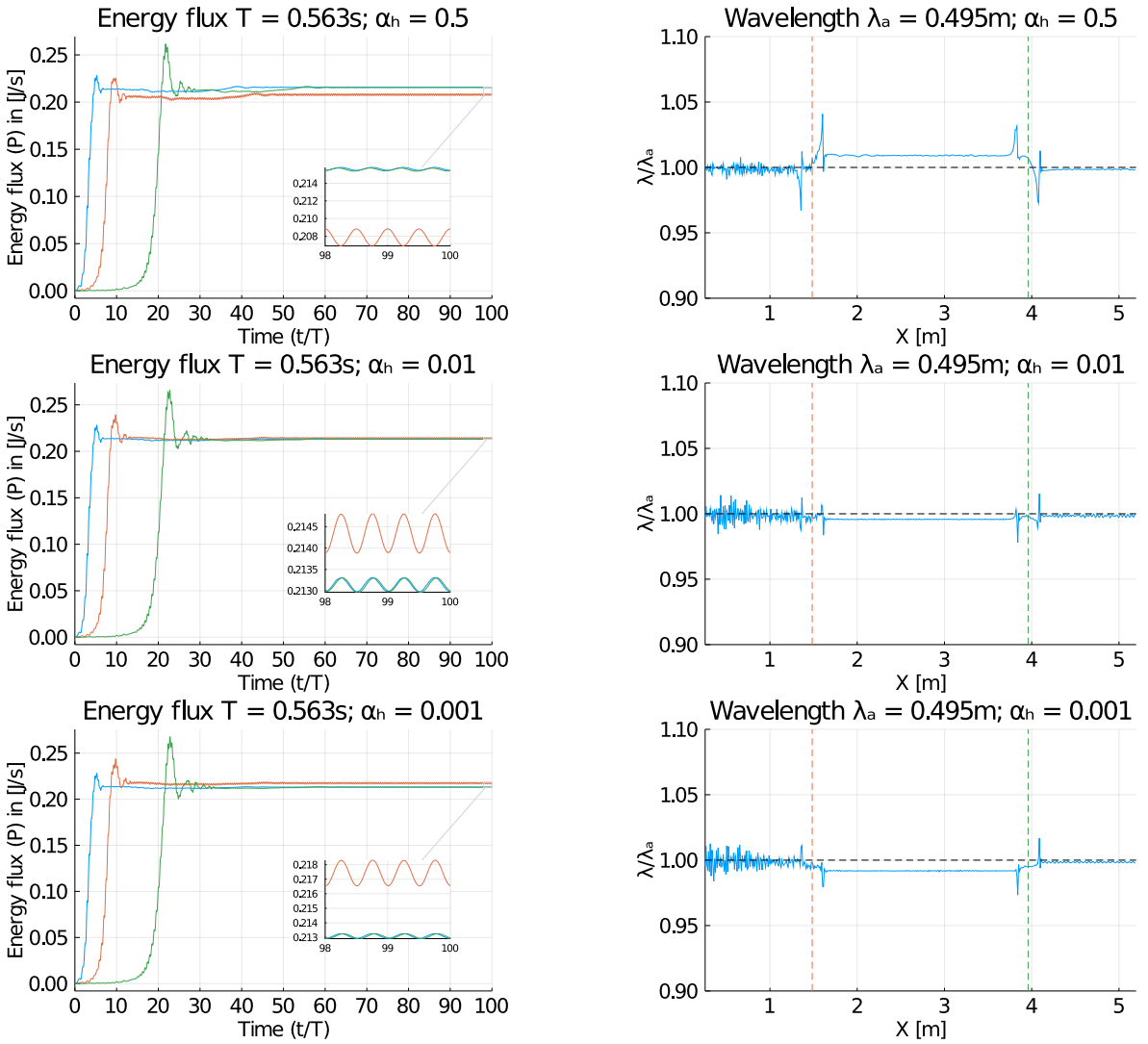

Figure 6.13: Energy flux at three locations of short waves (left). (Left plots: – Energy flux at $X = 3\lambda$ (incident wave zone); – Energy flux at $X = 5\lambda$ (hydroelastic zone); – Energy flux at $X = 8\lambda$ (outgoing wave zone), Right plots: – Wavelength; - - BeginVFFS; - - End VFFS; - - Original wavelength))

7

Discussion

The numerical model shows to be a good alternative to the analytical solution. It is a versatile solution as its input parameters, such as fluid density, VFFS density, structural stiffness and length, can easily be changed. It works both in 2D as well as in 3D, which opens the possibilities to experiment with irregular shapes or heterogeneous materials as well. The model is lightweight and able to run on a standard computer without any effort.

The results of the different test runs are individually discussed as several phenomena have been tested. First the towing tank experiment will be discussed, followed by the full scale set-up. The sensitivity study shows the limits of a VFFS and where the rigid VLFS domain starts. Finally, the influence of the draught of the structure is discussed.

7.1. Towing tank experiment

The numerical results of test run 1 show an overall good performance. The expected hydroelastic wave deformation is captured well by the numerical model. The results found by Schreier and Jacobi (2020b) corresponded with the numerical findings. In this study only 2D simulations have been executed as the focus of this research was to build a stable alternative for the analytical model. The physical experiments in the towing tank also showed 3D effects among which diffraction of the wave energy. This was not observed in the 2D test runs, but the numerical model is able to run 3D test cases as well. However, these runs are computational intensive did not fit in the scope of the project.

Next to this, the 3D effects can be deducted from the 2D results. Wave stretching is connected to diverging waves, whereas wave shortening is related to wave focusing. The latter only occurs if the draught of the structure dominates over the stiffness of the VFFS. For stiff applications such as floating islands or floating airports, wave focusing is unlikely to happen. For flexible structures like floating solar parks, it is important to design such that the zero-draught assumption remains valid, in order to overcome this issue.

7.2. Full scale set-up

Test run 2 was dedicated to a full-scale set-up of a VFFS. The material properties were matched to realistic dimensions and five design waves were chosen to see its response. It was found that for large ocean waves, the VFFS did not have much interaction with the free surface waves. They were simply too large and the floating structure is so flexible that it just moved up and down.

In case of the design wave lake, there was a noticeable wave interaction. Although the wave deformation was very low, the hydroelastic interface showed large fluctuations of the wavelength. Although the load of a lake wave is less profound than of oceanic waves, the lifetime of the structure could potentially be heavily reduced due to changing curvatures.

7.3. Sensitivity study

The sensitivity study was done to find the limits of the VFFS and to see in which cases significant (>1%) hydroelastic wave deformation would occur. The analytical solution told us that two phenomena are responsible for a change in wavelength and amplitude; the bending rigidity and draught will stretch or shorten the wave, respectively.

The wavelength dispersion showed really similar results between the numerical and the analytical solution. However, for the calculation of the amplitudes, the analytical approach is bounded by the assumption of a zero-draught, which means that the structure floats on top of the free surface line.

Test run 3 (flexible and zero-draught) and 5 (stiff and zero-draught) showed the influence of the bending stiffness of the structure. As the material properties of these test runs were within the analytical regime, they showed very similar results.

Test runs 4 (flexible and non-zero-draught) and 6 (stiff and non-zero-draught), however, lie outside the analytical domain. The numerical results of these cases could therefore not verified by the analytical solution. However, as the model itself was not changed and remained stable, there is enough confidence to state that these results are accurate as well. Experimental research could help to verify this statement.

Test run 4e shows something unexpected. Whereas, normally, the amplitude of the structure is restored to the incident wave amplitude once it enters the outgoing wave zone, this time it is further decreased. As this behaviour is odd, it was decided to deeper dive into the effect of the density of flexible structures. Test run 7 focuses on this and this phenomenon is further explained below.
Another interesting observation was done during test run 6e, where both the stiffness, as well as the draught of the structure were increased, so that the wavelength dispersion would cancel out, but the amplitude deformation would still occur. This expected behaviour sounds contradictory, however, the numerical model confirmed this expectation. The energy here clearly enters the structure. However, it is also released at the outgoing wave interface. This shows that designing for specific sea-states could help in extending the lifetime of the structure, as fatigue could be minimised due to the absence of wavelength deformation and less curvature due to lower amplitudes.

7.4. Influence of draught

The influence of the draught of the structure is highly interesting as the draught leads to wave shortening, which in its turn could lead to wave focusing under 3D objects. The same set-up as the towing tank experiment has been used, only the density of the material was changed. The expected wave shortening was clearly observed. For small wave shortening cases (7a and 7b), the amplitude drops in the hydroelastic zone and returns to its original wave height.

However, for larger structure densities (7c, 7d, 7e), the amplitude drops, once the wave enters the hydroelastic zone, but drops again once it travels out of the structure. This effect intensifies as the structure density increases. The wavelength of the traveling wave, however, follows the expected behaviour and returns back to its original shape. As this behaviour was not expected, an energy flux balance was established to examine the energy flux in each of the three zones (incident, hydroelastic and outgoing wave zone). As was shown in Section 6.9, the stability analysis of the system showed that further optimisation of α_h is necessary. Therefore, the results of this test run could contain numerical errors. However, it also opens up the opportunity to investigate the possibilities of flexible submerged wave dampers, as the combination of flexible structures with a large draught show lower amplitudes in the outgoing wave zone than in the incident wave zone.

7.5. Adaptability

The numerical model showed to cope well with different material properties. Both the bending rigidity as well as the density of the structure can easily be altered. Also, the dimensions of the structure can easily be changed. This creates an opportunity to cheaply test a wide variety of test set-ups, in a rela-

tively short period of time.

Besides the material, it was also shown that regular waves could be imposed without any difficulty by imposing a periodic horizontal velocity on the inlet of the domain. This velocity profile is easily changed to more complex types, such as irregular waves, to mimic a sea-state.

The model also showed to be give consistent results among different water depths. Both deep water and intermediate water have been tested for the fluid structure interactions and both gave accurate results. Although potential flow is able to describe shallow water, it has not been tested, as other bottom induced phenomena, such as shoaling, start to play a role as well.

7.6. Possibilities

The model has been programmed in such a way that it can be upscaled to a 3D domain without changing the code. Unfortunately, the available computer power was not sufficient to run a 3D test run with resolutions high enough to investigate the 3D effects observed by Schreier and Jacobi's (2020b) experiments. The Gridap module needs optimisation to cope with such large matrices, as it flooded the computer RAM memory. However, with the needed adaptations, it is possible to run 3D models as well as is shown in Figure 7.1.

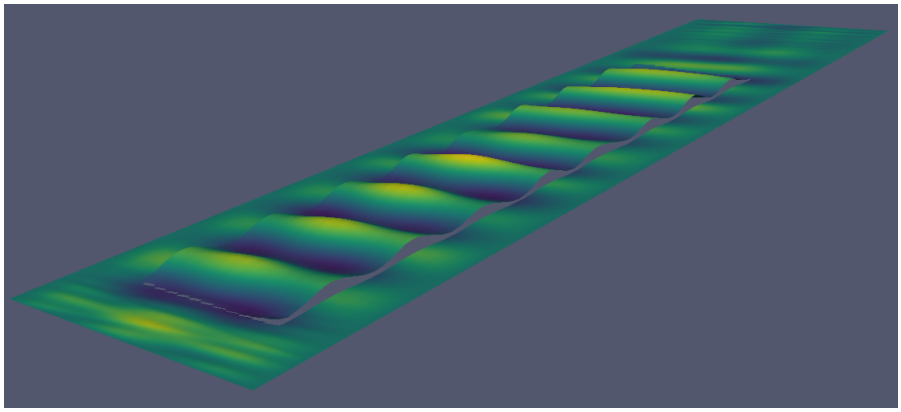

Figure 7.1: Render of 3D numerical model in Paraview.

If the 3D model is further explored with the necessary hardware tools, it also becomes possible to model irregular shapes, such as stars or ovals, without any difficulty. This is a huge advantage over the analytical approach.

8

Conclusion

The numerical model showed to be a great alternative to the analytical solution and shows similar results to early experimental research. During the calibration, the method proved to be energy conservative and identical to the expected analytical solution, both for a scenario where only waves are present in the system, as well as for the situation of a floating Euler-Bernoulli beam.

The test runs showed that the hydroelastic wave behaviour as observed in experimental research of a VFFS is well mimicked by the numerical model. Compared to the analytical solution the numerical results also correspond well within the given boundary conditions of the theory. This verifies the correctness of the numerical model versus the theory and vice versa. Outside this domain, the numerical solution cannot be verified by the analytical solution. However, there is good reasoning to assume that the numerical results outside this domain are correct, as the model has not changed.

Hydroelastic wave deformation (which consists of wavelength deformation and amplitude deformation) is related to three parameters: two material parameters and the incident wave. The stiffness of the VFFS provides wavelength stretching and the draught of the structure is decisive on the amount of wavelength shortening. A combination of the two material parameters could give a combination where they cancel each other out. No wavelength dispersion is then experienced. The amplitude deformation is more complicated and is generally opposed to the wavelength deformation; wave stretching is followed by an amplitude decrease and wave shortening is connected to an increase in amplitude. However, there are also scenarios where there is no wavelength deformation, but the amplitude deforms in the hydroelastic zone. This is especially useful when designing for lower amplitudes.

The incident wave influences the intensity of wave deformation, where high frequency waves have a larger influence on the hydroelastic wave deformation than low frequency waves. For the application of offshore floating solar, the wave deformation is negligible as most sea-states consist of waves with frequencies lower than the domain where significant hydroelastic wave deformation occurs. For the application of floating solar on inland waterbodies certain waves are significantly deformed. Although those waves seem small and insignificant compared to ocean waves, hydroelastic wave deformation could potentially play an important factor on the fatigue life of a VFFS.

The influence of the draught of the structure resulted in significant wave shortening in the numerical model. The wavelength deformation corresponded with the theory. However, it was not possible to verify the outcome of the amplitude deformation with an analytical method. Wave shortening is connected with wave focusing in a 3D domain, which can play an important factor for the design of the structure. This only happens if the draught dominates over the stiffness of the structure, as can be seen in Figures 5.6 and 5.7. For stiff structures wave focusing is therefore unlikely to be of any importance. However, for flexible structure this should definitely be taken into account.

9

Recommendations

While building the numerical model and executing the test runs, new questions arose that were not able to be answered within the scope of this research thesis. Therefore, they are discussed below as recommendations for further research.

The numerical model has been built in such a way that it can also calculate the outcome of a 3D domain. Due to limited computer power, it was not possible to run tests with a sufficient high resolution. Also, adaptations need to be made on the Gridap side to overcome the issue of flooding the RAM memory. The three-dimensional model could give answers to 3D effects that were not visible in the 2D model. Wave stretching has an additional 3D effect that it diffracts the wave energy. On the other hand, wave shortening leads to focusing of wave energy. This could result in certain areas under the structure where so much wave energy is trapped that it leads to high amplitudes and possible failure of the VFFS.

Furthermore, the system of equations needs stabilisation parameters to ensure a coercive system. This is necessary as there is yet to be found a norm that satisfies the condition $B(u,u) \geq ||u||$. More research should be carried out to prove if there exists a norm that satisfies this inequality, as a monolithic coercive system is unconditionally stable. Until then, the stabilisation parameters ensure a stable system, but could lead to numerical errors.

The ability to model in 3D also adds the possibility to investigate the response of a VFFS in a confused sea-state, where wind waves are coming from a perpendicular angle than swell, as this is a realistic scenario for offshore locations.

The numerical model was able to capture the effects of large draught scenarios of the structure. Currently, there is no analytical method which covers this regime. Therefore, it is difficult to verify the correctness of the numerical results in this regime. Experimental research with different VFFS densities could be a solution to see if the numerical solution corresponds with the reality.

It was seen that flexible structure with large densities show a wave damping effect as the amplitude of the outgoing wave was lower than the incident wave amplitude. Although this might be a numerical error, it could not be explained that unlike the amplitude, the wavelength deformation returns to its original value. If the numerical results are correct, this opens up an opportunity to investigate the potential of flexible wave dampers. However, more research is necessary to better understand this phenomenon.

A

Numerical test run results

A.1. Test run 1

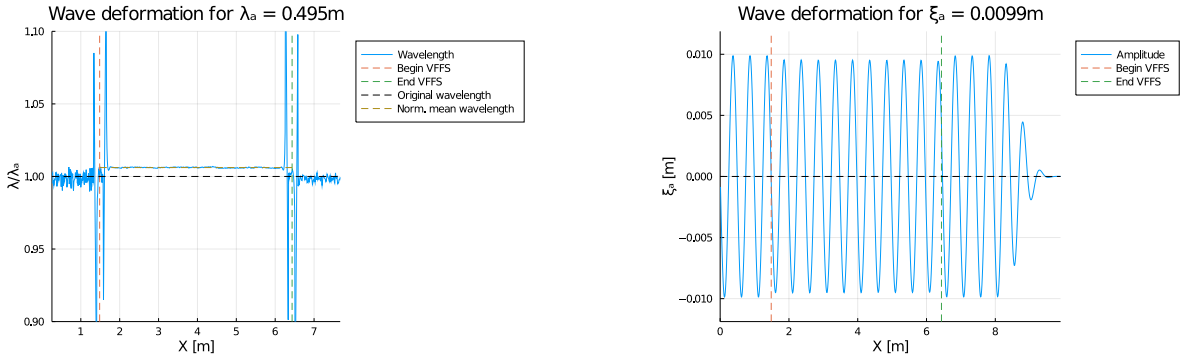

Figure A.1: Wave deformation, wavelength (left) and amplitude (right) for test run 1a.

Dispersion parameter	X_a	X_n	X_{ni}	X_{no}	X_{ri}	X_{ro}	X_b
K [-]	1.007	1.008	-	-	1.010	1.008	-
R [-]	0.965	-	0.964	0.965	0.963	0.963	-
P [J/s]	-	-	0.2148	0.2154	-	-	0.2146

Table A.1: Dispersion parameters for each subscript for test run 1a.

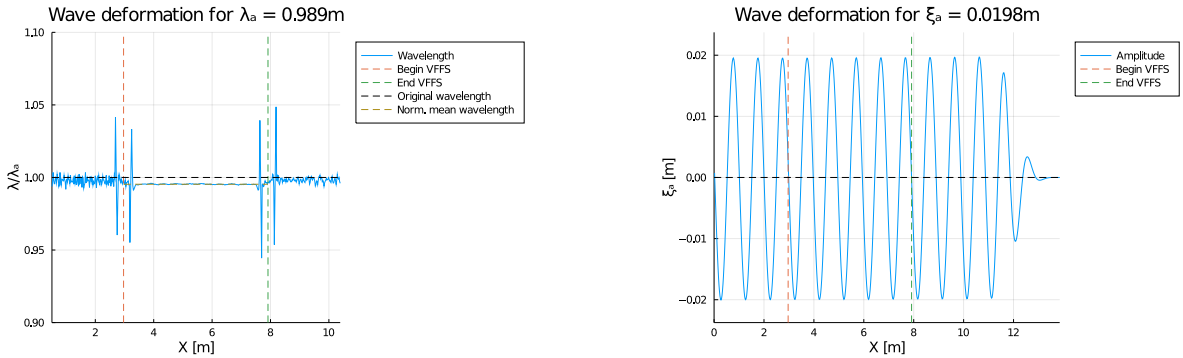

Figure A.2: Wave deformation, wavelength (left) and amplitude (right) for test run 1b.

Dispersion parameter	X_a	X_n	X_{ni}	X_{no}	X_{ri}	X_{ro}	X_b
K [-]	0.997	0.997	-	-	0.998	0.997	-
R [-]	1.001	-	1.001	1.001	1.000	0.993	-
P [J/s]	-	-	1.192	1.209	-	-	1.191

Table A.2: Dispersion parameters for each subscript for test run 1b.

A.2. Test run 2

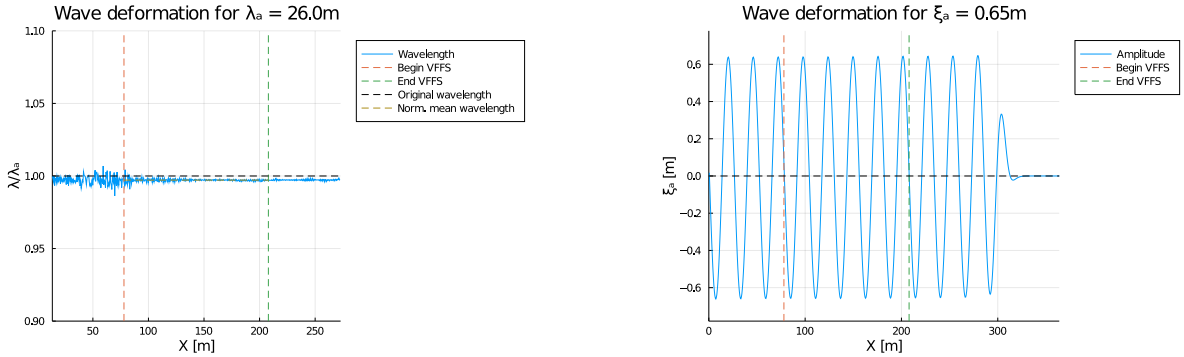

Figure A.3: Wave deformation, wavelength (left) and amplitude (right) for test run 2a.

Dispersion parameter	X_a	X_n	X_{ni}	X_{no}	X_{ri}	X_{ro}	X_b
K [-]	1.000	1.000	-	-	1.000	1.000	-
R [-]	1.000	-	1.000	1.000	1.003	0.991	-
P [J/s]	-	-	6535	6684	-	-	6565

Table A.3: Dispersion parameters for each subscript for test run 2a.

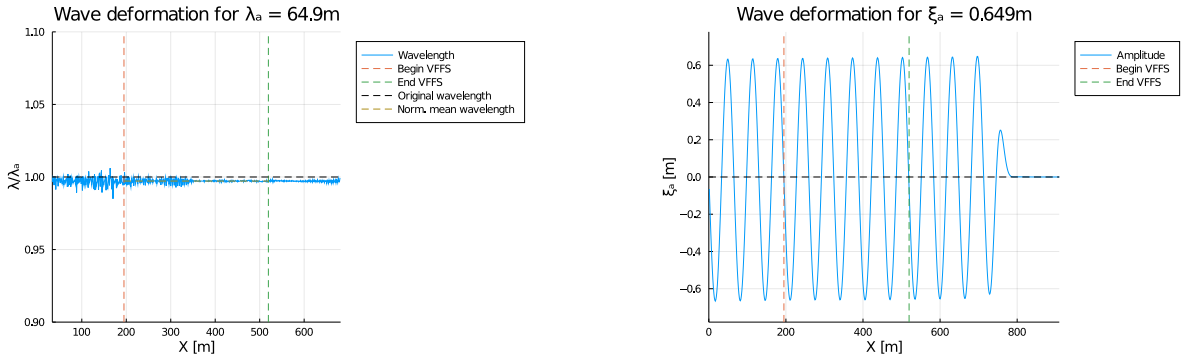

Figure A.4: Wave deformation, wavelength (left) and amplitude (right) for test run 2b.

Dispersion parameter	X_a	X_n	X_{ni}	X_{no}	X_{ri}	X_{ro}	X_b
K [-]	1.000	1.000	-	-	1.000	1.000	-
R [-]	1.000	-	1.000	1.000	1.004	0.986	-
P [J/s]	-	-	1022	1059	-	-	1031

Table A.4: Dispersion parameters for each subscript for test run 2b.

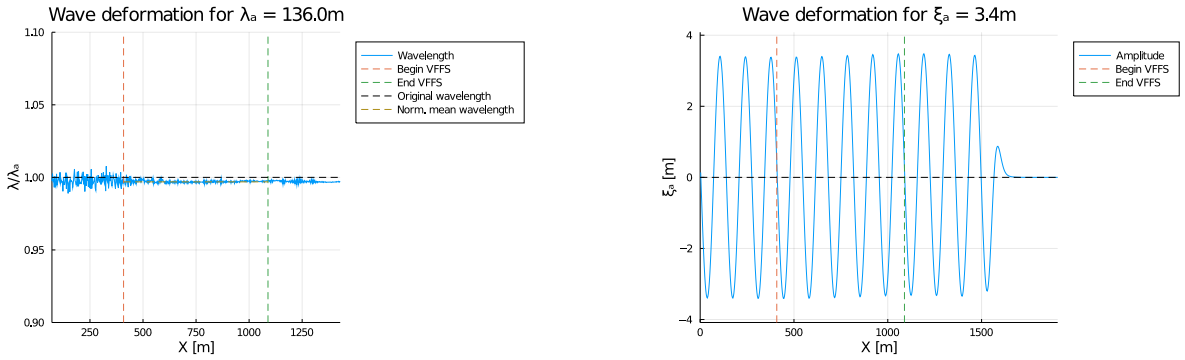

Figure A.5: Wave deformation, wavelength (left) and amplitude (right) for test run 2c.

Dispersion parameter	X_a	X_n	X_{ni}	X_{no}	X_{ri}	X_{ro}	X_b
K [-]	1.000	1.000	-	-	0.999	1.000	-
R [-]	1.000	-	1.001	1.000	1.002	0.986	-
P [J/s]	-	-	4.599×10^5	4.745×10^5	-	-	4.617×10^5

Table A.5: Dispersion parameters for each subscript for test run 2c.

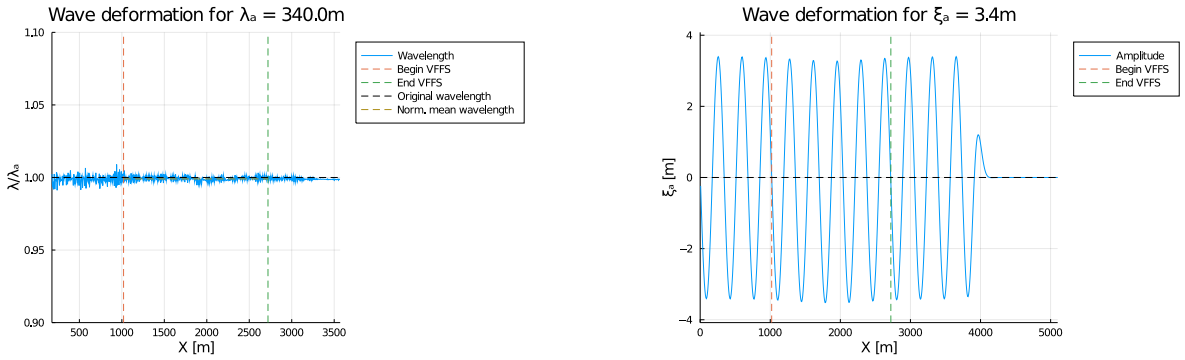

Figure A.6: Wave deformation, wavelength (left) and amplitude (right) for test run 2d.

Dispersion parameter	X_a	X_n	X_{ni}	X_{no}	X_{ri}	X_{ro}	X_b
K [-]	1.000	1.000	-	-	1.000	1.000	-
R [-]	1.000	-	1.000	1.000	0.971	0.971	-
P [J/s]	-	-	9.088×10^5	9.091×10^5	-	-	8.569×10^5

Table A.6: Dispersion parameters for each subscript for test run 2d.

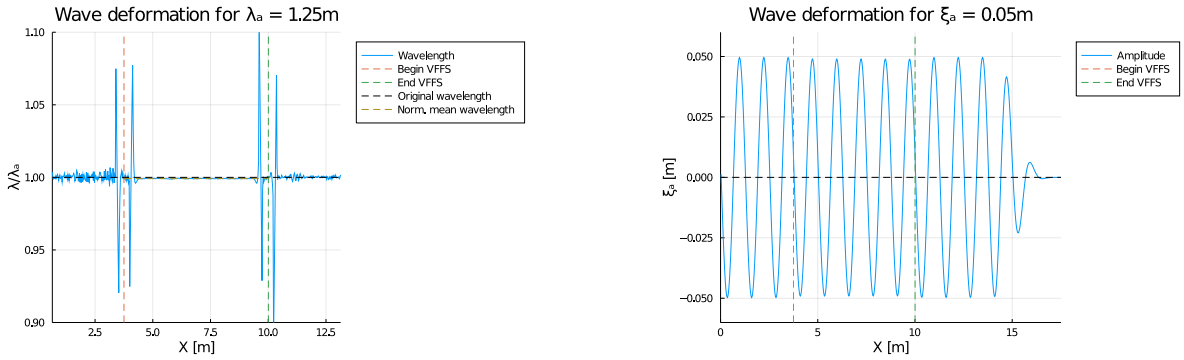

Figure A.7: Wave deformation, wavelength (left) and amplitude (right) for test run 2e.

Dispersion parameter	X_a	X_n	X_{ni}	X_{no}	X_{ri}	X_{ro}	X_b
K [-]	0.999	0.999	-	-	0.999	0.999	-
R [-]	0.989	-	0.989	0.989	0.987	0.988	-
P [J/s]	-	-	8.640	8.627	-	-	8.614

Table A.7: Dispersion parameters for each subscript for test run 2e.

A.3. Test run 3

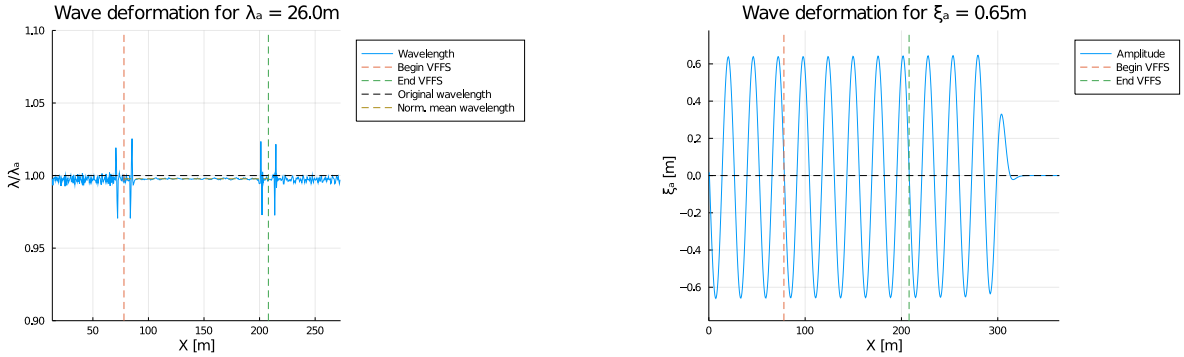

Figure A.8: Wave deformation, wavelength (left) and amplitude (right) for test run 3a.

Dispersion parameter	X_a	X_n	X_{ni}	X_{no}	X_{ri}	X_{ro}	X_b
K [-]	1.000	1.000	-	-	1.001	1.001	-
R [-]	0.999	-	0.999	0.999	1.002	0.990	-
P [J/s]	-	-	6529	6683	-	-	6566

Table A.8: Dispersion parameters for each subscript for test run 3a.

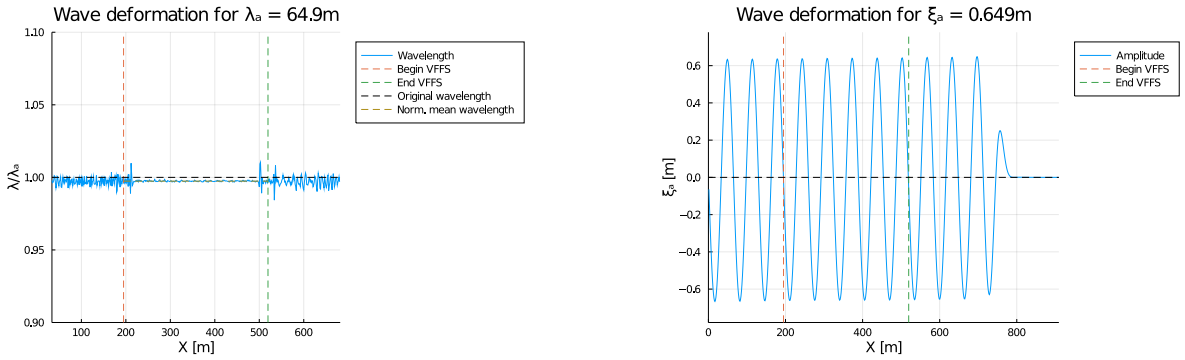

Figure A.9: Wave deformation, wavelength (left) and amplitude (right) for test run 3b.

Dispersion parameter	X_a	X_n	X_{ni}	X_{no}	X_{ri}	X_{ro}	X_b
K [-]	1.000	1.000	-	-	1.000	1.000	-
R [-]	1.000	-	1.000	1.000	1.005	0.986	-
P [J/s]	-	-	1.021×10^4	1.060×10^4	-	-	1031×10^4

Table A.9: Dispersion parameters for each subscript for test run 3b.

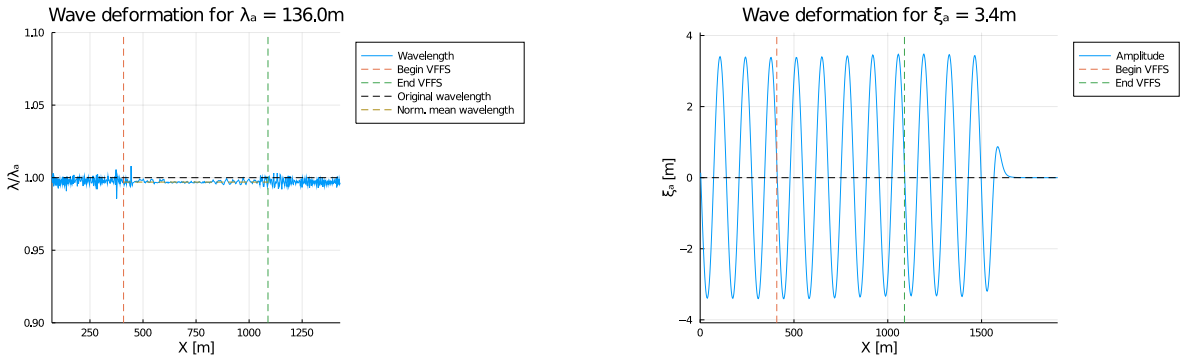

Figure A.10: Wave deformation, wavelength (left) and amplitude (right) for test run 3c.

Dispersion parameter	X_a	X_n	X_{ni}	X_{no}	X_{ri}	X_{ro}	X_b
K [-]	1.000	1.000	-	-	0.999	1.000	-
R [-]	1.000	-	1.000	1.000	1.003	0.986	-
P [J/s]	-	-	4.592×10^5	4.745×10^5	-	-	4.617×10^5

Table A.10: Dispersion parameters for each subscript for test run 3c.

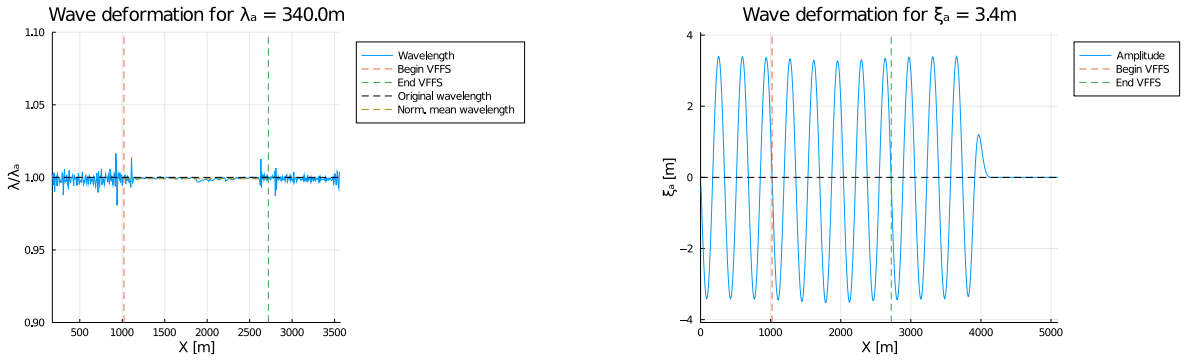

Figure A.11: Wave deformation, wavelength (left) and amplitude (right) for test run 3d.

Dispersion parameter	X_a	X_n	X_{ni}	X_{no}	X_{ri}	X_{ro}	X_b
K [-]	1.000	1.000	-	-	1.000	1.000	-
R [-]	1.000	-	1.000	1.000	0.970	0.969	-
P [J/s]	-	-	9.092×10^5	9.115×10^5	-	-	8.569×10^5

Table A.11: Dispersion parameters for each subscript for test run 3d.

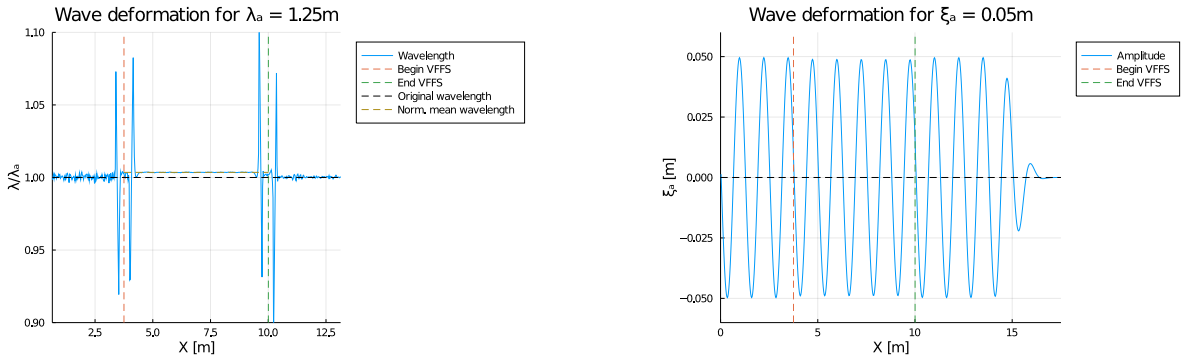

Figure A.12: Wave deformation, wavelength (left) and amplitude (right) for test run 3e.

Dispersion parameter	X_a	X_n	X_{ni}	X_{no}	X_{ri}	X_{ro}	X_b
K [-]	1.003	1.003	-	-	1.004	1.003	-
R [-]	0.985	-	0.984	0.985	0.984	0.985	-
P [J/s]	-	-	8.645	8.630	-	-	8.634

Table A.12: Dispersion parameters for each subscript for test run 3e.

A.4. Test run 4

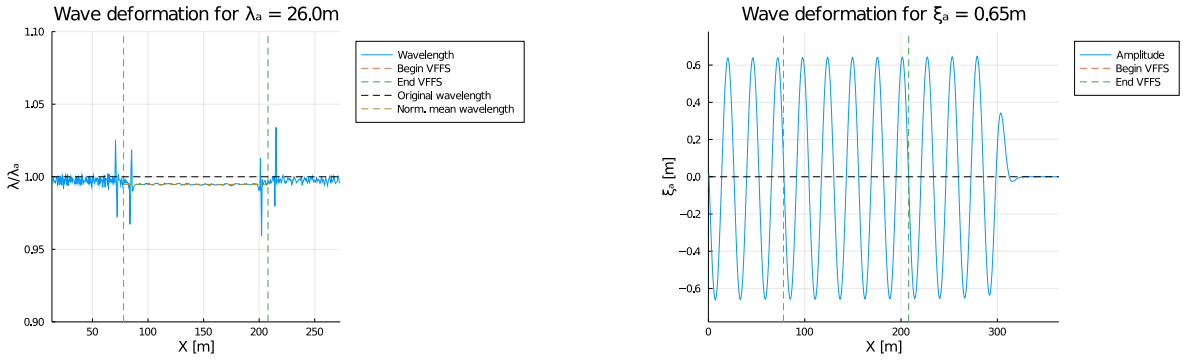

Figure A.13: Wave deformation, wavelength (left) and amplitude (right) for test run 4a.

Dispersion parameter	X_a	X_n	X_{ni}	X_{no}	X_{ri}	X_{ro}	X_b
K [-]	0.997	0.997	-	-	0.997	0.997	-
R [-]	1.002	-	1.002	1.002	1.003	0.990	-
P [J/s]	-	-	6532	6705	-	-	6547

Table A.13: Dispersion parameters for each subscript for test run 4a.

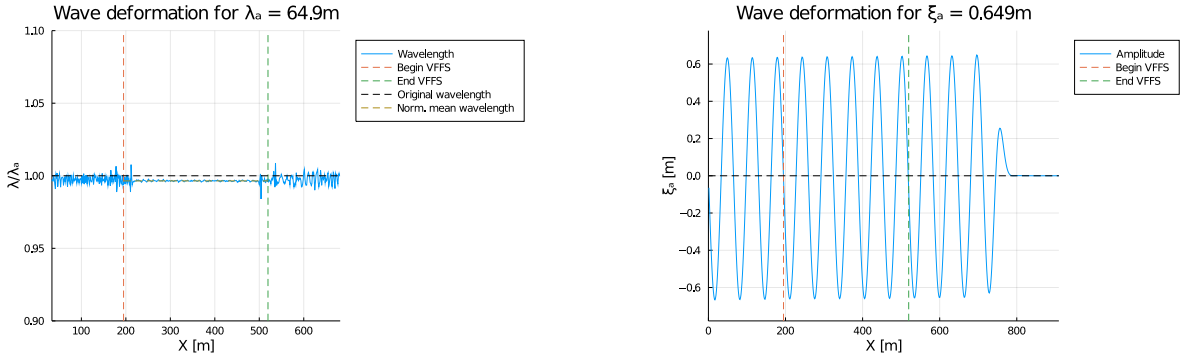

Figure A.14: Wave deformation, wavelength (left) and amplitude (right) for test run 4b.

Dispersion parameter	X_a	X_n	X_{ni}	X_{no}	X_{ri}	X_{ro}	X_b
K [-]	0.999	0.999	-	-	0.999	0.999	-
R [-]	1.001	-	1.001	1.001	1.005	0.985	-
P [J/s]	-	-	1.021×10^4	1064×10^4	-	-	1.030×10^4

Table A.14: Dispersion parameters for each subscript for test run 4b.

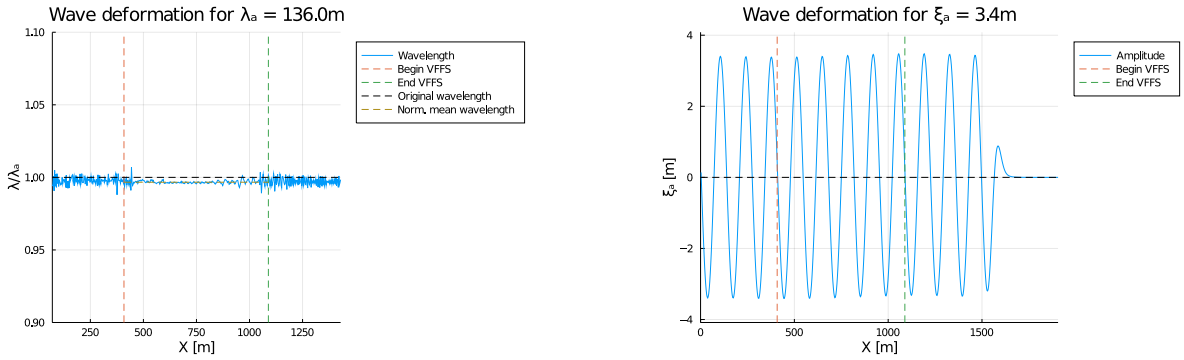

Figure A.15: Wave deformation, wavelength (left) and amplitude (right) for test run 4c.

Dispersion parameter	X_a	X_n	X_{ni}	X_{no}	X_{ri}	X_{ro}	X_b
K [-]	1.000	1.000	-	-	0.999	1.000	-
R [-]	1.000	-	1.001	1.000	1.003	0.988	-
P [J/s]	-	-	4.597×10^5	4.737×10^5	-	-	4.618×10^5

Table A.15: Dispersion parameters for each subscript for test run 4c.

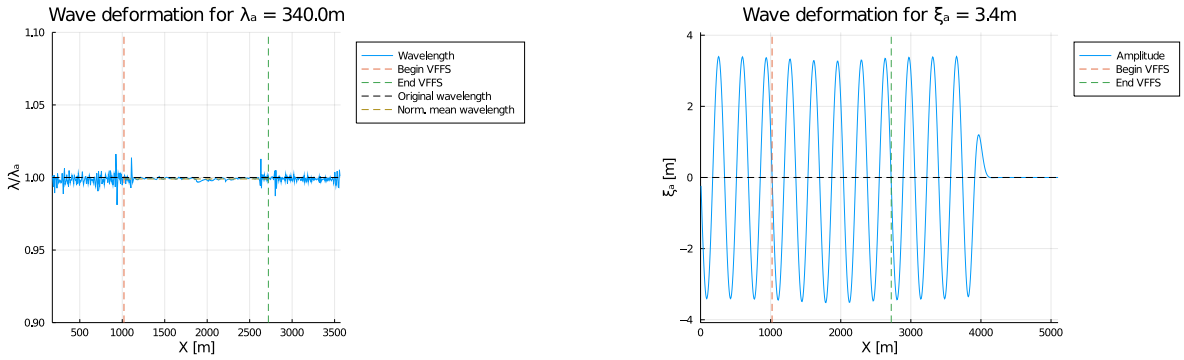

Figure A.16: Wave deformation, wavelength (left) and amplitude (right) for test run 4d.

Dispersion parameter	X_a	X_n	X_{ni}	X_{no}	X_{ri}	X_{ro}	X_b
K [-]	1.000	1.000	-	-	1.000	1.000	-
R [-]	1.000	-	1.000	1.000	0.970	0.970	-
P [J/s]	-	-	9.092×10^5	9.111×10^5	-	-	8.569×10^5

Table A.16: Dispersion parameters for each subscript for test run 4d.

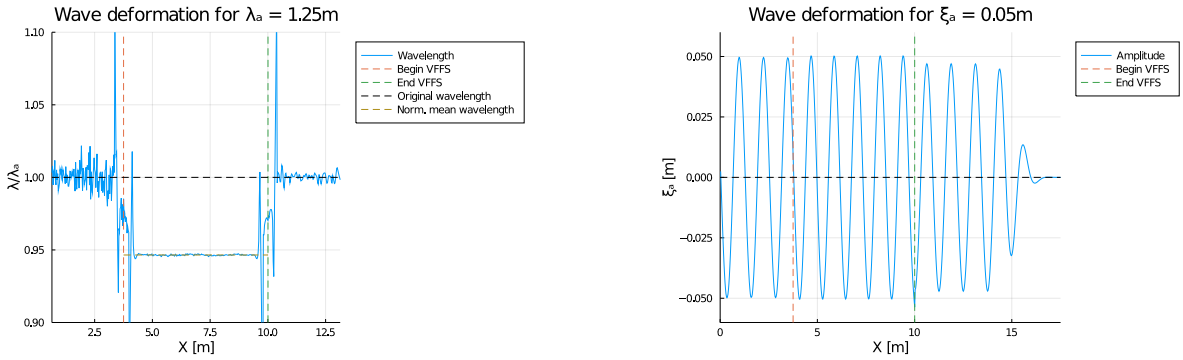

Figure A.17: Wave deformation, wavelength (left) and amplitude (right) for test run 4e.

Dispersion parameter	X_a	X_n	X_{ni}	X_{no}	X_{ri}	X_{ro}	X_b
K [-]	0.946	0.946	-	-	0.948	0.946	-
R [-]	1.040	-	1.039	1.039	1.011	1.066	-
P [J/s]	-	-	8.604	7.744	-	-	8.140

Table A.17: Dispersion parameters for each subscript for test run 4e.

A.5. Test run 5

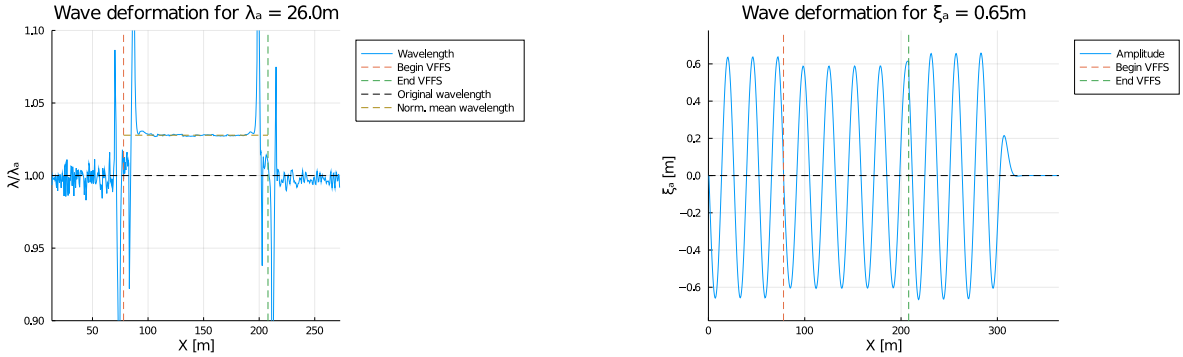

Figure A.18: Wave deformation, wavelength (left) and amplitude (right) for test run 5a.

Dispersion parameter	X_a	X_n	X_{ni}	X_{no}	X_{ri}	X_{ro}	X_b
K [-]	1.030	1.030	-	-	1.034	1.031	-
R [-]	0.918	-	0.916	0.918	0.920	0.896	-
P [J/s]	-	-	6515	6901	-	-	6573

Table A.18: Dispersion parameters for each subscript for test run 5a.

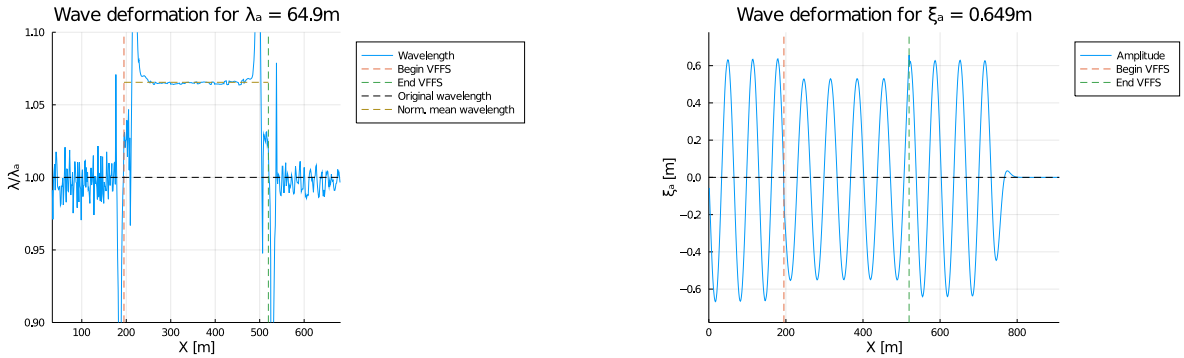

Figure A.19: Wave deformation, wavelength (left) and amplitude (right) for test run 5b.

Dispersion parameter	X_a	X_n	X_{ni}	X_{no}	X_{ri}	X_{ro}	X_b
K [-]	1.067	1.068	-	-	1.076	1.069	-
R [-]	0.837	-	0.833	0.836	0.832	0.843	-
P [J/s]	-	-	1.016×10^4	9973	-	-	1.013×10^4

Table A.19: Dispersion parameters for each subscript for test run 5b.

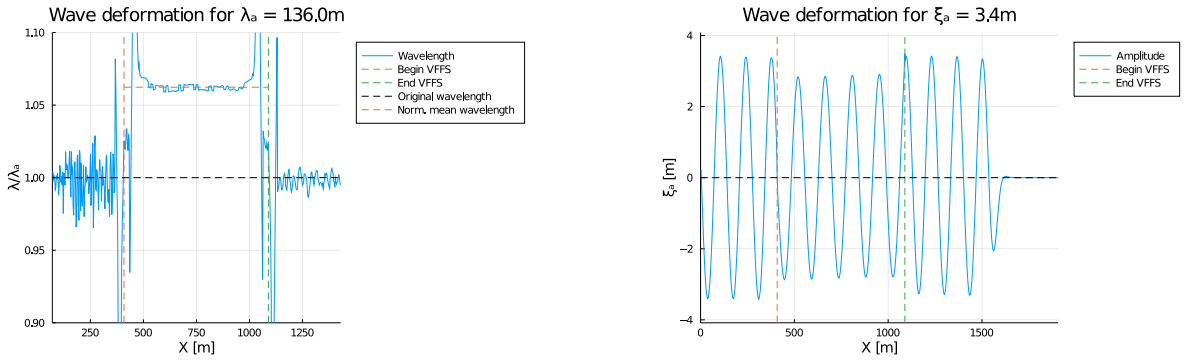

Figure A.20: Wave deformation, wavelength (left) and amplitude (right) for test run 5c.

Dispersion parameter	X_a	X_n	X_{ni}	X_{no}	X_{ri}	X_{ro}	X_b
K [-]	1.070	1.071	-	-	1.071	1.064	-
R [-]	0.834	-	0.829	0.833	0.833	0.834	-
P [J/s]	-	-	4.572×10^5	4.605×10^5	-	-	4.605×10^5

Table A.20: Dispersion parameters for each subscript for test run 5c.

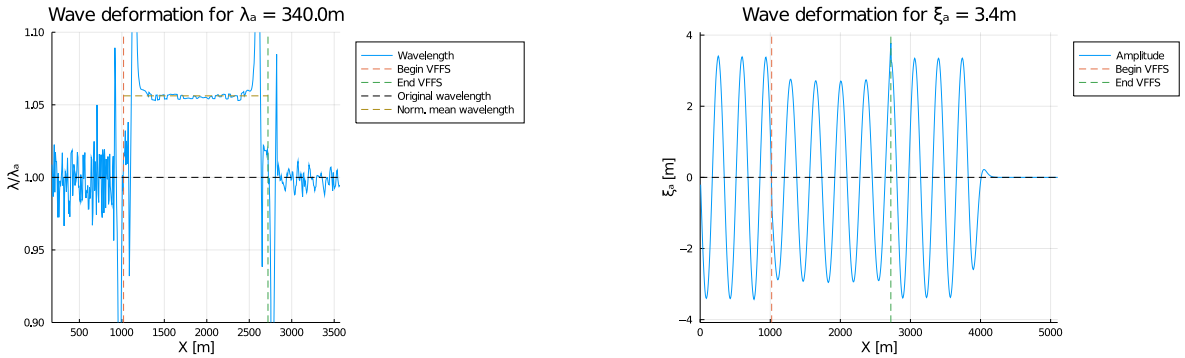

Figure A.21: Wave deformation, wavelength (left) and amplitude (right) for test run 5d.

Dispersion parameter	X_a	X_n	X_{ni}	X_{no}	X_{ri}	X_{ro}	X_b
K [-]	1.093	1.093	-	-	1.066	1.058	-
R [-]	0.838	-	0.833	0.837	0.801	0.815	-
P [J/s]	-	-	9.062×10^5	8.850×10^5	-	-	8.379×10^5

Table A.21: Dispersion parameters for each subscript for test run 5d.

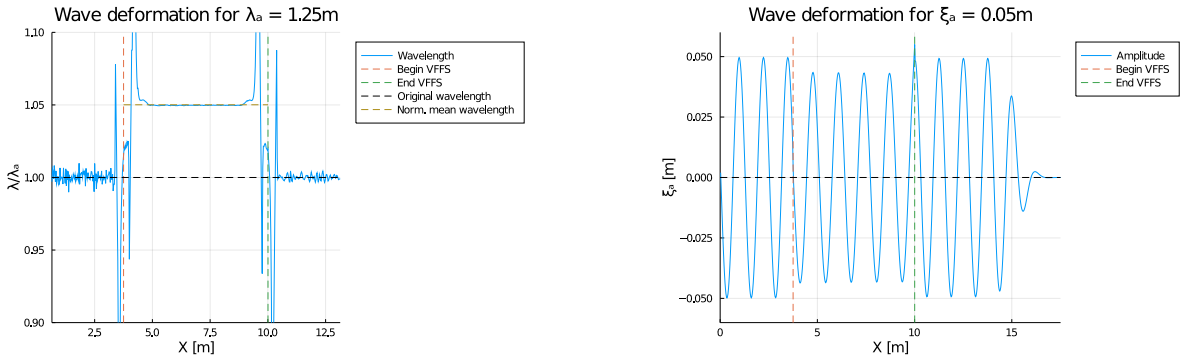

Figure A.22: Wave deformation, wavelength (left) and amplitude (right) for test run 5e.

Dispersion parameter	X_a	X_n	X_{ni}	X_{no}	X_{ri}	X_{ro}	X_b
K [-]	1.049	1.049	-	-	1.055	1.050	-
R [-]	0.870	-	0.868	0.870	0.867	0.873	-
P [J/s]	-	-	8.595	8.513	-	-	8.566

Table A.22: Dispersion parameters for each subscript for test run 5e.

A.6. Test run 6

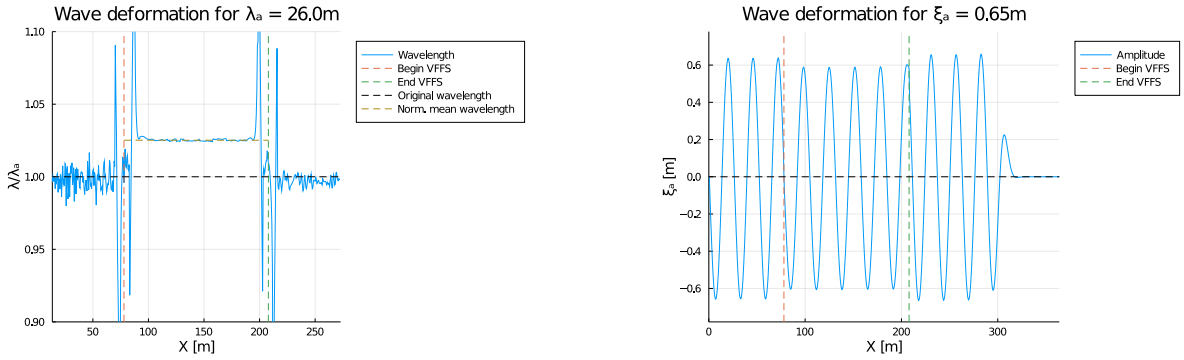

Figure A.23: Wave deformation, wavelength (left) and amplitude (right) for test run 6a.

Dispersion parameter	X_a	X_n	X_{ni}	X_{no}	X_{ri}	X_{ro}	X_b
K [-]	1.027	1.028	-	-	1.031	1.028	-
R [-]	0.920	-	0.918	0.919	0.921	0.896	-
P [J/s]	-	-	6524	6905	-	-	6561

Table A.23: Dispersion parameters for each subscript for test run 6a.

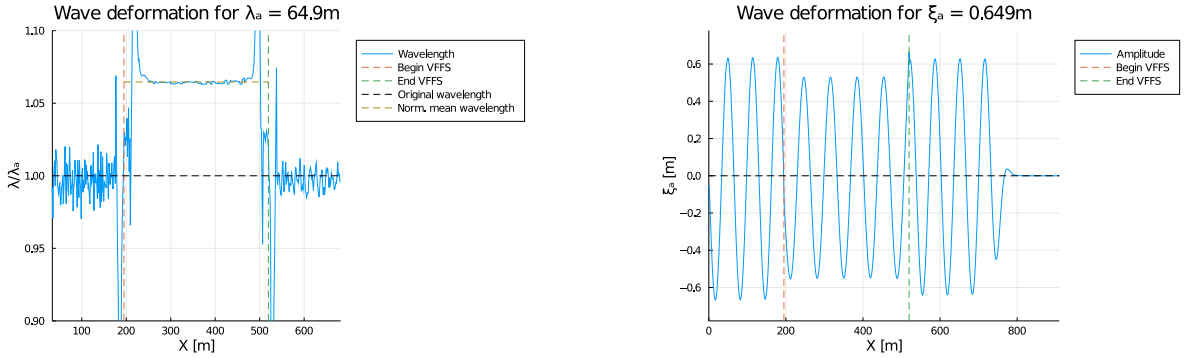

Figure A.24: Wave deformation, wavelength (left) and amplitude (right) for test run 6b.

Dispersion parameter	X_a	X_n	X_{ni}	X_{no}	X_{ri}	X_{ro}	X_b
K [-]	1.066	1.067	-	-	1.076	1.068	-
R [-]	0.837	-	0.833	0.836	0.832	0.843	-
P [J/s]	-	-	1.016×10^4	9961	-	-	1.013×10^4

Table A.24: Dispersion parameters for each subscript for test run 6b.

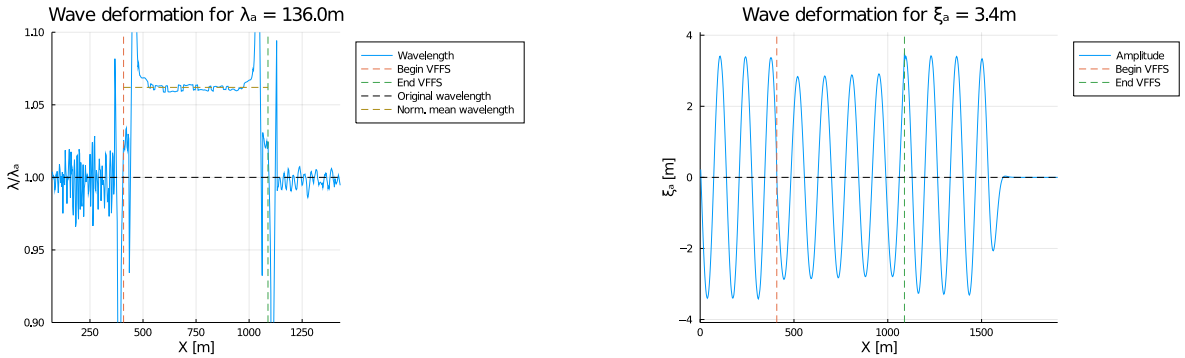

Figure A.25: Wave deformation, wavelength (left) and amplitude (right) for test run 6c.

Dispersion parameter	X_a	X_n	X_{ni}	X_{no}	X_{ri}	X_{ro}	X_b
K [-]	1.070	1.070	-	-	1.071	1.063	-
R [-]	0.834	-	0.830	0.834	0.833	0.833	-
P [J/s]	-	-	4.571×10^5	4.609×10^5	-	-	4.603×10^5

Table A.25: Dispersion parameters for each subscript for test run 6c.

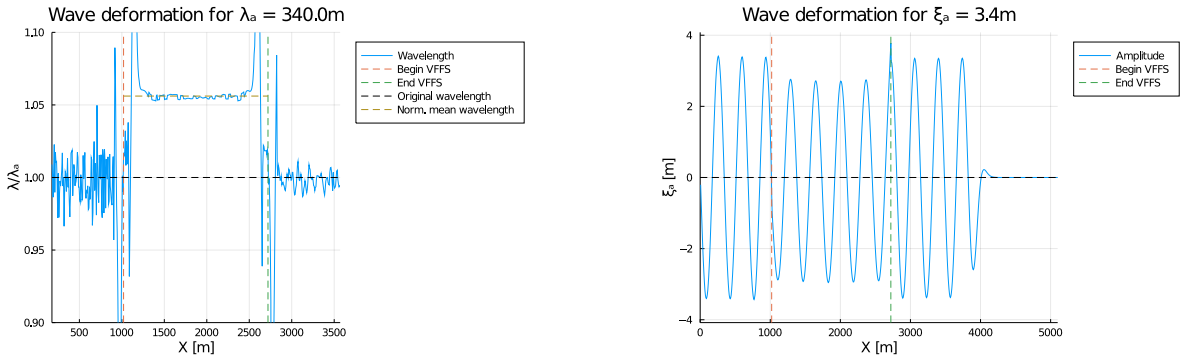

Figure A.26: Wave deformation, wavelength (left) and amplitude (right) for test run 6d.

Dispersion parameter	X_a	X_n	X_{ni}	X_{no}	X_{ri}	X_{ro}	X_b
K [-]	1.093	1.093	-	-	1.066	1.058	-
R [-]	0.838	-	0.833	0.837	0.801	0.815	-
P [J/s]	-	-	9.066×10^5	8.847×10^5	-	-	8.378×10^5

Table A.26: Dispersion parameters for each subscript for test run 6d.

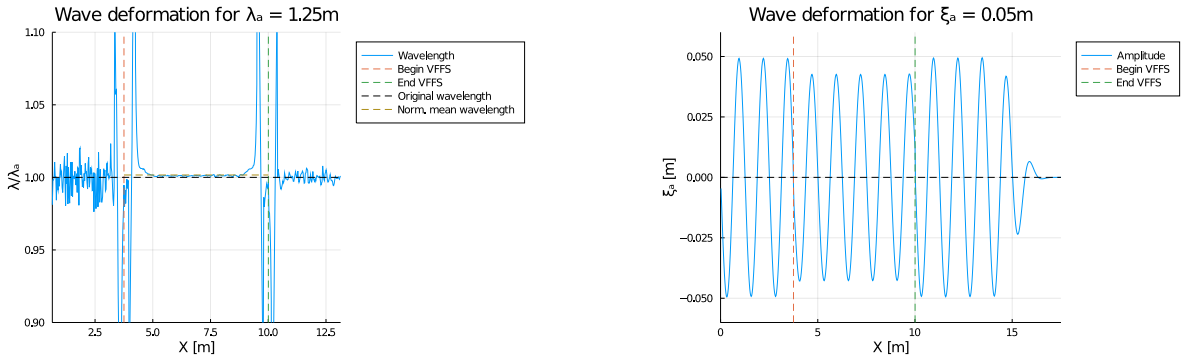

Figure A.27: Wave deformation, wavelength (left) and amplitude (right) for test run 6e.

Dispersion parameter	X_a	X_n	X_{ni}	X_{no}	X_{ri}	X_{ro}	X_b
K [-]	1.001	1.001	-	-	1.010	1.002	-
R [-]	0.893	-	0.889	0.893	0.861	0.869	-
P [J/s]	-	-	8.690	8.603	-	-	8.146

Table A.27: Dispersion parameters for each subscript for test run 6e.

A.7. Test run 7

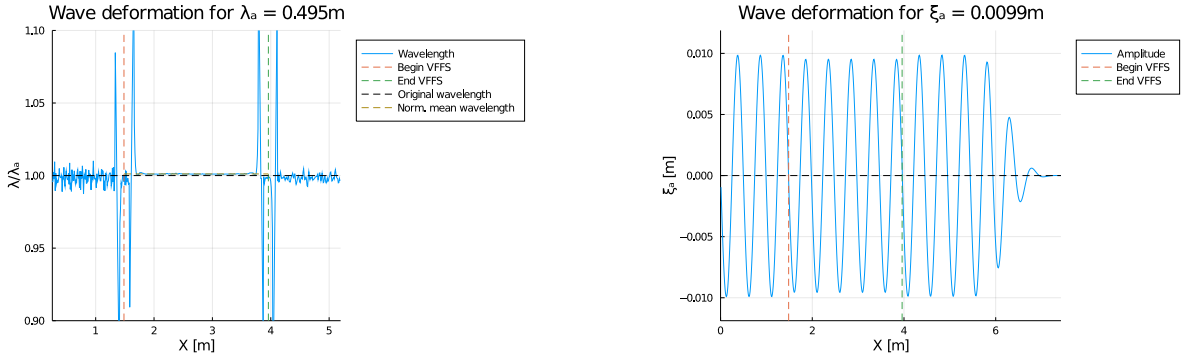

Figure A.28: Wave deformation, wavelength (left) and amplitude (right) for test run 7a.

Dispersion parameter	X_a	X_n	X_{ni}	X_{no}	X_{ri}	X_{ro}	X_b
K [-]	1.003	1.003	-	-	1.005	1.003	-
R [-]	0.969	-	0.968	0.969	0.966	0.965	-
P [J/s]	-	-	0.2134	0.2143	-	-	0.2127

Table A.28: Dispersion parameters for each subscript for test run 7a.

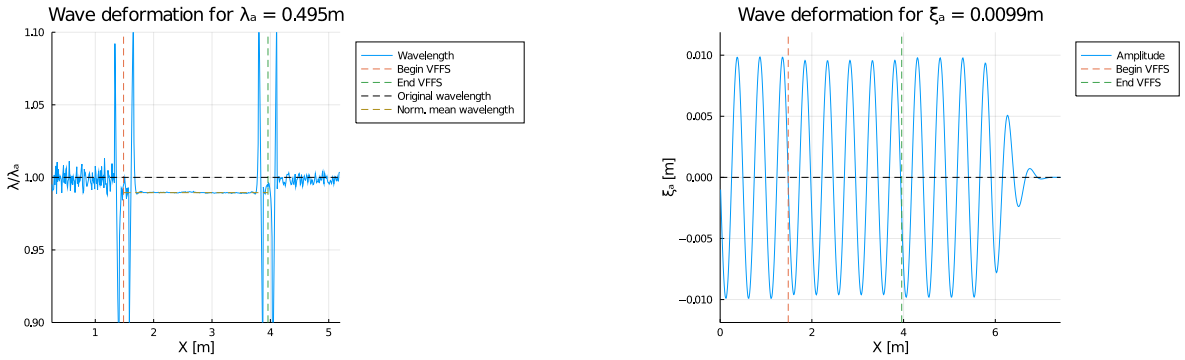

Figure A.29: Wave deformation, wavelength (left) and amplitude (right) for test run 7b.

Dispersion parameter	X_a	X_n	X_{ni}	X_{no}	X_{ri}	X_{ro}	X_b
K [-]	0.991	0.991	-	-	0.993	0.991	-
R [-]	0.979	-	0.977	0.979	0.970	0.977	-
P [J/s]	-	-	0.2136	0.2110	-	-	0.2103

Table A.29: Dispersion parameters for each subscript for test run 7b.

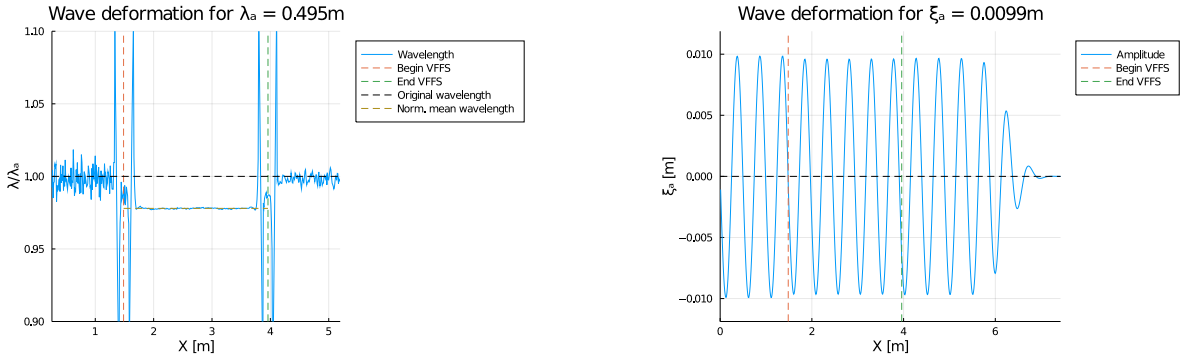

Figure A.30: Wave deformation, wavelength (left) and amplitude (right) for test run 7c.

Dispersion parameter	X_a	X_n	X_{ni}	X_{no}	X_{ri}	X_{ro}	X_b
K [-]	0.979	0.979	-	-	0.983	0.980	-
R [-]	0.989	-	0.987	0.988	0.975	0.994	-
P [J/s]	-	-	0.2128	0.2056	-	-	0.2078

Table A.30: Dispersion parameters for each subscript for test run 7c.

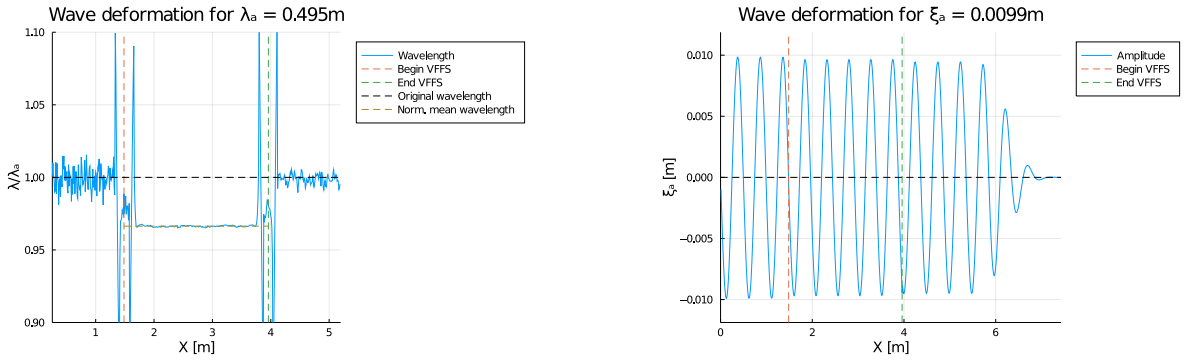

Figure A.31: Wave deformation, wavelength (left) and amplitude (right) for test run 7d.

Dispersion parameter	X_a	X_n	X_{ni}	X_{no}	X_{ri}	X_{ro}	X_b
K [-]	0.968	0.968	-	-	0.971	0.968	-
R [-]	0.998	-	0.997	0.998	0.978	1.019	-
P [J/s]	-	-	0.2131	0.1968	-	-	0.2053

Table A.31: Dispersion parameters for each subscript for test run 7d.

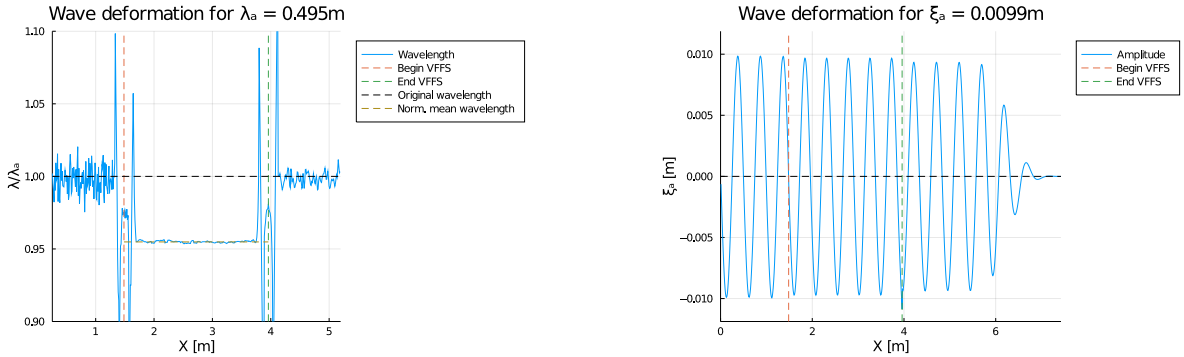

Figure A.32: Wave deformation, wavelength (left) and amplitude (right) for test run 7e.

Dispersion parameter	X_a	X_n	X_{ni}	X_{no}	X_{ri}	X_{ro}	X_b
K [-]	0.956	0.956	-	-	0.961	0.956	-
R [-]	1.008	-	1.006	1.008	0.982	1.036	-
P [J/s]	-	-	0.2126	0.1922	-	-	0.2028

Table A.32: Dispersion parameters for each subscript for test run 7e.

B

Tutorial

Very Flexible Floating Structure (VFFS)

This tutorial shows how a Fluid Structure Interaction (FSI) in a 2D domain is modelled. Potential flow is used to model the fluid and on top a Dynamic Euler-Bernoulli beam is located that serves as the floating structure. Below you find a picture of a 3D FSI model, however, as this is highly computational intensive, this tutorial will focus on a two-dimensional domain. Feel free to play with the code and try to make a 3D model!

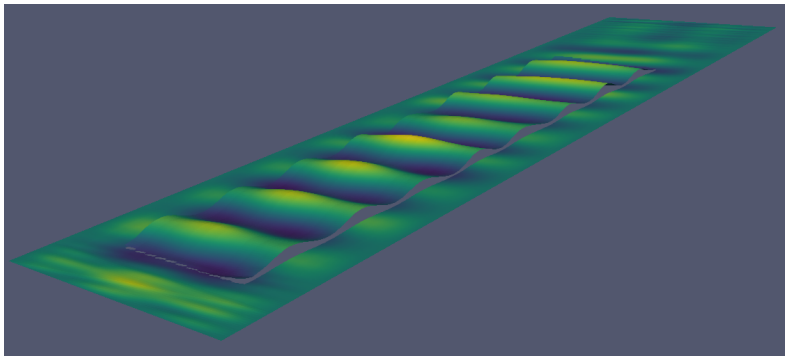

3D model

Mathematics

First of all, let's dive in to the mathematics behind the problem. Potential flow is based on the principle that the velocity field can be described by the spatial derivatives of a scalar function, this is called the potential function. Moreover, the fluid is considered to be incompressible. This consideration implies that the divergence of the velocity is equal to zero. The potential function then satisfies the Laplace equation:

$$\begin{cases} \nabla \cdot \vec{u} = 0 \\ \nabla \phi = \vec{u} \end{cases} \Leftrightarrow \nabla \cdot (\nabla \phi) = \Delta \phi = 0 \quad \text{in} \quad \Omega$$

Where Ω denotes the 2D domain.

Now it is time to set the boundary conditions of the domain. In this case, three different boundaries need to be applied:

- The bottom boundary
- The free surface boundary
- The structure boundary

Bottom boundary

The bottom boundary (also called the sea bed boundary) states that the boundary is impermeable and given as:

$$\nabla \phi \cdot \vec{n} = 0 \quad \text{on} \quad \Gamma_L \cup \Gamma_{btm} \cup \Gamma_R \quad \text{bottom b.c.}$$

In this model, not only the bottom of the domain (Γ_{btm}) is impermeable, but also the left (Γ_L) and right (Γ_R) hand side of the domain (see figure below).

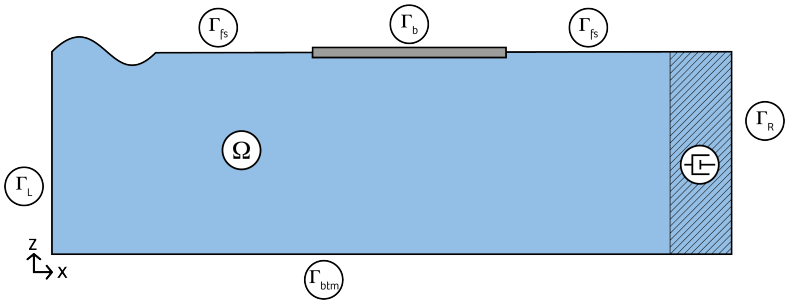

The top boundary, however, is not impermeable, but is the free surface boundary (Γ_{fs}). The fluid is able to move freely up and down, but mustn't leave the domain. Two conditions need to be applied here:

- The dynamic boundary condition
- The kinematic boundary condition

Dynamic boundary condition

The dynamic free surface boundary condition states that the pressure above the free surface is constant and equal to zero. Using Bernoulli's equation in the linearised form and assuming that there is no y-direction (since the model is only 2D), the boundary condition is given as:

$$\frac{\delta\phi}{\delta t} + g\eta = 0 \quad \text{on} \quad \Gamma_{fs} \quad \text{dynamic free surface b.c.}$$

Where g is the gravity constant and η is the surface elevation. With this boundary condition the formula of the potential flow can be derived and is equal to:

$$\phi = \frac{\xi_i g}{\omega} \cdot \frac{\cosh(k_i(d+z))}{\cosh(k_i d)} \cdot \sin(k_i x - \omega t)$$

Where ξ_i , ω and k_i are the amplitude, the angular frequency and the wave number of the incident wave, respectively and d the water depth.

Kinematic boundary condition

Finally, the third boundary condition is the kinematic free surface boundary condition which describes that the vertical velocity of the free surface has to be equal to the vertical motion of the flow and is given as follows:

$$\frac{\delta\phi}{\delta z} = \frac{\delta\eta}{\delta t} \quad \text{on} \quad \Gamma_{fs} \quad \text{kinematic free surface b.c.}$$

Cauchy-Poisson condition

Using this boundary condition the wave number can be related to the wave frequency. By differentiating the dynamic free surface boundary condition and inserting the kinematic free surface boundary condition one obtains the Cauchy-Poisson condition:

$$\frac{\delta\phi}{\delta z} + \frac{1}{g}\frac{\delta^2\phi}{\delta t^2} = 0$$

Substituting the potential function into the Cauchy-Poisson equation gives the dispersion relation:

$$\omega^2 = gk_i \tanh(k_i d)$$

Using these equation, one is able to establish the free surface and the fluid domain can be modelled. However, we are interested in a fluid structure interaction, which means that there should also be a boundary condition at the location of the floating structure (Γ_b). This is done by imposing the Dynamic Euler-Bernoulli beam on a slice of the free surface.

Dynamic Euler-Bernoulli beam

The dynamic Euler-Bernoulli beam is a one-dimensional equation that is valid if the loads are purely lateral and the deflections remain small. The general form of the Euler-Bernoulli beam describes a relation of the deflection of the beam (w) and an external force ($f(t)$) as function of time:

$$EI\frac{\delta^4 w}{\delta x^4} = -\mu\frac{\delta^2 w}{\delta t^2} + f(x)$$

Where EI is the bending stiffness and μ is the mass per unit length.

Regarding the boundary conditions, the kinematic b.c. remains the same as for the free surface. However, the dynamic boundary condition changes to a non-zero solution and is multiplied by the fluid density ρ_w:

$$-\rho_w \frac{\delta \phi}{\delta t} - \rho_w g\eta = p$$

The pressure p is equal to the external force of the Euler-Bernoulli beam:

$$p = \rho_b h\frac{\delta^2 \eta}{\delta t^2} + \frac{EI}{B}\frac{\delta^4 \eta}{\delta x^4}$$

Where μ is equal to the product of the structure density ρ_b and the thickness of the structure h. The bending stiffness has been divided by the width (B) of the structure, as the model is only two-dimensional and the deflection w has been replaced by the surface elevation η. Rewriting this into one equation results in the altered dynamic boundary condition:

$$\rho_b h\frac{\delta^2 \eta}{\delta t^2} + \frac{EI}{B}\frac{\delta^4 \eta}{\delta x^4} + \rho_w \frac{\delta \phi}{\delta t} + \rho_w g\eta = 0 \quad \text{on} \quad \Gamma_b$$

Rewriting this equation and inserting the same governing kinematic free surface boundary condition results in an altered Cauchy-Poisson condition with an added factor; three terms in between brackets:

$$\left(\frac{\rho_b h}{\rho_w g}\frac{\delta^2 \eta}{\delta t^2} + \frac{EI}{\rho_w g B}\frac{\delta^4 \eta}{\delta x^4} + 1\right) g\frac{\delta \phi}{\delta z} = -\frac{\delta^2 \phi}{\delta t^2}$$

Assuming that the solution of the free surface elevation is wave:

$$\eta = \xi_b \cos\left(k_b x - \omega t\right)$$

With ξ_b and k_b the amplitude and the wave number of the hydroelastic wave, respectively. Its second derivative in time and fourth derivative in space are given as:

$$\eta_{tt} = -\omega^2 \xi_b \cos(k_b x - \omega t)$$
$$\eta_{xxxx} = k_b^4 \xi_b \cos(k_b x - \omega t)$$

Inserting these wave terms and assuming initial conditions ($x = 0, t = 0$) the equation is given as:

$$\left(-\frac{\omega^2 \rho_b h}{\rho_w g} + \frac{k_b^4 EI}{\rho_w g B} + 1\right) g \frac{\delta \phi}{\delta z} = -\frac{\delta^2 \phi}{\delta t^2}$$

Damping zone

At the end of the domain the wave energy should be dissipated to prevent wave reflection. This is done by adding a viscosity term to the set of equations. There are several ways to achieve this, but the most effective way is to use a method by Kim Woo Min who changed the kinematic boundary condition by adding two terms which dissipate the wave energy:

$$\frac{\delta \eta}{\delta t} - \frac{\delta \phi}{\delta z} + \mu_1 \eta + \frac{\mu_2}{g} \phi = 0 \quad \text{kinematic b.c. damping zone}$$

Where μ_1 and μ_2 are damping coefficients that follow from the iteratively chosen μ_0, and are dependent on each other to ensure that no dispersion occurs:

$$\mu_1(x) = \mu_0 \left[1 - \cos\left(\frac{\pi}{2}\left(\frac{x - x_d}{L_d}\right)\right)\right]$$
$$\mu_2 = -\frac{\mu_1^2}{4}$$

Where x_d is starting point of the numerical damping zone and L_d is the length of the damping zone.

Numerical model

As the mathematics behind the model have been shown, it is now time to rewrite the system of equations into the weak formulation and insert them into the numerical model. However, in order to do so, we should first set up the numrical model.

Wave parameters

Let's start with initiating a simple regular wave with a period of $T = 0.5$ s and a steepness of 1/25 with a water depth of $d = 1$ m. Using the just derived Airy wave theory, the wave parameters can be calculated. The module `Roots` is used to calculate the root of the function.

```
using Roots
T = 0.5
steepness = 1/25
d = 1

ω = 2*π / T                 # angular frequency
g = 9.81                    # gravity constant
f(k) = √(g*k*tanh(k*d)) - ω
k = abs(find_zero(f, 0.5))  # wave number
λ = 2*π / k                 # wavelength
ξ = λ * steepness / 2       # wave amplitude
```

Material parameters

Next to the wave parameters, the structure also contains several properties, such as a stiffness, a thickness and a density. The fluid density has been set equal to the sea and the VFFS is made of a 0.005 m rubber-like material called Neoprene, which is very flexible. The width of the structure has not been taken into account and it is assumed that the cross-section is a rectangle.

```
ρ_w = 1025    # fluid density
ρ_b = 116     # structure density
E = 560e3     # Young's modulus
h = 0.005     # thickness
I = h^3 / 12  # moment of inertia
EI = E * I    # bending stiffness
```

For 3D applications the bending stiffness EI should be replaced by the flexural rigidity D and can be calculated as follows:

$$D = \frac{Eh^3}{12(1-\nu^2)}$$

Where ν is the Poisson's ratio.

```
ν = 0.4
D = E * h^3 / (12 * (1-ν^2) )
```

However, this tutorial will focus on a 2D domain, so this will be discarded.

Domain

The domain of the model is defined such that the free surface waves can develop and travel a few wavelengths before they reach the structure. The structure must be longer than the incident wavelength in order to be assumed a VFFS. Finally, the waves will leave the structure and are free surface waves again. Before the waves reach the end of the domain the wave energy should be dissipated to prevent wave reflection at the right hand side of the domain (Γ_R) The picture below shows the set-up of the model.

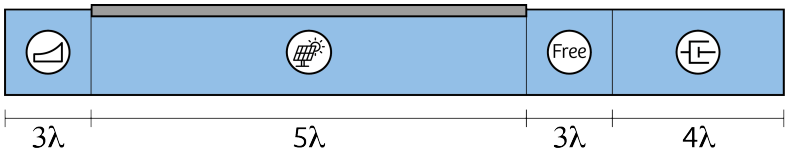

To define the domain the `Gridap` module is used and the different zones are specified:

```
using Gridap
using Gridap.Geometry
using GridapODEs
using GridapODEs.TransientFETools
using GridapODEs.ODETools
```

```
Li = 3*λ # length of incident wave zone
Lb = 5*λ # length of VFFS
Lo = 3*λ # length of outgoing wave zone
Ld = 4*λ # length of damping zone

xb₀ = Li        # x-coordinate start VFFS
xb₁ = Li + Lb   # x-coordinate end VFFS
x₂ = xb₁ + Lo   # x-coordinate start damping zone
x₃ = x₂ + Ld    # end of domain

Xmin = 0
Xmax = x₃
Zmin = 0
Zmax = d

domain = (Xmin, Xmax, Zmin, Zmax)
```

Damping zone

With these values the formula for the damping zone can be established. It is chosen to use a value of $\mu_0 = 10$:

```
μ₀ = 10
μ₁(x::VectorValue) = μ₀*(1.0 - cos(π/2*(x[1]-x₂)/Ld)) * (x[1]>x₂)
μ₂(x::VectorValue) = -(μ₁(x::VectorValue)^2)/4 * (x[1]>x₂)
```

Resolution

To define the resolution of the domain a partition is given. This is the amount of grid cells that the model contains. The resolution in the x-direction should be high, as we are interested in the exact shape of the wave. For the z-direction, however, we are only interested in the top layer near the free surface. It is assumed that the vertical velocity profile goes to zero when it reaches the bottom, so not much is going on as we proceed towards the bottom of the domain. Therefore, the resolution in x-direction is set to 50 cells per wavelength and for the z-direction only 10 cells are which have been unevenly spaced so that the resolution is fine at the free surface, but becomes coarser as we go down. This is done using the argument `map` in the function `CartesianDiscreteModel`. The function `simplexify` is used to change the mesh to an affine reference map, which is necessary to have the mapping work.

$$z_i = d - \frac{d}{2^i} \quad \text{for} \quad i < n_{\text{cells},z}$$
$$z_i = d \quad \text{for} \quad i = n_{\text{cells},z}$$

```
meshX = 50
meshZ = 10
function f_z(x)
    if x == d
        return d
    end
```

```
    i = x / (d/meshZ)
    return d-d/(2^i)
end
map(x) = VectorValue(x[1],f_z(x[2]))
Xspan = Int(round((Xmax - Xmin) / λ))
Zspan = Int(round((Zmax - Zmin) / λ))
partition = (Xspan * meshX, Zspan * meshZ)
model_Ω = simplexify(CartesianDiscreteModel(domain,partition, map=map))
Ω = Triangulation(model_Ω)
```

Boundaries

As the numerical domain `model_Ω` has been initiated, we wil now define the location of the floating structure using the following function and using a `mask`:

```
function is_beam(coords)
    n = length(coords)
    x = (1/n)*sum(coords)
    (xb₀ <= x[1] <= xb₁ ) * ( x[2] ≈ d )
end

labels = get_face_labeling(model_Ω)

bgface_to_mask = get_face_mask(labels,[3,4,6],1)
Γface_to_bgface = findall(bgface_to_mask)
model_Γ = BoundaryDiscreteModel(Polytope{1},model_Ω,Γface_to_bgface)
Γ = Triangulation(model_Γ)

Γface_coords = get_cell_coordinates(Γ)
Γface_mask = lazy_map(is_beam,Γface_coords)
Γbface_Γface = findall(Γface_mask)
Γfface_Γface = findall(!,Γface_mask)

Γb = BoundaryTriangulation(model_Ω,view(Γface_to_bgface,Γbface_Γface))
Γf = BoundaryTriangulation(model_Ω,view(Γface_to_bgface,Γfface_Γface))
```

As well as the other boundaries:

```
add_tag_from_tags!(labels,"bottom",[1,2,5])
add_tag_from_tags!(labels,"inlet",[7])
add_tag_from_tags!(labels,"outlet",[8])
add_tag_from_tags!(labels, "water", [9])
```

The inlet of the domain is specified and a vertical velocity profile is imposed which is based on the gradient of the potential function:

$$\frac{\delta\phi}{\delta x} = \omega\xi\frac{\cosh k(z+d)}{\sinh kd}\cos(kx-\omega t-\theta)$$

```
Γin = BoundaryTriangulation(model_Ω, tags = ["inlet"])

θ = π/2 # phase shift
function v_inlet(x,t)
    return (ω * ξ * ( cosh( k * (x[2]) ) / sinh( k * d ) ) * cos(k * x[1] - ω * t - θ))
end

v_inlet(t::Real) = x -> v_inlet(x,t)
```

Finally, the quadratures are specified for each boundary:

```
order = 2
dΩ = Measure(Ω,2*order)
dΓb = Measure(Γb,2*order)
dΓf = Measure(Γf,2*order)
dΓin = Measure(Γin,2*order)

Λb = SkeletonTriangulation(model_Γ,Γface_mask)
nΛb = get_normal_vector(Λb)
dΛb = Measure(Λb,2*order)
mean_mask = CellField(mean(CellField(Γface_mask,Γ)),Λb)
```

Finite Element spaces

As the numerical domain has been set and the boundaries have been defined, the test spaces can be constructed. For this type of problem, two spaces will be built; one for the internal domain `model_Ω` and one for the free surface `model_Γ`. Both will use lagrangian shape functions and are of order two. For the free surface there will be imposed dirichlet boundary conditions on all boundaries except for the free surface.

```
reffe = ReferenceFE(lagrangian,Float64,order)
V_Ω = TestFESpace(
    model_Ω,
    reffe,
    conformity=:H1
    )
V_Γ = TestFESpace(
    model_Γ,
    reffe,
    conformity=:H1,
    dirichlet_tags=["bottom", "water", "inlet", "outlet"]
    )
```

A `TrialFESpace` is established using the test spaces and dirichlet boundary conditions. Note that for the `"bottom"`, `"water"` and `"outlet"` boundary the value is set to zero using the function `u`. For the `"inlet"` boundary, the dirichlet condition is set to a vertical velocity profile which has been specified with the function `v_inlet`.

```
u(x,t) = 0
u(t::Real) = x -> u(x,t)
U_Ω = TransientTrialFESpace(V_Ω)
U_Γ = TransientTrialFESpace(V_Γ, [u,u,v_inlet,u])
```

The test spaces and trial spaces are combined in a `MultiFieldFESpace` indicated by `X` and `Y`, respectively.

```
X = TransientMultiFieldFESpace([U_Ω,U_Γ])
Y = MultiFieldFESpace([V_Ω,V_Γ])
```

Numerical time integration

To solve the system in time, a numerical time integration scheme needs to be chosen. As the set of equations consists of a second temporal derivative, the Newmark-beta integration scheme has been chosen, which is widely used in the dynamic response of structures. Generally, the system is explicit, however, by choosing the parameters $\beta = 0.25$ and $\gamma = 0.5$, the system becomes unconditionally stable, which means that the time step can be chosen independently of the grid resolution. In this case, it was found that the results were accurate if the time step was equal to grid resolution in x-direction, resulting in a time step of 1/50 of the wave period.

$$\mathbf{M}\ddot{y} + \mathbf{C}\dot{y} + f^{int}(y) = f^{ext}$$

$$\begin{aligned}
\dot{y}_{n+1} &= \dot{y}_n + (1-\gamma)\Delta t\ddot{y}_n + \gamma\Delta t\ddot{y}_{n+1} \\
y_{n+1} &= y_n + \Delta t\dot{y}_n + \tfrac{\Delta t^2}{2}((1-2\beta)\ddot{y}_n + 2\beta\ddot{y}_{n+1}) \\
\mathbf{M}\ddot{y}_{n+1} &+ \mathbf{C}\dot{y}_{n+1} + f^{\text{int}}\ (y_{n+1}) = f^{\text{ext}}_{n+1}
\end{aligned}$$

```
γ = 0.5   # Newmark beta factor
β = 0.25  # Newmark beta factor
Δt = T / meshX # time step
```

Stabilisation terms

To make sure that the system of equations is coercive, the weak formulation is stabilised by stabilisation terms. Currently, Oriol Colomés Gené is doing research to find the correct set of stabilisation terms to solve this problem. For now, a default value of $\alpha h = 0.5$ is used to display the correct values.

```
∂ut_∂u = γ/(β*Δt)
∂utt_∂u = 1/(β*Δt^2)
αh = 0.5                                                    # default value
h_m = min((Xmax-Xmin)/partition[1],(Zmax-Zmin)/partition[2])
β_f = ∂ut_∂u / (αh*g + ∂ut_∂u)                              # stability parameter
fluid
β_b = ∂ut_∂u / (αh*(ρ_b/ρ_w*h*∂utt_∂u + g) + ∂ut_∂u)        # stability parameter
structure
γ_m = 1.0e2*order*(order+1)
```

`s((ϕ,η),(w,v))` is a function containing all stabilisation terms that will be included in the weak formulation to ensure a stable system.

```
s((ϕ,η),(w,v)) = ∫( (mean_mask==1)*β_b*EI/ρ_w*( - ( jump(∇(v)⋅nΛb) * mean(Δ(η)) +
jump(αh*∇(w)⋅nΛb) * mean(Δ(η)) ) - ( mean(Δ(v)) * jump(∇(η)⋅nΛb) ) + γ_m/h_m * (
jump(∇(v)⋅nΛb) * jump(∇(η)⋅nΛb) + αh*jump(∇(w)⋅nΛb) * jump(∇(ϕ)⋅nΛb) ) ) )dΛb
```

Weak formulation

The weak form is the set of equations that will be solved by `Gridap`. The Newmark-beta scheme distinguishes between three different matrices; the mass matrix M which contains the seond derivative terms, the damping matrix C which contains the first derivative terms, f_{int} and the other terms of the standard form. Finally there is the vector that includes the external loads f_{ext}. In `Gridap`, four functions are used that resemble the mentioned matrices. `m((ϕtt,ηtt),(w,v))`, `c((ϕt,ηt),(w,v))` and `a((ϕ,η),(w,v))` form the bi-linear form and `b(t,(w,v))` is the vector containing the externeal forces.

```
m((ϕtt,ηtt),(w,v)) = ∫( ρ_b/ρ_w*h*ηtt*β_b*(v+αh*w) )dΓb

c((ϕt,ηt),(w,v)) =  ∫( β_f*(αh*w + v)*ϕt - w*ηt )dΓf +
                    ∫( β_b*(αh*w + v)*ϕt - w*ηt )dΓb

a((ϕ,η),(w,v)) =  ∫( ∇(ϕ)⋅∇(w) )dΩ +
                  ∫( β_f*(v + αh*w) * g*η - μ₁*η*w - μ₂*ϕ*w/g )dΓf +
                  ∫( β_b*(Δ(v) + αh*Δ(w)) * EI/ρ_w*Δ(η) + β_b*(v + αh*w) * g*η + EI/
ρ_w*αh*Δ(w)*Δ(ϕ) )dΓb +
                   s((ϕ,η),(w,v))

b(t,(w,v)) =  ∫( v_inlet(t) * w )dΓin +
              ∫( β_b*(αh*w + v)*(-0.0) )dΓb
```

The set of equations is combined into one matrix and the numerical solver is set up.

Solver

```
op = TransientConstantMatrixFEOperator(m,c,a,b,X,Y)
ls = LUSolver()
odes = Newmark(ls,Δt,γ,β)
solver = TransientFESolver(odes)
```

The initial solution is set to zero.

```
x₀ = interpolate_everywhere([0.0, 0.0],X(0.0))
v₀ = interpolate_everywhere([0.0, 0.0],X(0.0))
a₀ = interpolate_everywhere([0.0, 0.0],X(0.0))
```

And all time steps are set, ready to be computed.

```
t₀ = 0.0
periods = 50
tf = periods * T
sol_t = Gridap.solve(solver,op,(x₀,v₀,a₀),t₀,tf)
```

The `WriteVTK` and `FileIO` modules are loaded to store the results on the computer and a directory is created to store all the files.

```
using WriteVTK
using FileIO


folderName = "solution"
if !isdir(folderName)
    mkdir(folderName)
end
```

The model consists of three parts; the 2D potential domain and the free surface which can be subdivided into the fluid part and structure part. Each is stored seperately and can be viewed in Paraview.

```
filePath_Ω = folderName * "/fields_O"
filePath_Γb = folderName * "/fields_Gb"
filePath_Γf = folderName * "/fields_Gf"
pvd_Ω = paraview_collection(filePath_Ω, append=false)
pvd_Γb = paraview_collection(filePath_Γb, append=false)
pvd_Γf = paraview_collection(filePath_Γf, append=false)
```

Finally, a for loop is created that runs through all the timesteps and stores the potential `ϕn` and the surface elevation `ηn` of each time step.

```
for ((ϕn,ηn),tn) in sol_t
  println(tn)

  pvd_Ω[tn] = createvtk(Ω,filePath_Ω * "_$tn.vtu",cellfields = ["phi" => ϕn],order=2)
  pvd_Γb[tn] = createvtk(Γb,filePath_Γb * "_$tn.vtu",cellfields = ["eta" =>
ηn],nsubcells=10)
  pvd_Γf[tn] = createvtk(Γf,filePath_Γf * "_$tn.vtu",cellfields = ["eta" =>
ηn],nsubcells=10)

end

vtk_save(pvd_Ω)
vtk_save(pvd_Γb)
vtk_save(pvd_Γf)
```

This is the end of the tutorial and I hope you now understand how to build a fluid structure interaction in `Gridap`. If you want to learn extra things, like storing values of a test run or calculating the energy in the system, please take a look below in the Extra's section.

Extra's

The following blocks of code help to further explore the results that have been generated with the numerical model. If you want to run this file please comment out the full Extra's section to have the code properly work.

Storing values

Sometimes, you don't want to only look at the results in Paraview, but also use them for more scientific uses. Then it is convenient to store all the values in a `Dict()`. By creating a dictionary, it is possible to save all variables in a wrapper. Here, the module `JLD2` is used which also gives the possibilty to save a `.jld2` file which contains all the data. Just follow the approach below:

```
using DelimitedFiles
using JLD2

dat = Dict()

dat[:λ] = λ
dat[:ξ] = ξ
dat[:st] = steepness
dat[:d] = d
dat[:k] = k
dat[:ω] = ω
dat[:T] = T

dataname = "data"
datapath = "solution"
save(datapath * "$dataname.jld2", "data", dat)
```

Saving free surface as vector

To save surface elevation as a datastring, a few extra lines need to be added to the for loop. A `global` variable `ηns` is created before the for loop. In the loop, for each time step, the surface elevation is stored in a local variable `surface` and subsequently `push!`'ed to `ηns`. The datastring can be stored in a JLD2 file as mentioned in the previous section.

```
global ηns = []
for ((ϕn,ηn),tn) in sol_t
  println(tn)

  global cell_values_ηn = get_cell_dof_values(ηn)
  surface = []
  for i in 1:length(cell_values_ηn)
      push!(surface, cell_values_ηn[i][3])
  end
  push!(ηns, surface')
  ηns = vcat(ηns...)

end
```

Calculating energy in the system

To check the amount of energy in the system, the sum of all values can be taken in the for loop as well. Here, we distinguish the energy between potential energy `Eₚ_f` and kinetic energy `Eₖ_f` for the free surface. For the structure, two more energy terms are taken into account; the kinetic energy `Eₖ_b` and the elastic energy `Eₚ_b` of the structure. In this example the energy is calculated at three different locations; the incident wave zone `xp1`, the hydroelastic wave zone `xp2` and the outgoing wave zone `xp3`.

```
global Eₖ_f_p1 = []
global Eₚ_f_p1 = []

global Eₖ_f_p2 = []
global Eₖ_b_p2 = []
global Eₚ_f_p2 = []
global Eₚ_b_p2 = []

global Eₖ_f_p3 = []
global Eₚ_f_p3 = []

global η_0 = interpolate_everywhere(0.0, U_Γ(0.0))

global xp1 = 1 * λ
global xp2 = 3 * λ
global xp3 = 9 * λ

x_p1(x) = (xp1 <= x[1] <= (xp1 + λ))
x_p2(x) = (xp2 <= x[1] <= (xp2 + λ))
x_p3(x) = (xp3 <= x[1] <= (xp3 + λ))

for ((ϕn,ηn),tn) in sol_t
  println(tn)

  push!(Eₖ_f_p1, 0.5 * ρ_w * ∑( ∫(∇(ϕn)⋅∇(ϕn) * x_p1 )dΩ ))
  push!(Eₚ_f_p1, 0.5 * ρ_w * g * ∑( ∫((ηn*ηn) * x_p1 )dΓf ))
```

```
  push!(Eₖ_f_p2, 0.5 * ρ_w * ∑( ∫(∇(ϕn)⋅∇(ϕn) * x_p2 )dΩ ))
  push!(Eₚ_b_p2, 0.5 * EI * ∑( ∫(Δ(ηn)⋅Δ(ηn) * x_p2 )dΓb ))
  push!(Eₖ_b_p2, 0.5 * ρ_b * h * ∑( ∫((ηₜ*ηₜ) * x_p2 )dΓb ))
  push!(Eₚ_f_p2, 0.5 * ρ_w * g * ∑( ∫((ηn*ηn) * x_p2 )dΓb ))

  push!(Eₖ_f_p3, 0.5 * ρ_w * ∑( ∫(∇(ϕn)⋅∇(ϕn) * x_p3 )dΩ ))
  push!(Eₚ_f_p3, 0.5 * ρ_w * g * ∑( ∫((ηn*ηn) * x_p3 )dΓf ))

  η_0 = interpolate_everywhere(ηn, U_Γ(tn))

end
```

This page was generated using Literate.jl.

Written by Sjoerd van Hoof © 2021

Bibliography

Mohit Acharya and Sarvesh Devraj. Floating Solar Photovoltaic (FSPV): A Third Pillar to Solar PV Sector ? *TERI Discussion Paper:Output of the ETC India Project (New Delhi: The Energy and Resources Institute)*, page 68, 2019. URL www.teriin.org.

I. Akkerman, J. H.A. Meijer, and Marco F.P. Ten Eikelder. Isogeometric analysis of linear free-surface potential flow. *Ocean Engineering*, 201(February):107114, 2020. ISSN 00298018. doi: 10.1016/j.oceaneng.2020.107114. URL https://doi.org/10.1016/j.oceaneng.2020.107114.

Santiago Badia and Francesc Verdugo. Gridap: An extensible Finite Element toolbox in Julia. *Journal of Open Source Software*, 5(52):2520, 2020. ISSN 2475-9066. doi: 10.21105/joss.02520.

Wilem Biesheuvel. Interview with Groenleven. Personal Communication, 2020. Online; accessed October 2020.

Oriol Colomés, Francesc Verdugo, Nabil Atallah, and Sjoerd van Hoof. A monolithic Finite Element formulation for the hydroelastic analysis of Very Large Floating Structures. (Draft), 2021.

Minne De Jong and Wim Soppe. Interview with TNO. Personal Communication, 2020. Online; accessed October 2020.

Jeroen De Werd and Clemens Van der Nat. Interview with Bluewater. Personal Communication, 2020. Online; accessed October 2020.

Deltares. Site Studies Wind Farm Zone Borssele - Metocean study for the Borssele Wind Farm Zone Site IV. page 127, 2015. URL https://english.rvo.nl/sites/default/files/2015/02/SiteStudiesWindFarmZoneBorssele{_}MorphodynamicsofBorsseleWindFarmZone.pdf.

J. Den Bieman and A. Kieftenburg. *Handreiking voor het afleiden van ontwerpwaterstanden en golfcondities: T.b.v het ontwerp van dammen, zee- en meerdijken*. 2015. ISBN 4500222634.

DNV-GL. DNVGL-ST-N001 Marine operations and marine warranty. (June), 2016.

P J Eecen. Measurements of Wind , Wave and Currents at the Offshore Wind Farm Egmond aan Zee. *Ecn.Nl*, (December), 2009.

IEA. Solar, 2020. URL https://www.iea.org/fuels-and-technologies/solar.

Changqing Jiang, Ould Moctar, Thomas E Schellin, and Yan Qi. Numerical Investigation of Hydroelastic Effects on Floating Structures. *PtW 2020*, 2020.

Min Woo Kim, Weoncheol Koo, and Sa Young Hong. Numerical analysis of various artificial damping schemes in a three-dimensional numerical wave tank. *Ocean Engineering*, 75:165–173, 2014. ISSN 00298018. doi: 10.1016/j.oceaneng.2013.10.012. URL http://dx.doi.org/10.1016/j.oceaneng.2013.10.012.

Pijush Kundu and Ira Cohen. *Fluid mechanics 2nd Edition*, volume 6. 1987. ISBN 0080339336. URL http://www.springerlink.com/index/10.1007/b138775.

Pierce Mayville, Neha Vijay Patil, and Joshua M. Pearce. Distributed manufacturing of after market flexible floating photovoltaic modules. *Sustainable Energy Technologies and Assessments*, 42 (February):100830, 2020. ISSN 22131388. doi: 10.1016/j.seta.2020.100830. URL https://doi.org/10.1016/j.seta.2020.100830.

Nathan M. Newmark. A Method of Computation for Structural Dynamics. *Journal of the Engineering Mechanics Division*, 85(3):67–94, jul 1959. ISSN 0044-7951. doi: 10.1061/JMCEA3.0000098. URL http://ascelibrary.org/doi/10.1061/JMCEA3.0000098.

Shigeo Ohmatsu. Overview: Research on wave loading and responses of VLFS. *Marine Structures*, 18(2):149–168, 2005. ISSN 09518339. doi: 10.1016/j.marstruc.2005.07.004.

William Otto. Interview with Marin. Personal Communication, 2020. Online; accessed October 2020.

Sebastian Schreier and Gunnar Jacobi. Measuring Hydroelastic Deformation of Very Flexible Floating Structures. *WCFS2020 - Proceedings of the Second World Conference on Floating Solutions*, 2020a.

Sebastian Schreier and Gunnar Jacobi. Experimental investigation of wave interaction with a thin floating sheet. *Proceedings of the International Offshore and Polar Engineering Conference*, 2020-Octob:2479–2488, 2020b. ISSN 15551792.

H. Suzuki, H. R. Riggs, M. Fujikubo, T. A. Shugar, H. Seto, Y. Yasuzawa, B. Bhattacharya, D. A. Hudson, and H. Shin. Very Large Floating Structures. In *Volume 2: Structures, Safety and Reliability; Petroleum Technology Symposium*, pages 597–608. ASMEDC, jan 2007. ISBN 0-7918-4268-1. doi: 10.1115/OMAE2007-29758. URL https://asmedigitalcollection.asme.org/OMAE/proceedings/OMAE2007/42681/597/323259.

The SWASH team. USER MANUAL SWASH version 7.0.1. Technical report, Delft University of Technology, Delft, 2020. URL http://www.tudelft.nl/swash.

Lonny L. Thompson and Runnong Huan. Implementation of exact non-reflecting boundary conditions in the finite element method for the time-dependent wave equation. *Computer Methods in Applied Mechanics and Engineering*, 187(1-2):137–159, 2000. ISSN 00457825. doi: 10.1016/S0045-7825(99)00114-0.

Takashi Tsubogo. On the dispersion relation of hydroelastic waves in a plate. *Journal of Marine Science and Technology*, 4(2):76–83, 1999. ISSN 09484280. doi: 10.1007/s007730050009.

Takashi Tsubogo and Hiroo Okada. Estimation method of dynamic behavior of huge mat-type floating structures using simple beam modeling. *Proceedings of the International Conference on Offshore Mechanics and Arctic Engineering - OMAE*, 1998.

Vincent Van Daalen. Interview with ProFloating. Personal Communication, 2020. Online; accessed October 2020.